FLOW OF A NON-NEWTONIAN BINGHAM PLASTIC FLUID OVER A ROTATING DISK

A Thesis

Submitted to the College of Graduate Studies and Research

In Partial Fulfillment of the Requirements

For the Degree of

Doctor of Philosophy

in the Department of Mechanical Engineering

University of Saskatchewan

Saskatoon, Saskatchewan

By

Ali A. Rashaida

PERMISSION TO USE

The author has agreed that the library, University of Saskatchewan, may make this thesis freely available for inspection. Moreover, the author has agreed that permission for extensive copying of this thesis for scholarly purposes may be granted by the professors who supervised the thesis work recorded herein or, in their absence, by the Head of the Department or Dean of the College in which the thesis work was done. It is understood that due recognition will be given to the author of this thesis, supervisors and to the University of Saskatchewan in any use of the material in this thesis. Copying or publication or any other use of this thesis for financial gain without the approval by the University of Saskatchewan and the author's written permission is prohibited.

Requests for permission to copy or to make any other use of material in this thesis in whole or in part should be addressed to:

Head of the Department of Mechanical Engineering,

57 Campus Drive,

University of Saskatchewan,

Saskatoon, Saskatchewan, Canada.

S7N 5A9

ABSTRACT

Even though fluid mechanics is well developed as a science, there are many physical phenomena that we do not yet fully understand. One of these is the deformation rates and fluid stresses generated in a boundary layer for a non-Newtonian fluid. One such non-Newtonian fluid would be a waxy crude oil flowing in a centrifugal pump. This type of flow can be numerically modeled by a rotating disk system, in combination with an appropriate constitutive equation, such as the relation for a Bingham fluid. A Bingham fluid does not begin to flow until the stress magnitude exceeds the yield stress. However, experimental measurements are also required to serve as a database against which the results of the numerical simulation can be interpreted and validated.

The purpose of the present research is to gain a better understanding of the behavior of a Bingham fluid in the laminar boundary layer on a rotating disk. For this project, two different techniques were employed: numerical simulation, and laboratory investigations using Particle Image Velocimetry (PIV) and flow visualization. Both methods were applied to the flow of a Bingham fluid over a rotating disk.

In the numerical investigations, the flow was characterized by the dimensionless yield stress "Bingham number", B_y, which is the ratio of the yield and viscous stresses. Using von Kármán's similarity transformation, and introducing the rheological behavior of the fluid into the conservation equations, the corresponding nonlinear two-point boundary value problem was formulated. A solution to the problem under investigation

was obtained by numerical integration of the set of Ordinary Differential Equations (ODEs) using a multiple shooting method. The influence of the Bingham number on the flow behavior was identified. It decreases the magnitude of the radial and axial velocity components, and increases the magnitude of the tangential velocity component, which has a pronounced effect on the moment coefficient, C_M, and the volume flow rate, Q.

In the laboratory investigations, since the waxy crude oils are naturally opaque, an ambitious experimental plan to create a transparent oil that was rheologically similar to the Amna waxy crude oil from Libya was developed. The simulant was used for flow visualization experiments, where a transparent fluid was required. To fulfill the demand of the PIV system for a higher degree of visibility, a second Bingham fluid was created and rheologically investigated. The PIV measurements were carried out for both filtered tap water and the Bingham fluid in the same rotating disk apparatus that was used for the flow visualization experiments. Both the axial and radial velocity components in the (r-z) plane were measured for various rotational speeds.

Comparison between the numerical and experimental results for the axial and radial velocity profiles for water was found to be satisfactory. Significant discrepancies were found between numerical results and measured values for the Bingham fluid, especially at low rotational speeds, mostly relating to the formation of a yield surface within the tank.

Even though the flow in a pump is in some ways different from that of a disk rotating in a tank, some insight about the behavior of the pump flow can be drawn. One conclusion is that the key difference between the flow of a Bingham fluid in rotating equipment from that of a Newtonian fluid such as water relates to the yield surface introduced by the yield stress of the material, which causes an adverse effect on the performance and efficiency of such equipment.

ACKNOWLEDGEMENT

I would like to express my profound appreciation and sincere gratitude to my supervisors, Professor Donald J. Bergstrom and Professor Robert J. Sumner for their invaluable guidance and supervision throughout the course of this work. Their encouragement and positive criticism have been mainly responsible for the success of this project.

I would also like to extend my sincere appreciation to my advisory committee members: Professor James D. Bugg for making his PIV system available to me, Professor Richard W. Evitts for his kind generosity in allowing me to use his electrochemical analytical rotator and Professor Spiro Yannacopoulos for his valuable academic advice. Also, I would like to extend my appreciation to my external examiner, Professor Anthony Yeung for his useful comments and suggestions.

I also wish to thank Mr. David M. Deutscher of the Thermo/Fluids Lab, Mr. Doug V. Bitner of the Fluid Power/Control Engineering Lab, Mr. Dave G. Crone of the Metallurgical Lab, and Mr. D. Claude of the Chemical Engineering Lab, for their assistance in laboratory matters. Also, the technical assistance from my graduate student colleagues, Mr. Abdul Shinneeb, Mr. Warren Brooke, Mr. Franklin Krampa-Morlu and Mr. Olajide Ganiyu Akinlade are gratefully acknowledged. My appreciation also goes to the secretaries in the Department of the Mechanical Engineering for their varied help and support.

I take this opportunity to express my deep gratitude to my parents for their moral and personal support, and for their encouragement in every step of my life.

Financial assistance provided by the Libyan Educational Program in the form of a Graduate Scholarship is thankfully acknowledged.

Special thanks to the many friends I have made during my stay in Canada for bringing me so many joyful moments.

DEDICATION

The sacrifices, encouragement, and support which I received from my family cannot be compensated by dedication of this piece of work to them. However, I would like to dedicate this thesis to my wife, Rakia, children, Abdalrahim, Raaid and Noor, my father Abdalrahim, my mother Kadija and my brothers and sisters. Thank you very much for your love and support throughout my Ph.D. studies.

كل الصبر و التضحية والتشجيع الذي تلقيته من عائلتي لايمكن أن يعوض بمجرد اهدائي لهم هذا العمل المتواضع. ومع هذا اهدي رسالة الدكتوراه الي زوجتي العزيزة راقية التي لولا اللـّه ثم صبرها ومثابرتها معي لما كان لهذه الرسالة أن ترى النور. كما اهديها لأبنائي الأعزاء عبدالرحيم ورائد ونور , ولأبي وأمي وإخوتي وأخواتي الغاليين. وفي النهاية اهدي هذه الرسالة لكل من ساهم بتعليمي أي شئ مفيد أو أضاف لهذا العالم بريق نور من المعرفة.

TABLE OF CONTENTS

LIST OF TABLES

LIST OF FIGURES

NOMENCLATURE

B_y	Bingham number defined by Eq. (3.29)
B_n	Global Bingham number
C_M	Torque coefficient
d_p	Diameter of the particle, μm
D	Disk diameter, m
h_c	Cavern height, m
d_c	Cavern diameter, m
e_{ij}	Rate-of-deformation tensor,
F, G, H	Dimensionless velocities in r, ϕ and z direction
K	Apparent viscosity of power-law fluids defined by Eq. (A.2)
m	Consistency index, Pa.s^n
M	Torque, N.m
n	Flow behavior index
N	Rotational speed, rad/sec
P	Pressure, Pa
q	Continuation parameter
Q	Flow rate, m^3/s
$\overline{Q}$	Delivery coefficient
r	Radial distance, m
R	Radius, m

Re_ϕ	Rotational Reynolds number defined by Eq. (4.9)
v_r, v_ϕ, v_z	Radial, tangential and axial velocity components, m/s
V_p	Particle radial velocity, μm/sec
z	Axial coordinate
δ	Thickness of momentum boundary layer, m
ϕ	Tangential coordinate
Ω	Angular velocity, s^{-1}
κ	Kinematic viscosity, m^2/sec
μ_p	Dynamic plastic viscosity, Pa.s
η	Apparent viscosity defined by Eq. (3.21), Pa.s
τ	Shear stress, Pa
τ_y	Yield stress, Pa
$\tau_{z\phi}$	Tangential shear stress defined by Eq. (3.26), Pa
τ_{zr}	Radial shear stress defined by Eq. (3.27), Pa
$\dot{\gamma}$	Shear rate, s^{-1}
ρ	Density of the fluid, kg/m^3
ρ_p	Particle density, kg/m^3
ζ	Dimensionless axial coordinate defined by Eq. (3.11)

Subscripts

r	Radial
z	Normal

ϕ	Angular
0	At surface
∞	Far field

CHAPTER 1

Introduction

This thesis presents the results of a numerical and experimental investigation of the hydrodynamics of a Bingham fluid flowing over a rotating disk. The motivation for the present study is introduced in this chapter. The characteristics of non-Newtonian fluid behavior, with specific reference to the yield stress, are also introduced. Waxy crude oil is one example of such a fluid. General remarks about the characteristics of rotating disk systems are also presented. The introduction will conclude with the objectives and the scope of this study.

1.1 Motivation

Most fluid flows encountered in environmental and industrial applications are directly influenced by a solid boundary. Significant shear rates and shear stresses often develop in narrow boundary layers associated with solid bodies moving through a liquid, such as the impeller of a centrifugal pump or the vanes of a turbine.

In the petroleum industry, centrifugal pumps are used extensively to transport fluids of high apparent viscosity such as waxy crude oils. Where the fluid has strong non-

Newtonian characteristics, pump performance is often observed to be adversely affected. For example, the pump head at a given flow rate may be significantly reduced (Walker and Goulas, 1984; Li, 2000). These effects not only relate to the rheology of the fluid, but also reflect the special deformation rates created in a pump.

A rotating disk system can be used to model the flow characteristics, including deformation rates, that occur in practical turbo-machinery such as the flow of waxy crude oils or foodstuffs in centrifugal pumps. There are various reasons for choosing the rotating disk system as a prototype for practical rotating flows. The rotating disk has proven to be a successful system for the study of transport phenomena in Newtonian fluids where a boundary layer type of flow occurs. It is one of the few three-dimensional flows which allow a complete analytical solution to the equations of motion. Experimentally, the rotating disk has many advantages over other geometries. For a liquid system, the apparatus consists of a housing to surround the disk and a motor-control system to provide rotation. Surprisingly, the flow of a non-Newtonian fluid over a rotating disk has received little attention, even though it has extensive technical application, such as turbo-machinery, lubrication and chemical processes. One common application involves the use of a centrifugal pump to transport non-Newtonian waxy crude oils. However, non-Newtonian shear characteristics can cause the flow through the impeller to differ in an adverse manner from that of the original pump design. Also, the speed of the rotating impeller subjects the fluid to relatively high shear. This high shear can cause degradation and damage to shear sensitive fluids, such as blood and foodstuffs. Therefore, the underlying motivation for the present work is to better understand this

flow behavior, which includes developing a better understanding of the shear distribution over a range of operating conditions.

1.2 Fluid Rheology

Rheology is the study of deformation and flow of fluids in response to stress. To make an incompressible fluid flow, a shear stress must be applied. Fluids include both gases and liquids. Here the focus on the liquids.

Consider a liquid placed between two parallel plates with area ***A*** as shown in Fig. 1.1. The top plate is moved with constant velocity, V, by the action of a shearing force F, while the bottom plate is fixed. Within this context, the following definitions apply:

Shear stress: The shear stress, τ, is defined as the force per unit area F/A.

Shear rate: If the variation in velocity between the plates is constant, the shear rate, $\dot{\gamma}$, is the velocity difference between the plates divided by the distance between them, h.

Viscosity: For a Newtonian fluid the viscosity is defined by Newton's law of viscosity,

$$\tau = \mu\dot{\gamma} \tag{1.1}$$

The fluid viscosity μ represents the resistance of the fluid to shearing force, and is called the dynamic viscosity. The kinematic viscosity is defined as

$$\kappa = \mu/\rho \tag{1.2}$$

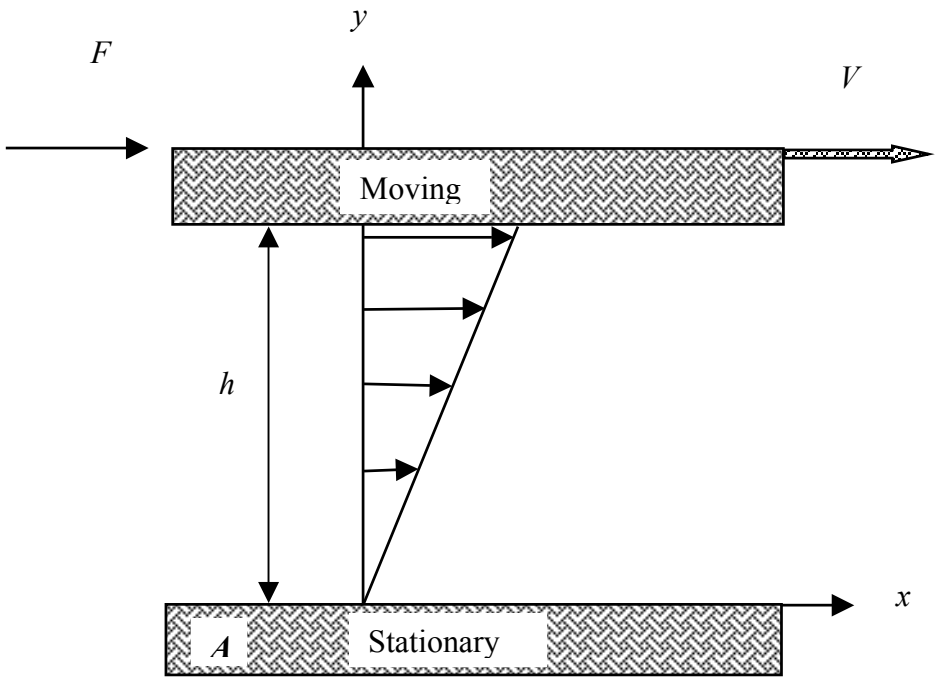

Figure 1.1: Shearing motion in a fluid between two parallel plates

1.2.1 Classification of Fluids

Fluids are normally classified into four categories, according to the relationship between the shear stress and shear rate:

1- Newtonian fluids

2- Time-independent non-Newtonian fluids

3- Time-dependent non-Newtonian fluids

4- Viscoelastic fluids

1.2.1.1 Newtonian Fluids

Newtonian fluids follow the simple rheological equation known as Newton's law of viscosity (Eq. 1.1). The magnitude of the viscosity is not dependent on shear rate or time. Its rheological behavior (shear stress versus shear rate) is shown in Fig. 1.2. It shows a linear relationship and passes through the origin. Water and mineral oils are common Newtonian liquids.

1.2.1.2 Time-Independent Non-Newtonian Fluids

Non-Newtonian fluids are only type of fluid which do not obey Newton's law of viscosity (Eq.1.1). The shear stress is a non-linear function of the shear rate. Fig. 1.2 shows the rheological behavior of several types fluids. The viscosity of a time-independent non-Newtonian fluid is dependent on the shear rate (Skelland, 1967). Depending on how the apparent viscosity changes with shear rate the flow behavior is characterized as follows:

Shear thinning

The apparent viscosity of the fluid decreases with increasing shear rate. This type of behavior is also referred to as "pseudoplastic" and no initial stress (yield stress) is required to initiate shearing. A number of non-Newtonian materials are in this category, including grease, molasses, paint, starch and many dilute polymer solutions.

Shear thickening

The apparent viscosity of this fluid increases with increasing shear rate and no initial stress is required to initiate shearing. This type of behavior is also referred to as "dilatant." Beach sand mixed with water and peanut butter are examples of dilatant

liquids. Dilatant liquids are not as common as pseudoplastic liquids. Dilatant rheological behavior is also shown in Fig. 1.2.

Viscoplastic Fluids

Viscoplastic materials are fluids that exhibit a yield stress. Below a certain critical shear stress there is no permanent deformation of the fluid and it behaves like a rigid solid. When that shear stress value is exceeded, the material flows like a fluid. Bingham plastics are a special class of viscoplastic fluids that exhibit a linear behavior of shear stress versus shear rate once the fluid begins to flow. An example of a plastic fluid is toothpaste, which will not flow out of the tube until a finite stress is applied by squeezing.

1.2.1.3 Time-Dependent Non-Newtonian Fluids

For these kinds of fluids, their present behavior is influenced by what happened to them in the recent past. These fluids seem to exhibit a "memory" which fades with time. The apparent viscosity of the fluid depends on a number of properties including shear rate and the history of the shearing process. Depending on how the apparent viscosity changes with time the flow behavior is characterized as:

Thixotropic

A thixotropic liquid will exhibit a decrease in apparent viscosity over time at a constant shear rate. Once the shear stress is removed, the apparent viscosity gradually increases and returns to its original value. When subjected to varying rates of shear, a thixotropic fluid will demonstrate a "hysteresis loop". Drilling mud and cement slurries are among the many materials which can exhibit thixotropic behavior.

Rheopectic

A rheopectic liquid exhibits a behavior opposite to that of a thixotropic liquid, i.e. the apparent viscosity of the liquid will increase over time at a constant shear rate. Once the shear stress is removed, the apparent viscosity gradually decreases and returns to its original value. Rheopectic fluids are rare. Examples include specific gypsum pastes and printers inks.

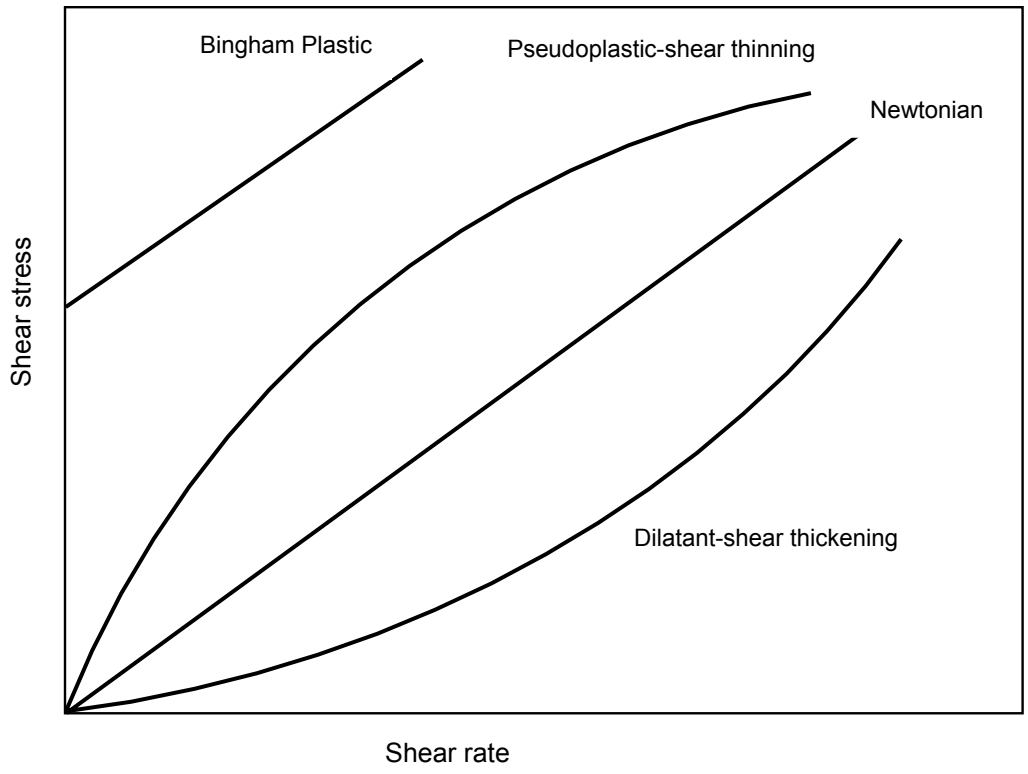

Figure 1.2: Rheological behavior of various types of non-Newtonian fluids

1.2.1.4 Viscoelastic fluids

These materials exhibit both viscous and elastic properties. The rheological properties of such a substance at any instant of time will be a function of the recent

history of the material and cannot be described by simple relationships between shear stress and shear rate alone, but will also depend on the time derivatives of both of these quantities. Typical examples of viscoelastic material are bread dough, polymer melts and egg white.

1.2.2 Viscoplastic Materials and the Yield Stress Concept

A viscoplastic material possesses a yield stress which must be exceeded before significant deformation can occur. In limiting cases, a viscoplastic material may flow and deform throughout the domain it occupies if the stress is everywhere above the yield stress in the control volume of interest; on the other hand, it may not flow at all if the stress is everywhere below this value. Such materials include suspensions and fine particle slurries including paint, pastes and foodstuffs.

A number of empirical relations have been proposed to account for the behavior of viscoplastic materials. The three most widely used are the Bingham, Casson, and Herschel-Buckley equations. The simplest and most widely used model is the two-parameter model proposed by Bingham (Bird et al., 1982):

$$\tau = \tau_y + \mu_p \dot{\gamma} \qquad |\tau| > \tau_y \tag{1.3}$$

$$\dot{\gamma} = 0 \qquad |\tau| \leq \tau_y \tag{1.4}$$

The Bingham model takes into account two parameters, the yield stress, τ_y, and the plastic viscosity, μ_p, to fully characterize the material rheology. Note that once the fluid flows, the plastic viscosity defines the rate of change of the excess shear stress τ- τ_y with the shear rate $\dot{\gamma}$. shear stress with shear rate. In contrast, the apparent viscosity is the ratio

of the shear stress to the shear rate, and in this case it approaches the plastic viscosity at very high shear rates. Figure 1.3 shows how two Bingham materials could have one identical parameter and a very different second parameter. These materials would consequently exhibit different flow behaviors.

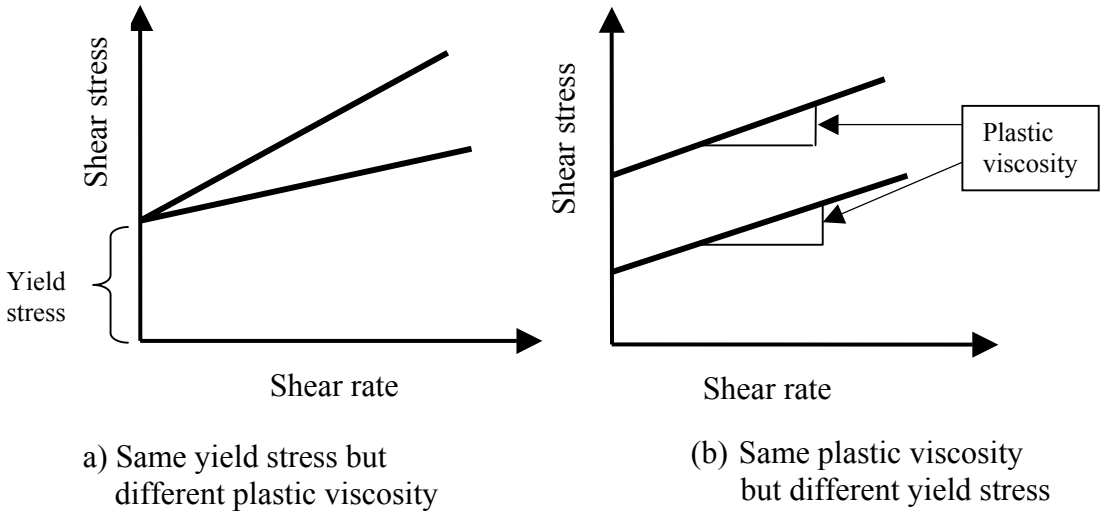

a) Same yield stress but different plastic viscosity

(b) Same plastic viscosity but different yield stress

Figure 1.3: Rheology of Bingham materials

1.2.3 Waxy Crude Oils

Crude oils, which are found in a number of reservoirs throughout the world, contain significant quantities of wax which can crystallize during production, transportation, and storage (Barry, 1971). This process can result in severe difficulties in pipelining and storage. The wax present in petroleum crudes consists of alkanes. Paraffin wax forms as a non-volatile long chain hydrocarbon with a composition of C_nH_{2n+2} where n is 30 or greater. It crystallizes to form an interlocking structure of plate, needle, or malformed crystals (Lovell and Seitzer 1981). When the oil is cooled to a temperature

lower than the crystallization point (generally called the pour point), the growing and agglomerating crystals entrap the oil into a gel-like structure. Consequently, the flow properties of the oil become distinctly non-Newtonian. At temperatures above the pour point, the waxy crude oils behave as Newtonian fluids.

1.3 Rotating Flows

Rotating flows are found in a number of technical applications including viscometry, lubrication, and rotating machinery such as centrifugal pumps. The internal geometry of centrifugal pumps is very complicated. In order to understand the flow and deformation that occurs in these pumps, it is common practice to approximate the geometries by plane rotating-disk systems. Fluid flows related to rotating disks can be classified into two main categories (Daily and Nece, 1960):

(a) "Free disk" is a disk that rotates within an infinite medium. The free disk is shown in Fig. 1.4 (a). It provides an asymptotic reference for all rotating-disk systems.

(b) "Enclosed disk" is a disk that rotates within a chamber of finite dimensions (rotor-stator system), as shown in Fig. 1.4 (b).

1.3.1 Free Disk

The case of laminar flow of an infinite flat disk rotating in a fluid represents one of the few exact solutions of the three-dimensional Navier-Stokes equations. This type of flow was first theoretically investigated using an approximate method developed by Von Kármán 1921 (Cochran, 1934). Using similarity transformations Von Kármán was able to

reduce the Navier-Stokes equations to a system of coupled ordinary differential equations. He found that this disk flow represents a boundary layer flow where the boundary layer thickness is independent of the radial distance. The tangential component of the shear stress at the disk surface imparts a circumferential velocity on the adjacent fluid layer, which in turn moves radially outwards due to the centrifugal forces. In other words, the fluid in the immediate neighborhood of the disk is circulated by friction, and then forced outwards by the centripetal acceleration. The velocity in the boundary layer has a radial and a tangential component. The fluid driven outwards by the centrifugal force is replaced by an axial flow toward the disk.

In the current study, the flow over a rotating disk has been restricted to the laminar flow regime. As discussed in Wu and Squires (2000), for a Newtonian fluid, the flow over a rotating disk is laminar for a Reynolds number, Re_ϕ, less than about 4.5 x 10^4. The flow is fully turbulent for Re_ϕ greater than about 3.9 x 10^5. For some Newtonian fluids, it is possible to increase the rotation rate and/or disk size to reach the turbulent regime. However, for a disk rotating in a Bingham fluid, simply increasing the rotation rate is not sufficient to generate turbulence, due to the large plastic viscosity that is associated with many Bingham fluids. However, once turbulence is generated, it enhances the performance of equipment handling Bingham fluids.

1.3.2 Enclosed Disk

Flows between a rotating and stationary disk in a fixed casing have been the subject of many investigations, since they model various practical configurations (Owen and Rogers, 1989). For a Newtonian fluid these flows are controlled by two parameters: the height to radius aspect ratio

$$A_R = h/R \tag{1.5}$$

where h is the axial distance between the two disks and R is the radius of the rotating disk, and the rotational Reynolds number

$$\mathrm{Re}_\phi = \Omega R^2/\kappa \tag{1.6}$$

where Ω is the angular velocity of the rotating disk and κ the kinematic viscosity of the working fluid.

(a) Free disk (b) Enclosed disk

Figure 1.4: Schematic diagram of rotating-disk systems

1.4 Instrumentation

Direct measurements of the velocity field in various flow configurations are important for verification of assumptions and predictions of various theoretical models. Only a limited number of experimental measurements of the velocity field in boundary layer flows induced by rotating bodies have been conducted (Wichterle et al., 1996). The lack of velocity data is partly due to the fact that conventional methods for measuring velocity, such as Pitot-tubes and thermal anemometry, are not suitable for such flows.

The development of optical methods such as laser Doppler velocimetry (LDV) and particle image velocimetry (PIV), together with recent advances in signal processing, represent great advances in the measurement of fluid velocity fields. PIV has proven to be a useful tool for experimental measurement of velocity profiles in rotating flows, since precise measurements may be performed without significant disturbance of the flow (Pedersen et al., 2003).

The PIV system measures velocity by determining particle displacement over time using a double-pulsed laser technique. A two frame cross-correlation method is employed in the present study. The synchronizer controls dual lasers through the computer which triggers and fires two laser pulse sequences at a given separation time and a given frequency during the measurement. The laser light sheets illuminate the plane of interest within the flowing fluid, which is seeded with tracer particles. The synchronizer also triggers the CCD camera and two image frames of particles in the

measurement region are obtained. Frame 1 contains the image from the first laser pulse, and frame 2 contains the image from the second laser pulse. The time between frame 1 and frame 2 is the same as that between laser pulse 1 and laser pulse 2. The flow velocity is found by measuring the distance the particle has traveled from frame 1 to frame 2, and dividing by the time between pulses.

1.5 Research Methodology

This research will use both numerical and experimental methods. The mass and momentum transport equations govern the flow of both Newtonian and non-Newtonian fluids. Boundary-layer approximations are often valid near a solid surface, and the resulting equations may be expressed in either differential or partially integrated form. Similarity hypotheses can facilitate the solution of transport equations, by recasting the problem in a more convenient form. With respect to material properties, Newtonian or non-Newtonian behavior can be represented using the appropriate model.

Experimental rotating flow investigations often employ both qualitative and quantitive measurements. Techniques of flow visualization and particle image velocimetry (PIV) can be used to map the velocity field in the region of high shear.

1.6 Objectives

The overall objective of the present thesis is to investigate the behavior of a Bingham fluid in the laminar boundary layer created on a rotating disk. The effect of the yield stress on the flow is of special interest. Two different techniques are adopted. The

first technique involved performing analytical modeling with numerical simulation. The second technique involved performing laboratory investigations using Particle Image Velocimetry (PIV) and a flow visualization technique. Both methods are applied to the flow of both Newtonian and Bingham plastic fluids over a rotating disk. The specific objectives of the thesis are as follows:

1. Numerically solve the problem of the flow of a Bingham fluid over a rotating disk; to explore the influence of the yield stress on the flow patterns; and to determine how different the resulting flow field is from that of a Newtonian fluid.
2. Create and measure the rheological properties of a transparent Bingham fluid that rheologically approximates the Amna waxy crude oil.
3. Qualitatively visualize the extent of the flow of the simulated waxy oil over the rotating disk using a dye visualization technique.
4. Measure the local velocity field of a Newtonian and a Bingham fluid flowingover a rotating disk using the PIV technique. The PIV measurements are not intended to be exhaustive but rather represent a first attempt to apply the technique to a Bingham fluid. Only laminar flow will be considered.
5. Assess the adequacy of the approximations of the numerical model in the light of the experimental results, and integrate the numerical and experimental results to better understand the flow of a Bingham fluid over a rotating disk.

1.7 Thesis Organization

The layout of the remaining chapters of this thesis is as follows. First, in Chapter 2, a review of previous work related to the simulation of rotating disk systems, fluid characterization, and experimental measurement and visualization is presented. Following this, a numerical investigation is presented in the next two chapters. Chapter 3 is devoted to the description of the problem, governing equations, Bingham and power law models, and use of similarity transformations to reduce the partial differential equations to a solvable set of ordinary differential equations. It also introduces the numerical solution of the system of non-linear ordinary differential equations, using a multiple shooting method. The results obtained from the numerical investigation are discussed in Chapter 4. The effects of fluid properties (plastic viscosity and yield stress) on the velocity field, torque and flow rate are also discussed. Then, the laboratory investigation is described in the next three chapters. Chapter 5 describes the rheological experiments which includes development of transparent waxy oils, viscosity measurements and rheological characterization. Chapter 6 presents visualization of the flow of a Bingham fluid over the rotating disk, while Chapter 7 discusses the experimental particle image velocimetery (PIV) results. Comparison of numerical and experimental results is also given. Finally, Chapter 8 summarizes the main conclusions, states the contributions of the thesis, and gives recommendations for future research.

CHAPTER 2

Literature Review

2.1 Flow Properties of Waxy Crude Oils

Waxy crude is one of the most common crude oils in the petroleum industry. Waxy crudes are very important from an environmental viewpoint since they have a low sulfur content (Barry, 1970). Also, their availability combined with the need for new sources of petroleum has encouraged production of these crude oils. However, wax agglomerates increase the apparent viscosity of this oil which increases the energy requirements associated with pipeline transportation. Since the temperature at which paraffin crystallizes is not particularly low (usually between 10° C and 30° C), the problem of crystallization affects most of the waxy crude oils that are found in nature (Lorenzo, 2003).

The successful and efficient production of waxy crudes requires knowledge and understanding of their rheological behavior. The rheological properties of different kinds of waxy crude oils have recently been studied. These studies report the existence of non-Newtonian behavior for certain waxy crudes. Barry (1971) had investigated waxy crude

oils from North Africa and noticed that at surface temperatures, the wax from the pumped crude oil begins to precipitate. This changes the transport characteristics from those of a Newtonian fluid to a non-Newtonian fluid. His work shows that these crudes behave as Newtonian fluids at 10° C above the pour point temperature. When the waxy crude oils are cooled below this temperature, they become non-Newtonian Bingham fluids. Davenport and Somper (1971) have reported that waxy crude oils from Libya and Nigeria have exhibited similar behavior. They develop a gel structure when cooled quiescently resulting in the observed Bingham behavior. Waxy crude oils from Venezuela were investigated by Rojas et al. (1977). These crude oils exhibited a yield stress which was associated with the crystallization of waxes at temperatures below the pour point. Irania and Zajac (1982) studied the West African waxy crude oils in Zaire and Cabinda. Their study also showed that the crudes behaved as a Bingham plastic, and yield stress values were determined by extrapolation of the linear section of shear stress-shear rate data.

Numerous studies (Wardhaugh and Boger, 1987; Wardhaugh and Boger, 1991; Ronningsen, 1992; Cheng, 1998) have also shown that below their pour point, waxy crude oils often exhibit time-dependent flow behavior which was believed to correspond to the gel structure gradually breaking down under the action of a constant shear stress or shear rate (termed “thixotropy”) (Davenport and Somper, 1971). This complicates measurement of the viscosity of waxy crude oil. Davenport and Somper (1971) noted that repeatable results could not be obtained even with the same apparatus. However, Wardhaugh and Boger (1987) showed that repeatable results could be achieved by the removal of the fluid memory and control of the shear and thermal history. This was

achieved by heating the sample to a sufficiently high temperature such that the wax crystals fully dissolve, loading the sample into a preheated viscometer and then cooling both the sample and instrument to the test temperature with careful control of the shear rate. Following this procedure, they concluded that the pretreated waxy (equilibrium state) oils behave as Bingham plastic fluids.

Oil producers have been aware of the difficulties of pipelining waxy crude oil and fuel oils for several decades. Traditionally the issue has been avoided by heating the crude or the crude and the pipeline, thus holding the wax in solution (El-Eman et al., 1993). It is possible to improve the flow of waxy crude oils by a number of alternative methods. Pipelining the crude as an oil in water (O/W) emulsion reduces the viscosity to nearly that of the continuous water phase (Marsden, 1973). Blending with a less waxy crude oil also improves the flow properties by altering the wax solubility relationships (Marsden, 1973). More recently, chemical additives, for example pour point depressants, flow improvers, paraffin inhibitors, or wax crystal modifiers have been developed. Small quantities of the additives are capable of affecting the crystal growth and as a result improve the flow properties (El-Eman et al., 1993 and Al-Fariss et al., 1993).

The mechanisms by which these additives modify the wax structures, however, are not completely understood. As such, the choice of the most appropriate additives for crude oils are largely based on trial and error rather than scientific principles. Therefore, conducting a waxy oil rheological investigation is of importance in the design of pipelines and pumps. In earlier studies, the characteristics of these oils were found to be

affected by temperature, shear rate and wax concentration (Wardhaugh and Boger, 1987; Wardhaugh and Boger, 1991; Ronningsen, 1992; Al-Fariss, 1993; Cheng and Boger, 1998).

2.2 The Concept of Yield Stress and Its Measurement

The yield stress concept was first introduced by Bingham and Green (1919) for a class of fluids known as viscoplastic fluids. After their initial work, many different equations have been proposed to describe the relationship between shear stress and shear rate for different viscoplastic materials (Nguyen and Boger, 1992). In many models, the yield stress was simply defined as the minimum stress required to produce a shear flow. As pointed out by Cheng (1998), for yield stress fluids in general, the yield stress is a time-dependent property. Upon yielding, the flow properties show time dependency indicating a degradation of structure with continued shear, finally developing equilibrium or time-independent flow properties (under certain circumstances) which still exhibit a yield stress which can be represented using the Bingham model. Early measurements of the yield point for waxy crude oils were performed with capillaries or pipelines (Davenport and Somper, 1971; Ronningsen, 1992). Both capillary and model pipeline techniques have now been rejected due to the uncertainties arising from the known effects of stress concentration, compressibility of the pipe and the oil, and diffusion of the wax-free oil (Davenport and Somper, 1971; Wardhaugh and Boger, 1991). Rotational viscometers with concentric cylinders, parallel plates, a cone–and plate, or vanes have also been used to study the yield stress of waxy crude oils (Davenport and Somper, 1971; Lovell and Seitzer, 1979; Wardhaugh and Boger, 1987; Al-Fariss et al., 1993; El-Eman et

al., 1993; Cheng and Boger, 1998; Kirsanov and Remizov, 1999). However, no standard test for determining the yield stress of waxy crude oils has been adopted by the petroleum industry because of the very poor repeatability between the different tests. One of the reasons for the poor repeatability is that the yield stress, along with other rheological properties of waxy crude oils, depend not only on what the sample is experiencing, i.e., temperature and shear rate, but also on what the sample has experienced, i.e., thermal and shear history (Wardhaugh and Boger, 1987; Ronningsen, 1992; Cheng and Boger, 1998). Wardhaugh and Boger, (1987, 1991) stated that even small variations in any of the test conditions or history can cause a marked difference in the measurement results.

2.3 Flow in Turbo-Machinery

In a turbo-machine, there is a conversion of the kinetic energy of a rotating shaft to the flow work of a moving stream. For pumps, fans and compressors, this conversion is from shaft work to flow work. For turbines, the conversion is from flow work to rotating shaft work. In all cases, the most important shear rates and shear stresses appear in narrow boundary layers of the moving solid parts, e.g. disks, impellers, and blades.

A common type of momentum-based pump is a centrifugal pump. A centrifugal pump consists of an impeller with blades rotating inside a casing. The impeller rotation reduces the pressure at the pump inlet causing fluid to flow into the pump. The fluid is then accelerated outward along the blades and exits the pump casing.

Typically, the pump characteristics are established in the pump manufacturer's test facilities using water as the test fluid. The performance data for media with other viscosities are only rarely tested in special closed-loop test facilities. In most cases, the water data will be converted to the new working conditions by applying formulas given in standard references (Hydraulic Institute Standard, 1975).

To the author's knowledge, the flow pattern of a non-Newtonian fluid in the impeller of a centrifugal pump has not yet been measured. This is due to the difficulty of measuring velocity and shear stress in rotating boundary layers, using conventional methods (Wichterle and Mitschka, 1998). For example, performing particle image velocimetry (PIV) measurements within turbine impellers is difficult due to the optical obstruction to the illuminating sheet and to the camera caused by the blades (Wichterle et al., 1996). However, studies have investigated the effect of non-Newtonian fluids on the performance of centrifugal pumps in general (Walker and Goulas, 1984; Li, 2000, Xu, et al., 2002). Li (2000) noted that using a viscous fluid drops the performance of a centrifugal pump because the high viscosity results in a rapid increase in the disk friction losses over the impeller shroud and hub as well as in the flow channels of the pump.

Because of the speed of the impeller, the fluid passing through the pump is subjected to high shear. This high shear can cause degradation and damage to shear sensitive fluids, such as blood and foodstuffs. This concern was the primary motivation for researchers in the biomedical industry and other biotechnological or chemical processes, to investigate shear distribution in centrifugal pumps (Lutz, 1998; Yamane,

1999). Lutz (1998) presented electro-diffusional measurements of the wall shear rate at the impeller surface of a radial centrifugal pump. Using a different approach, Yammane (1999) conducted a flow visualization study of a centrifugal blood pump to determine the shear and velocity profiles in the back gap between the impeller and the casing. Blood has rheological properties similar to a waxy crude oil, and both of them are classified as Bingham fluids.

Due to the geometric complexity of turbine impellers and the velocity field in a centrifugal pump, there is little chance for obtaining theoretical predictions from solution of the full equations of motion (Xu et al., 2002; Wichterle et al., 1996). However, for simplified rotating geometries, e.g., around rotating disks, such a solution can be obtained.

2.4 Flow in Rotating Disk Systems

The rotating disk is a popular geometry for studying different flows, because of its simplicity and the fact that it represents a classical fluid dynamics problem. It is a subject of widespread practical interest in connection with steam turbines, gas turbines, pumps, and other rotating fluid machines (Owen and Rogers, 1989). This flow paradigm has also been used to investigate the momentum (Andersson et al., 2001) and heat and mass transfer characteristics of Newtonian and non-Newtonian fluids (Kawase and Ulbrecht, 1983; Hansford and Litt, 1968; Mishra and Singh, 1978).

2.4.1 Newtonian Rotating Disk Flow

The rotating disk problem was first solved by von Kármán (1921). He showed that the Navier-Stokes equations for steady flow of a Newtonian incompressible fluid due to a disk rotating far from other solid surfaces can be reduced to a set of ordinary differential equations. These equations can be solved by an approximate integral method. The problem was further investigated both theoretically and experimentally by Cochran (1934), Goldstein (1935) and Gregory, Stuart, and Walker (1955). The disk acts like a centrifugal pump where the fluid near the disk is thrown radially outwards. This, in turn, creates an axial flow towards the disk to satisfy continuity. The mathematical solution of the Navier-Stokes equations for the Newtonian laminar case by von Kármán (1921) is an exact solution of the complete equations. However, the solution obtained is of the boundary-layer type. For the laminar case the boundary layer has a constant thickness, as shown theoretically by von Kármán (1921) and demonstrated experimentally by Gregory, Stuart and Walker (1955).

Bodewadt (1940) studied the problem of the disk at rest and the fluid at infinity rotating with uniform angular velocity. Lance and Rogers (1961) numerically studied a similar problem with the disk rotating with a different angular velocity than that of the surrounding fluid. Stewartson (1953), following a suggestion made by Batchelor (1951), investigated the effect of uniform suction of fluid from the surface of the rotating disk. The effect of suction is essentially one of decreasing both the radial and tangential components of the velocity and increasing the axial flow towards the disk at infinity. The boundary layer thinned as a consequence. Wagner (1948) and Millsaps and Pohlhausen

(1952) found that the heat transfer from a disk with a uniform surface temperature was different from that of the isothermal surroundings. Later, Sparrow and Gregg (1959) obtained the rate of heat transfer from a rotating disk to a fluid based on an arbitrary Prandtl number. Sparrow and Gregg (1960), considering the same rotating disk. They extended their investigation to study the effects of mass injection or removal at the surface of the disk on heat transfer rates and on the flow field around the disk.

A number of fluid flow devices have an internal geometry where non-rotating surfaces are located in close axial and radial proximity to rotating surfaces. This gives considerable attention to the case of a plane circular disk rotating in a concentric cylindrical housing closed at either end by flat circular end plates. This case includes the conditions obtained in centrifugal machinery where problems of disk friction torque and power loss, and heat transfer are related to the circulation and secondary flows induced by the rotating element (Daily and Nece, 1960). These induced flows are dependent on the geometries of the rotating element and its enclosure. Enclosed disk flow has been investigated analytically and experimentally by Soo (1958), Conover (1968), Mellor, Chapple and Stokes (1968), and Daily and Nece (1960). Soo (1958) performed an analytical study on the Newtonian laminar incompressible flow between a rotating disk and casing. His treatment addresses the case of radial inflow, radial outflow, and no-through flow. Experimental measurements of disk friction in a finite housing have shown that the case of an enclosed disk is quite different from the case of a disk in an infinite medium, although many of the theoretical correlations follow the trends associated with an infinite system (Conover, 1968; Daily and Nece, 1960).

In all the above studies, the fluid was assumed to be isothermal and exhibit Newtonian behavior. However, it is known that this physical property may change significantly with temperature or shear rates. To predict the flow behavior more accurately it is necessary to take into account non-Newtonian fluid behavior. This is the subject of the following section.

2.4.2 Non-Newtonian Rotating Disk Flow

Although the solution for a Newtonian fluid in a rotating disk system was first given many years ago (von Kármán, 1921), the equivalent solutions for non-Newtonian fluids appeared more recently in the literature (Mitschka and Ulbricht, 1965). Several investigators have considered the flow of non-Newtonian liquids on a rotating disk from a theoretical prospective. Acrivos et al. (1960) investigated the flow of a non-Newtonian fluid (power-law fluid) on a rotating plate. Their industrial motivation was to determine whether the non-Newtonian character of the substance would produce uniform films if the materials were spun rapidly on a disk. Because of the non-linearity introduced by the viscosity function, a similarity transformation is no longer possible. However, by using boundary-layer approximations and the appropriate dimensionless variables, one arrives at a set of ordinary differential equations that can be solved numerically (Mitschka and Ulbricht, 1965; Balaram and Luthra, 1973; Wichterle and Mitschka, 1998; Andersson et al., 2001). Mitschka and Ulbricht (1965) were the first to obtain a numerical solution for the flow caused by a disk rotating in liquids with a shear dependent viscosity, in this case a power-law liquid in the range $0.2 \leq \mathbf{n} \leq 1.5$. Wichterle and Mitschka (1998) revisited

the same study, with a focus on the shear of liquid particles to fit with the application of micro-mixing technology.

The work of Mitschka and Ulbricht (1965) was reconsidered by Andersson et al. (2001) to test the reliability of their numerical technique when considering shear-thickening fluids beyond those considered by Mitschka and Ulbricht. Their results confirm the high quality of the calculations of Mitschka and Ulbrecht, and conclude that the effect of the rheological parameter is that the boundary layer thickness increases as the power-law index n is reduced throughout the entire parameter range from 2.0 to 0.2.

Studies involving heat and mass transfer (Hansford and Litt, 1968; Mishra and Singh, 1978; Greif and Paterson, 1973) have used parts of the solutions provided by Mitschka and Ulbrecht (1965) in order to determine coefficients for heat and mass transfer.

In recent years the process of spin coating has been widely used in the manufacture of semiconductor devices, optical devices and magnetic recording devices. Many of the coating materials are suspensions and the Bingham fluid equation may be chosen to describe the rheological properties of the materials (Bird et al., 1982). However very few numerical, theoretical or experimental works have considered the flow of yield-stress fluids, which is due to the difficulties bound up with the surface separating the solid and gel phases. Matsumoto et al. (1982) have used the momentum integral method to analyze the film thickness of a Bingham fluid on a rotating disk. Their work is

unique in that it made the first attempt to investigate the film thickness for a non-Newtonian fluid. In this context, Jenekhe and Schuldt, (1985) have theoretically analyzed the free surface film flow of Bingham plastic liquids on a rotating disk. Their analysis found that the film thickness is not always uniform as was predicted for a Newtonian fluid by Emslie et al. (1958) and Brian (1986). Wilson et al. (1989) claimed that this defect was attributed to the original Bingham model that was used to describe the rheological properties of the materials. Because of the inherent discontinuity in the original Bingham model, the presence of the velocity gradients in the denominator of the constitutive equation makes this model singular as the yield surface is approached. Burgess and Wilson (1996) proposed the bi-viscosity model which was first introduced by O'Donovan and Tanner (1984). This model suggests a constitutive equation that is valid throughout the material. Other variations of the Bingham model have been introduced, for example, the exponential model proposed by Papanastasiou (1987) and the modified Bingham model by Bercovier and Engelman (1980) who added a small regularization parameter to the denominator of the viscosity function, so that it remains non-zero even when the yield surface is approached.

2.4 Visualization of Fluid Flows

Observations of flow patterns using streamlines or pathlines often reveal valuable qualitative information about fluid motion. In order to be able to investigate fluid motion, one must apply certain techniques to make the flow motion visible. Such methods are called flow visualization techniques.

One of the most important discoveries in the history of fluid mechanics was based on experimental observations by Reynolds (1883) using a dye injection technique to view the transition of flow from a laminar to a turbulent regime. Since then, flow visualization techniques have been used extensively in the development of many areas of fluid mechanics. Flow visualization techniques can be used to reveal qualitative features of the flow, and in some cases they even provide quantitive measurements of flow parameters.

There are many factors which guide the selection of a particular flow visualization method. Fluid properties, flow geometry, and cost are some of the main factors one must consider. For aerodynamic flow visualization, smoke generation methods are the most popular. According to the shape of the object of study, smoke-tube equipment or a smoke-wire (Mueller and Batill, 1980) can be used to generate visible smoke in a wind tunnel. In viewing liquid flows, dye injection, surface-coating, and solid particle tracing techniques are the most popular.

Visualization methods based on dye injection techniques have been reviewed by Werle (1973). Werle indicated that the primary concern with this technique is that the injection must not significantly alter the flow under study. For example, the velocity of the injected dye should be the same as the surrounding fluid.

Surface-coating techniques are mainly used to observe the flow of fluid in contact with a solid surface (Pao, 1983). Pao used Nigrosine dye to coat a solid surface. When it

is in contact with liquid, this dye will slowly dissolve to give a color sheet downstream of the coated surface.

2.5 Particle Image Velocimetry

In the past, a variety of one-point measurement techniques have been applied to measure the velocities at some selected positions in rotating disk systems. Daily and Nece (1960) used a Pitot tube to measure the velocities at some selected positions in a water rotating disk flow rig. Kang et al. (1998) obtained experimental results using a hot-wire anemometer from a smooth disk rotating in air and suggested that the probe has a big influence on the flow field. Laser Doppler velocimetry (LDV) were also reported by Berman and Pasch, (1986), Sirivat et al. (1988) and Riahi and Hill, (1994). These methods have provided fundamental knowledge regarding the flow phenomena occurring in rotating disk system. However, a more detailed knowledge of the flow field of a rotating disk is needed to validate the results of a numerical model. For this purpose, the particle image velocimetry (PIV) technique is a powerful alternative to these methods.

To date, there appears to have been no other reported PIV measurements of an infinite flow of a fluid over a rotating disk. The only previous works that are of relevance to our investigation are those by Prasad and Adrian (1993) and Zhou and Garner (1996). Although, the main attention of Prasad and Adrian (1993) was to test the stereoscopic PIV system (twin-camera), a basic distribution of the nature of a flow induced by a rotating disk in glycerin was given. Zhou and Garner (1996) used a PIV technique to measure the flow field of water inside an enclosed cylindrical chamber containing a

rotating disk. Their measurements were compared with the results obtained from a CFD model, but very little information was given regarding the behavior of the flow. One of the objectives of the present work is to demonstrate the potential of using the PIV technique to measure the velocity field of a non-Newtonian Bingham plastic fluid over a rotating disk.

CHAPTER 3

Numerical Model

In this chapter, a classical problem considered by von Kármán is extended to the laminar flow of a Bingham fluid over a rotating disk. The solution for the case of a power-law fluid is also obtained as a validation of the numerical technique. The flow of a Newtonian fluid is a special case of the constitutive equations of both the solution of the Bingham and the power-law models. The numerical solution to the (highly) non-linear ODEs arising from the non-linear relationship between the shear stress and the shear rate is presented.

Contrary to experiments, in numerical simulations it is possible to isolate certain properties of the fluid by using specific, idealized assumptions, and then study the effects of these assumptions on the flow. In this context, the numerical model assumes that the fluid near the disk has been sufficiently sheared for it to deform and flow to be established. The shear stresses in the vicinity of the disk are assumed everywhere to exceed the yield stress so that any plug-flow region is avoided.

3.1 Formulation of the Problem

The laminar flow produced by a disk rotating in an infinite fluid, where the effects of flow confinement do not exist, is a classical fluid mechanics problem. For this system, it is usually convenient to use a stationary frame of reference. As shown in Fig.3.1 the disk rotates about the z-axis with a constant angular velocity Ω, and the origin, 0, is taken as the point where the axis of rotation intersects the rotating disk. A cylindrical coordinate system (r, ϕ, z) is adopted such that ϕ is orientated in the direction of rotation. Let v_r, v_ϕ and v_z represent the components of the velocity vector in cylindrical coordinates. Additional assumptions are as follows:

- The flow is fully described by the continuity and conservation of momentum equations.
- The fluid flow is isothermal, laminar and its density, ρ, is constant.
- The flow is steady and axi-symmetric, i. e. $\partial/\partial t = \partial/\partial \phi = 0$ for all dependent variables.

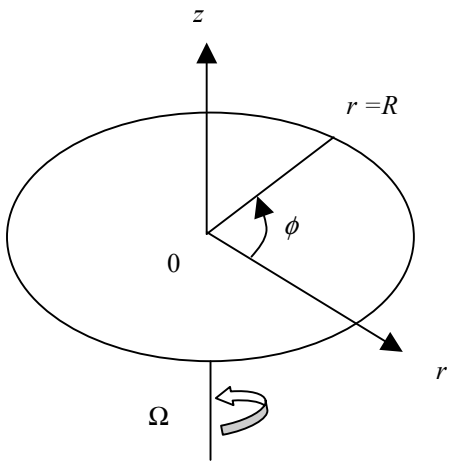

Figure 3.1: Coordinate system for rotating disk flow

3.1.1 Boundary Conditions

The boundary conditions for the velocity components at the surface and far away from the plate are given, respectively, by:

$$v_r = 0\ , \qquad v_\phi = \Omega r, \qquad v_z = 0 \qquad \text{at } z = 0, \tag{3.1}$$

$$v_r \to 0\ , \qquad v_\phi \to 0, \qquad \text{as } z \to \infty \tag{3.2}$$

The value of v_z vanishes near the surface of the disk, since there is no penetration. However, the value of v_z as $z \to \infty$ is not specified; it adjusts to a negative value, which provides sufficient fluid necessary to maintain the pumping effect. As shown below, it becomes part of the solution to the problem. In contrast to the axial velocity, both the radial and tangential velocities go to zero at large axial distances from the disk.

3.1.2 Equations of Motions

Applying the assumptions the transport equations for conservation of mass and momentum, in cylindrical co-ordinates, can be written as follows (Bird et al., 2002):

Continuity equation

$$\frac{\partial v_r}{\partial r} + \frac{v_r}{r} + \frac{\partial v_z}{\partial z} = 0 \tag{3.3}$$

Momentum equations

in the r-direction:

$$\rho\left(v_r \frac{\partial v_r}{\partial r} + v_z \frac{\partial v_r}{\partial z} - \frac{{v_\phi}^2}{r} \right) = -\frac{\partial p}{\partial r} + \frac{\partial \tau_{rr}}{\partial r} + \frac{\partial \tau_{rz}}{\partial z} + \frac{\tau_{rr} - \tau_{\phi\phi}}{r} \tag{3.4}$$

in the ϕ-direction:

$$\rho\left(v_r\frac{\partial v_\phi}{\partial r}+v_z\frac{\partial v_\phi}{\partial z}+\frac{v_r v_\phi}{r}\right)=\frac{1}{r^2}\frac{\partial}{\partial\phi}\left(r^2\tau_{r\phi}\right)+\frac{\partial\tau_{z\phi}}{\partial z}+\frac{\tau_{\phi r}-\tau_{r\phi}}{r} \tag{3.5}$$

in the z-direction:

$$\rho\left(v_r\frac{\partial v_z}{\partial r}+v_z\frac{\partial v_z}{\partial z}\right)=-\frac{\partial p}{\partial z}+\frac{1}{r}\frac{\partial}{\partial r}\left(r\tau_{rz}\right)+\frac{\partial\tau_{zz}}{\partial z} \tag{3.6}$$

3.1.3 Boundary Layer Approximations

Since the motion of the fluid is caused by the rotation of the disk, at sufficiently high Reynolds number the viscous effects will be confined within a thin layer near the disk. Therefore, further simplification can be obtained by considering the usual boundary-layer approximations (Owen and Rogers, 1989):

- The component of velocity v_z is very much smaller in magnitude than either of the other two components;
- The rate of change of any variable in the direction normal to the disk is much greater than its rate of change in the radial or tangential directions $\partial/\partial z >> \partial/\partial\phi$ and $\partial/\partial r$;
- The only significant fluid stress components are $\tau_{\phi z}$ and τ_{rz},.
- The pressure depends only on the axial distance from the axis of rotation.

Therefore, equation (3.3) is unchanged; it is repeated as equation (3.7). Equations (3.4) to (3.6) reduce to equations (3.8) to (3.10).

$$\frac{\partial v_r}{\partial r}+\frac{v_r}{r}+\frac{\partial v_z}{\partial z}=0 \tag{3.7}$$

$$v_r \frac{\partial v_r}{\partial r} + v_z \frac{\partial v_r}{\partial z} - \frac{{v_\phi}^2}{r} = \frac{1}{\rho} \frac{\partial \tau_{zr}}{\partial z} \tag{3.8}$$

$$v_r \frac{\partial v_\phi}{\partial r} + v_z \frac{\partial v_\phi}{\partial z} + \frac{v_r v_\phi}{r} = \frac{1}{\rho} \frac{\partial \tau_{z\phi}}{\partial z} \tag{3.9}$$

$$0 = \frac{\partial p}{\partial z} \tag{3.10}$$

3.2 Similarity Transformations

The classical approach for finding exact solutions of linear and non-linear partial differential equations is the similarity transformation. They are the transformations by which a system of partial differential equations with n-independent variables can be converted to a system with n-1 independent variables. The axisymmetric momentum equations associated with rotating disk flow have mainly been solved using a similarity transformation, which allows the governing partial differential equation set to be transformed into a set of ordinary differential equations. In the similarity solution, analytical relationships will be used and dimensionless parameters will be substituted so that the number of variables to be solved is reduced.

The solution is based on the appropriate non-dimensional transformation variable given by von Kármán (Cochran, 1934) i.e.,

$$\zeta = z\left(\frac{\Omega}{\kappa}\right)^{1/2} \tag{3.11}$$

along with the associated set of dimensionless velocity components and pressure, i.e.,

$$F(\zeta) = \frac{v_r}{\Omega r} \tag{3.12 a}$$

$$G(\zeta) = \frac{v_\phi}{\Omega r} \tag{3.12 b}$$

$$H(\zeta) = \frac{v_z}{(\Omega \kappa)^{1/2}} \tag{3.12 c}$$

$$P(\zeta) = -\frac{p}{\rho \ \Omega \ \kappa} \tag{3.12 d}$$

This similarity transformation implies that all three dimensionless velocity components depend only on the distance from the disk, ζ. The boundary conditions are transformed into the ζ coordinate as follows:

$$F(0) = 0 \ , \qquad G(0) = 1, \qquad H(0) = 0 \qquad \text{at} \ \ \zeta = 0, \tag{3.13}$$

$$F(\zeta) \to 0 \ , \qquad G(\zeta) \to 0, \qquad \text{as} \ \ \zeta \to \infty \tag{3.14}$$

Note that the formulation above becomes problematic at the axis of the disk, where among other things the boundary layer assumptions break down.

3.3 Constitutive Models

3.3.1 Bingham Model

Now consider the flow of a Bingham fluid over a rotating disk. A Bingham fluid does not deform until the stress level reaches the yield stress, after which the "excess stress" above the yield stress drives the deformation. This results in a two-layered flow consisting of a 'plug layer' and a 'shear layer'. Figure 3.2 shows a sketch of a Bingham fluid flowing over a rotating disk, using a cylindrical coordinate system (r, ϕ, z).

In a number of cases, the Bingham constitutive equation adequately represents the stress–deformation behavior of materials with a yield stress (Bird et al., 1982). This

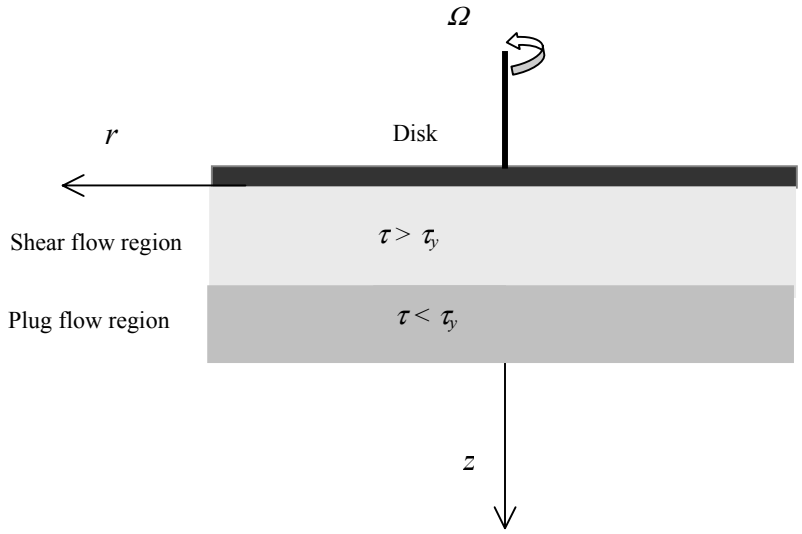

Figure 3.2: Simplified schematic of the flow geometry of a Bingham fluid on a rotating disk

model relates the rate-of-deformation tensor, e_{ij}, defined below in terms of the velocity field vector v_i

$$e_{ij} = \left(\frac{\partial v_i}{\partial x_j} + \frac{\partial v_j}{\partial x_i} \right), \tag{3.15}$$

to the deviatoric stress tensor, τ_{ij}, using the following relations:

$$e_{ij} = \begin{cases} \dfrac{\tau_{ij}}{\left[\mu_p + \left(\dfrac{\tau_y}{|\dot{\gamma}|} \right) \right]} = \dfrac{\tau_{ij}}{\eta} & \text{for } \tau \geq \tau_y \\ 0 & \text{for } \tau < \tau_y \end{cases} \tag{3.16}$$

When the magnitude of the shear stress $|\tau|$ is greater than the yield stress τ_y, the material flows with an apparent viscosity given by:

$$\eta = \mu_p + \frac{\tau_y}{|\dot{\gamma}|}, \tag{3.17}$$

where μ_p is the viscosity of the deformed material, referred to as the plastic viscosity. The magnitudes of the shear stress and deformation rate are defined, respectively, as

$$|\tau| = \sqrt{\frac{1}{2}\tau_{ij}\tau_{ij}} \tag{3.18 a}$$

$$|\dot{\gamma}| = \sqrt{\frac{1}{2}e_{ij}e_{ij}} \tag{3.18 b}$$

using the summation convention for repeated indices. With the approximations noted in the preceding section, and assuming rotational symmetry, one then obtains

$$\dot{\gamma}_{rz} = \frac{\partial v_r}{\partial z} \tag{3.19 a}$$

$$\dot{\gamma}_{\phi z} = \frac{\partial v_\phi}{\partial z} \tag{3.19 b}$$

$$|\tau| = \sqrt{\tau_{rz}^{\ 2} + \tau_{\phi z}^{\ 2}} \tag{3.20 a}$$

$$|\dot{\gamma}| = \sqrt{\dot{\gamma}_{rz}^{\ 2} + \dot{\gamma}_{\phi z}^{\ 2}} \tag{3.20 b}$$

using the conventional index notation to describe the individual components.

It should be noted that it is not possible to explicitly express the deviatoric stress in terms of the rate-of-deformation for a region where the stress is below the yield value, τ_y. The areas where $|\tau| < \tau_y$ have a zero rate-of-deformation, hence they translate like a

rigid solid. Thus, this numerical method will neglect any unsheared region which might exist outside the boundary layer region, and instead focus on the sheared region which flows with apparent viscosity, η. It follows that the apparent viscosity for a Bingham plastic fluid takes the following form

$$\eta = \mu_p + \frac{\tau_y}{\left[\left(\frac{\partial v_r}{\partial z}\right)^2 + \left(\frac{\partial v_\phi}{\partial z}\right)^2\right]^{\frac{1}{2}}} \tag{3.21}$$

For cylindrical coordinates, the two pertinent stress components in the plastic region assume the following forms:

$$\tau_{z\phi} = \tau_{\phi z} = \eta\left[\frac{\partial v_\phi}{\partial z} + \frac{1}{r}\frac{\partial v_z}{\partial \phi}\right] \tag{3.22}$$

$$\tau_{zr} = \tau_{rz} = \eta\left[\frac{\partial v_r}{\partial z} + \frac{\partial v_z}{\partial r}\right] \tag{3.23}$$

For $\left(\partial/\partial z >> \partial/\partial \phi \text{ and } \partial/\partial r\right)$ following boundary layer theory, the tangential component, $\tau_{\phi z}$, and the radial component, τ_{rz}, of the stress tensor become

$$\tau_{\phi z} = \eta\frac{\partial v_\phi}{\partial z} \tag{3.24}$$

$$\tau_{rz} = \eta\frac{\partial v_r}{\partial z} \tag{3.25}$$

Substitution of equation (3.21) into (3.24) and (3.25), gives

$$\tau_{\phi z} = \left\{ \mu_p + \frac{\tau_y}{\left[\left(\frac{\partial v_r}{\partial z} \right)^2 + \left(\frac{\partial v_\phi}{\partial z} \right)^2 \right]^{\frac{1}{2}}} \right\} \left(\frac{\partial v_\phi}{\partial z} \right) \tag{3.26}$$

$$\tau_{rz} = \left\{ \mu_p + \frac{\tau_y}{\left[\left(\frac{\partial v_r}{\partial z} \right)^2 + \left(\frac{\partial v_\phi}{\partial z} \right)^2 \right]^{\frac{1}{2}}} \right\} \left(\frac{\partial v_r}{\partial z} \right) \tag{3.27}$$

These are the components of stress required to close the momentum equations given by Eqs. (3.8) and (3.9).

A useful parameter is the "Bingham Number", which is the ratio of the yield stress, τ_y, to viscous stress. It is used to assess the viscoplastic character of the flow and is defined as:

$$B_y = \frac{\tau_y}{\mu_p \frac{V}{l}} \tag{3.28}$$

which is expressed by the following relation (Matsumoto et al., 1982):

$$B_y = \frac{\tau_y}{2\rho\ \Omega r (\kappa\Omega)^{\frac{1}{2}}}, \tag{3.29}$$

where κ is the kinematic plastic viscosity of the fluid, $\kappa = \mu_p / \rho$, l is a characteristic length scale, and r indicates that this a local Bingham number.

It is possible to reduce the continuity and momentum equations to a set of ordinary differential equations by substitution of equations (3.12 a, b, c, d) for velocity, equations (3.26) and (3.27) for the shear stress components, and equation (3.29) for the ratio B_y, into equations (3.7) to (3.10) (see Appendix A). This was accomplished with the aid of Maple software, and the resultant equations are presented below.

Continuity Equation

$$2F + H' = 0 \tag{3.30}$$

Momentum Equations

r-wise

$$F'' = \left[F^2\left(F'^2 + G'^2\right)^{\frac{1}{2}} F'^2 + F^2\left(F'^2 + G'^2\right)^{\frac{1}{2}} G'^2 - G^2\left(F'^2 + G'^2\right)^{\frac{1}{2}} F'^2 + 2B_y G'F'G'' \right.$$
$$\left. - G^2\left(F'^2 + G'^2\right)^{\frac{1}{2}} G'^2 + F'^3 H\left(F'^2 + G'^2\right)^{\frac{1}{2}} + F'H\left(F'^2 + G'^2\right)^{\frac{1}{2}} G'^2 \right]$$
$$\left(F^2\left(F'^2 + G'^2\right)^{\frac{1}{2}} F'^2 + F^2\left(F'^2 + G'^2\right)^{\frac{1}{2}} G'^2 + 2B_y G'^2 \right)^{-1} \tag{3.31}$$

ϕ-wise

$$G'' = \left[2FG\left(F'^2 + G'^2\right)^{\frac{1}{2}} F'^2 + 2FG\left(F'^2 + G'^2\right)^{\frac{1}{2}} G'^2 + G'H\left(F'^2 + G'^2\right)^{\frac{1}{2}} F'^2 \right.$$
$$\left. + G'^3 H\left(F'^2 + G'^2\right)^{\frac{1}{2}} + 2B_y F'G'F'' \right]$$
$$\left(F^2\left(F'^2 + G'^2\right)^{\frac{1}{2}} F'^2 + \left(F'^2 + G'^2\right)^{\frac{1}{2}} G'^2 + 2B_y F'^2 \right)^{-1} \tag{3.32}$$

z-wise

$$P' = HH' - H'', \tag{3.33}$$

where a prime denotes differentiation with respect to ζ.

Since the last equation, (3.33), is the only one involving $P(\zeta)$, it may be integrated directly to give

$$P(\zeta) = P(0) + \frac{1}{2} H^2(\zeta) + 2F(\zeta) \tag{3.34}$$

where $P(0)$ is the value of P at the disk. Hence no numerical integration for P is necessary once F and H are determined.

For solution purposes, it is advantageous to eliminate the second derivatives on the right hand side of equations (3.31) and (3.32) so as to obtain a single second order variable for each equation. Algebraic calculations yield:

$$\begin{aligned} F'' = & \Big[2F^2 B_y F'^2 - G'^2 G^2 \left(F'^2 + G'^2\right)^{\frac{1}{2}} + G'^2 F' H \left(F'^2 + G'^2\right)^{\frac{1}{2}} \\ & - G^2 F'^2 \left(F'^2 + G'^2\right)^{\frac{1}{2}} + 2B_y G'^2 F' H + F^2 G'^2 \left(F'^2 + G'^2\right)^{\frac{1}{2}} + 4B_y F F' G G' \\ & + F'^3 H \left(F'^2 + G'^2\right)^{\frac{1}{2}} + F^2 F'^2 \left(F'^2 + G'^2\right)^{\frac{1}{2}} + 2B_y F'^3 H - 2B_y F'^2 G^2 \Big] \\ & \left(2B_y G'^2 + \left(F'^2 + G'^2\right)^{\frac{1}{2}} F'^2 + \left(F'^2 + G'^2\right)^{\frac{1}{2}} G'^2 + 2B_y F'^2 \right)^{-1} \end{aligned} \tag{3.35}$$

$$\begin{aligned} G'' = & \Big[2B_y G'^3 H + G'^3 H \left(F'^2 + G'^2\right)^{\frac{1}{2}} + 2B_y G' F' F^2 + 4B_y G'^2 F G \\ & + 2FGG'^2 \left(F'^2 + G'^2\right)^{\frac{1}{2}} - 2B_y G^2 G' F' + 2B_y G' F'^2 H \\ & + F'^2 G' H \left(F'^2 + G'^2\right)^{\frac{1}{2}} + 2FGF'^2 \left(F'^2 + G'^2\right)^{\frac{1}{2}} \Big] \\ & \left(2B_y G'^2 + \left(F'^2 + G'^2\right)^{\frac{1}{2}} G'^2 + \left(F'^2 + G'^2\right)^{\frac{1}{2}} F'^2 + 2B_y F'^2 \right)^{-1} \end{aligned} \tag{3.36}$$

The resultant equations can be considered as a generalized case including both Bingham and Newtonian fluids, since setting B_y = 0 will simplify these equations to represent a Newtonian fluid, i.e.,

$$2F + H' = 0 \tag{3.37}$$

$$F'' = F^2 - G^2 + F'H, \tag{3.38}$$

$$G'' = 2FG + G'H, \tag{3.39}$$

$$P' = HH' - H'', \tag{3.40}$$

The constitutive equation of the Bingham fluid has generated additional non-linear terms in the momentum equations in comparison to the equations for a Newtonian fluid. Equations (3.35) and (3.36) are second order in both *F* and *G*, and first order in *F, G* and *H*. Therefore, we expect five arbitrary constants to appear in the general solutions for *F, G* and *H*, which are determined from the five boundary conditions given by (3.13) and (3.14).

3.3.2 Power-Law Model

As indicated in the literature review, power-law fluids have been considered by some researchers (Andersson et al., 2001). We include it in this study as a validation of the analysis being used for the Bingham fluid. Here we will only list the resulting ODEs. The development of these equations is given in Appendix B. The resulting ODEs are as follows:

$$H' = -2F - \frac{(1-n)F'\zeta}{n+1} \tag{3.41}$$

$$F'' = \left(F^2 - G^2 + \left(H + \frac{(1-n)F\zeta}{n+1} \right) F' \right) \left(1 + \frac{(n-1)G'^2}{F'^2 + G'^2} \right) - (n-1)F'G' \\ \left(2FG + \left(H + \frac{(1-n)F\zeta}{n+1} \right) G' \right) \left(F'^2 + G'^2 \right)^{-1} \left(n \left(F'^2 + G'^2 \right)^{\left(\frac{1}{2}n - \frac{1}{2} \right)} \right)^{-1} \tag{3.42}$$

$$G'' = \left(2FG + \left(H + \frac{(1-n)F\zeta}{n+1} \right) G' \right) \left(1 + \frac{(n-1)F'^2}{F'^2 + G'^2} \right) - (n-1)F'G' \\ \left(F^2 - G^2 + \left(H + \frac{(1-n)F\zeta}{n+1} \right) F' \right) \left(F'^2 + G'^2 \right)^{-1} \left(n \left(F'^2 + G'^2 \right)^{\left(\frac{1}{2}n - \frac{1}{2} \right)} \right)^{-1} \tag{3.43}$$

3.4 Numerical Solution of Governing Equations

From the basic theory of ODEs, there are two ways to solve the nonlinear second-order system of ODEs, either as an initial value problem (IVP) or boundary value problem (BVP). One of the most popular methods for solving the general BVP is the shooting method (Roberts and Shipman, 1972). With the simple shooting method, one turns the BVP into a first-order IVP, and tries to obtain the solution based on a set of unspecified initial conditions which are then corrected through an iterative procedure (e.g., Newton's method) to satisfy the boundary conditions. This procedure requires the transformation into the state-space form and also requires evaluation of the Jacobian. The success of the procedure depends on using an appropriate initial guess.

The three sets of the ODEs given by equations (3.30), (3.35) and (3.36) for Bingham fluids, (3.37) to (3.39) for Newtonian fluids and (3.41) to (3.43) for power-law fluids represent a "two-point boundary value problems" (TPBVP) which must be solved numerically. Besides the shooting method, TPBVPs can also be solved by finite-

difference methods. However, difficulties have been reported in the literature when implementing these methods to solve the ODEs associated with similarity problems in fluid mechanics (Kafoussias et al., 1993). These difficulties are mostly attributed to the fact that the ODEs are often extremely sensitive to the choice of initial conditions (Ariel, 1992; Kafoussias et al., 1993; Andersson et al., 2001). In this case, the ODEs are indeed extremely sensitive to the initial guess, and both the single shooting method and the conventional finite-difference methods failed to converge even for the Newtonian case. This result notwithstanding, it is important to note that many techniques based on finite-difference formulations have been reported as successful in solving the problem of sensitive initial values (Holodniok et al., 1977; Ariel, 1992; Kafoussias et al., 1993).

An alternative approach is to use multiple shooting methods (Roberts and Shapman, 1972). Multiple shooting is a strategy that significantly enhances the stability of the shooting method. The approach has much in common with the single shooting method. The solution of the local BVP is also found by transforming the BVP into the IVP. The simple but very powerful idea behind this approach is to find solutions to the ODEs not over the full interval in a single step but to split the interval up into N sub-intervals. The solution in each of the sub-intervals is found by integrating the ODEs using the fourth-order Runge-Kutta method with variable step size, and then these solutions are matched using Newton's method. In this way we may think of it as being a compromise between the finite-difference and shooting methods. A full description of the multiple-shooting method for a two-point boundary value problem (TPBVP) is given by Roberts and Shapman (1972).

This method has been implemented in a subroutine called BVPMS contained in the International Mathematics and Statistics Libraries (IMSL). The routine BVPMS uses a multiple-shooting technique to solve the differential equation system $y' = f(x, y)$ with boundary conditions of the form, $g(y(a), y(b)) = 0$. A fourth-order Runge-Kutta algorithm is used to perform the integration. An adapted version of the IMSL routine BVPMS has been used by the author to solve the problem specified in the previous section. To obtain a solution to the present problem, the domain is divided into N = 40 sub-intervals. The nature of the problem requires a large number of BVPs to be solved. However, the procedure is fast, even in sequential processing, since the sub-intervals are short, with only a few integration points in each. The algorithm begins with a given initial guess [a, b] and iteratively corrects the initial value set using Newton's method. Details of the algorithm that is responsible of implementing the model are described in Appendix E. The following computations were run on a personal computer in FORTRAN double precision, using the FORTRAN power station compiler.

The system of coupled ordinary nonlinear differential equations given by (3.30), (3.35) and (3.36) for Bingham fluids are put into a standard form, suitable for numerical computation, by defining the functions

$$y_1 = F, \qquad y_2 = F', \qquad y_3 = G, \qquad y_4 = G', \qquad y_5 = H. \tag{3.44}$$

These functions will convert the two second order ODEs into five first order ODEs, which then are to be solved numerically. Following this approach, equations (3.30),

(3.35) and (3.36), together with the initial and boundary conditions given by (3.13) and (3.14), and the initial guesses $F'(0) = a$ and $G'(0) = b$ become

$$y'_1 = y_2 \qquad y_1(0) = 0 \tag{3.45}$$

$$\begin{aligned} y'_2 = \Big[& 2y_1^{\,2} B_y y_2^{\,2} - y_4^{\,2} y_3^{\,2} \left(y_2^{\,2} + y_4^{\,2}\right)^{\frac{1}{2}} + y_4^{\,2} y_2 y_5 \left(y_2^{\,2} + y_4^{\,2}\right)^{\frac{1}{2}} \\ & - y_3^{\,2} y_2^{\,2} \left(y_2^{\,2} + y_4^{\,2}\right)^{\frac{1}{2}} + 2B_y y_4^{\,2} y_2 y_5 + y_1^{\,2} y_4^{\,2} \left(y_2^{\,2} + y_4^{\,2}\right)^{\frac{1}{2}} + 4B_y y_1 y_2 y_3 y_4 \\ & + y_2^{\,3} y_5 \left(y_2^{\,2} + y_4^{\,2}\right)^{\frac{1}{2}} + y_1^{\,2} y_2^{\,2} \left(y_2^{\,2} + y_4^{\,2}\right)^{\frac{1}{2}} + 2B_y y_2^{\,3} y_5 - 2B_y y_2^{\,2} y_3^{\,2} \Big] \\ & \left(2B_y y_4^{\,2} + \left(y_2^{\,2} + y_4^{\,2}\right)^{\frac{1}{2}} y_2^{\,2} + \left(y_2^{\,2} + y_4^{\,2}\right)^{\frac{1}{2}} y_4^{\,2} + 2B_y y_2^{\,2}\right)^{-1} \end{aligned}$$

$$y_2(0) = a \tag{3.46}$$

$$y'_3 = y_4 \qquad y_3(0) = G(0) \tag{3.47}$$

$$\begin{aligned} y'_4 = \Big[& 2B_y y_4^{\,3} y_5 + y_4^{\,3} y_5 \left(y_2^{\,2} + y_4^{\,2}\right)^{\frac{1}{2}} + 2B_y y_4 y_2 y_1^{\,2} + 4B_y y_4^{\,2} y_1 y_3 \\ & + 2y_1 y_3 y_4^{\,2} \left(y_2^{\,2} + y_4^{\,2}\right)^{\frac{1}{2}} - 2B_y y_3^{\,2} y_4 y_2 + 2B_y y_3 y_2^{\,2} y_5 \\ & + y_2^{\,2} y_3 y_5 \left(y_2^{\,2} + y_4^{\,2}\right)^{\frac{1}{2}} + 2y_1 y_3 y_2^{\,2} \left(y_2^{\,2} + y_4^{\,2}\right)^{\frac{1}{2}} \Big] \\ & \left(2B_y y_3^{\,2} + \left(y_2^{\,2} + y_4^{\,2}\right)^{\frac{1}{2}} y_3^{\,2} + \left(y_2^{\,2} + y_4^{\,2}\right)^{\frac{1}{2}} y_2^{\,2} + 2B_y y^{\,2}\right)^{-1} \end{aligned}$$

$$y_4(0) = b \tag{3.48}$$

$$y'_5 = -2\, y_1 \qquad y_5(0) = 0 \tag{3.49}$$

where for each equation, the initial condition is specified on the right hand margin.

Owing to the nonlinearity of the system, a parameterization of the problem was necessary in order to attain convergence. This can be done by using the so-called continuation method (Deuflhard et al., 1976) in conjunction with the multiple shooting method. Usually, the nonlinear system is partitioned into its linear and nonlinear parts, where nonlinear terms are multiplied by some continuation parameters, whose values range between 0 and 1. These parameters are initially set to zero, in which case only the linear part of the system takes effect. After the solution is readily found for the linear terms, the values of the continuation parameters are gradually increased to obtain a sequence of solutions that converges to the actual solution. This procedure, however, may take a long time to achieve the required solution, depending on the nonlinearity of the problem (Kaya and Noakes, 1998). The system was embedded in a one-parameter family $y' = f(x, y, q)$, with boundary conditions $g(y(a), y(b), q) = 0$, where $q = 0$ gives the linear problem and $q = 1$ represents the full nonlinear formulation. The routine BVPMS automatically moves the parameter from q = 0 toward q = 1.

The numerical solution, which satisfies equations (3.45) to (3.49), was obtained by the above-mentioned multiple-shooting method. In the computation, the far-field boundary ($\zeta \rightarrow \infty$) is replaced by a sufficiently large value, $\zeta(\infty)$, which is determined by numerical experiments (Owen and Rogers, 1987). Typically, $\zeta(\infty) \approx 10$ is used to represent the far-field flow behavior. In the present case, the boundary conditions at infinity could not be satisfied using either the finite-difference method or the single shooting method, but with the multiple shooting method convergence was obtained.

Having determined a successful solution technique, the system of Eqs. (3.45) to (3.49) was solved numerically for different values of the Bingham number, B_y. The program was run for fifteen values of B_y ranging in increments of 0.1 from 0 to 1 and increments of 0.5 from 1 to 3. This covers a reasonable range of values for common industrial fluids as characterized by their yield stress.

3.5 Summary

In this chapter, the flow of a Bingham fluid over a rotating disk was considered. The flow is characterized by the dimensionless yield stress "Bingham number", B_y, which is the ratio of the yield and local viscous stresses. Using von Kármán's similarity transformation, and introducing the rheological behavior law of the fluid into the conservation equations, the corresponding nonlinear two-point boundary value problem is formulated. A solution to the problem under investigation is obtained by a numerical integration of the set of Ordinary Differential Equations (ODEs), using a multiple shooting method, which employs a fourth order Runge–Kutta method to implement the numerical integration of the equations, and Newton iteration to determine the unknowns $F'(0)$ and $G'(0)$. Results of the numerical model will be presented in the following chapter.

CHAPTER 4

Results and Discussion of the Numerical Model

4.1 Introduction

For a disk rotating in a Bingham fluid, viscous effects are typically confined within a thin layer near the surface. At larger distances from the disk, the shear rates and related stresses decrease. In fact, if the yield stress of the material is larger than the magnitude of the shear stress produced in the fluid, a so called "plug flow" region occurs. The unsheared region is separated from the shear flow region by a yield surface on which the shear stress is equal to the yield stress.

Application of the present analysis is limited to flows where the shear stress exceeds the yield stress in the region adjacent to the disk surface. Typically the shear stresses have appreciable values in this region. We believe that this is a reasonable approximation for many Bingham fluids at practical rotation rates. In this investigation, for a wide range of yield values, we observed that the magnitude of the shear stress tensor, $|\tau|$, always exceeded the yield stress in the boundary layer region, and even beyond that region in the case of relatively low yield stress values. Thus, the numerical solution neglected any unsheared region which might exist outside the boundary layer

region, and instead focused on the sheared region in which the fluid flows with apparent viscosity, η.

In this chapter the results of the numerical simulation of boundary layer flow of a Bingham fluid over a rotating disk are presented. Special attention is paid to the velocity field, the torque exerted on the disk, the boundary layer thickness and the volumetric flow rate produced by the rotation of the disk.

Although the multiple shooting method was adopted to relieve the well known sensitivity to the initial guess of the shooting method as discussed by Andersson et al., 2001 and Denier and Hewitt (2004), severe difficulties were still existing for the shear thinning fluids (i.e., $n < 1$). Therefore, the results for only one class of the power-law fluids, shear thickening fluids (i.e., $n > 1$) are presented as a validation of the numerical technique.

4.2 Velocity Field

The velocity fields exhibit some general features for all types of fluids. The dimensionless velocity distributions are given by F in the radial direction, G in the tangential direction and H in the axial direction. These functions have been defined in Chapter 3 by Eqs. 3.12 a-c. Consider first the case of a Newtonian fluid: the computed velocity profiles F, G and H are plotted in Figs. 4.1 versus the dimensionless axial distance, ζ, (Eq. 3.11). The rotating disk acts like a pump, drawing fluid axially inward from the surroundings toward the disk surface. However, because the surface is solid, the

inflowing fluid finds its path blocked and is redirected in the radial direction. The fluid far away from the plane of rotation, i.e., $\zeta \rightarrow \infty$, does not rotate but moves in a purely axial direction. The axial velocity, H, starting from its maximum negative value at $\zeta(\infty)$, decreases steadily as the disk is approached due to the fluid being redirected in the radial direction. Since the radial component, F, is zero both at the disk surface and in the ambient fluid, there must be a maximum value somewhere in between. The maximum value is positive since the radial flow is always outward along the disk. The tangential velocity component, G, is driven by the rotation of the disk. It increases with decreasing axial distance ζ, reaching a maximum value at the plate. Consequently, the shear stress also increases with decreasing ζ (approaching the disk surface).

The numerical results are also compared to published values for the dimensionless velocity profiles (Ostrach and Thornton, 1958) [OT] in Fig. 4.1. The figure demonstrates that the numerical results are in good agreement with the published results. The main features of the numerical curves are summarized as follows:

- While the tangential velocity, G, decreases continuously due to viscous diffusion, the radial velocity, F, peaks at $\zeta = 0.9$. On the surface of the disk the radial velocity is zero due to the no-slip condition. Far away from the disk, the radial velocity is significantly reduced as the tangential component responsible for the radial acceleration decreases rapidly.
- From the continuity equation (Eq. 3.30):

$$H = 2Fd\,\zeta \tag{4.1}$$

Because F decays rapidly at large ζ, H approaches an asymptotic value at finite value of ζ, far away from the disk, there is a constant dimensionless axial velocity of $-H(\infty) \approx 0.8823$ towards the rotating disk which is set up by the combined action of viscous diffusion and centripetal acceleration. Despite, the presumed uniqueness of the solution of the rotating disk problem, different models give slightly different values for the axial inflow. Schlichting (1979) and Andersson et al. (2001) have reported slightly higher values for the axial inflow than the present simulation, i.e., $-H(\infty) = 0.88446$ and 0.883, respectively. The value of Ostrach and Thornton (1958) was $-H(\infty) = 0.8843$.

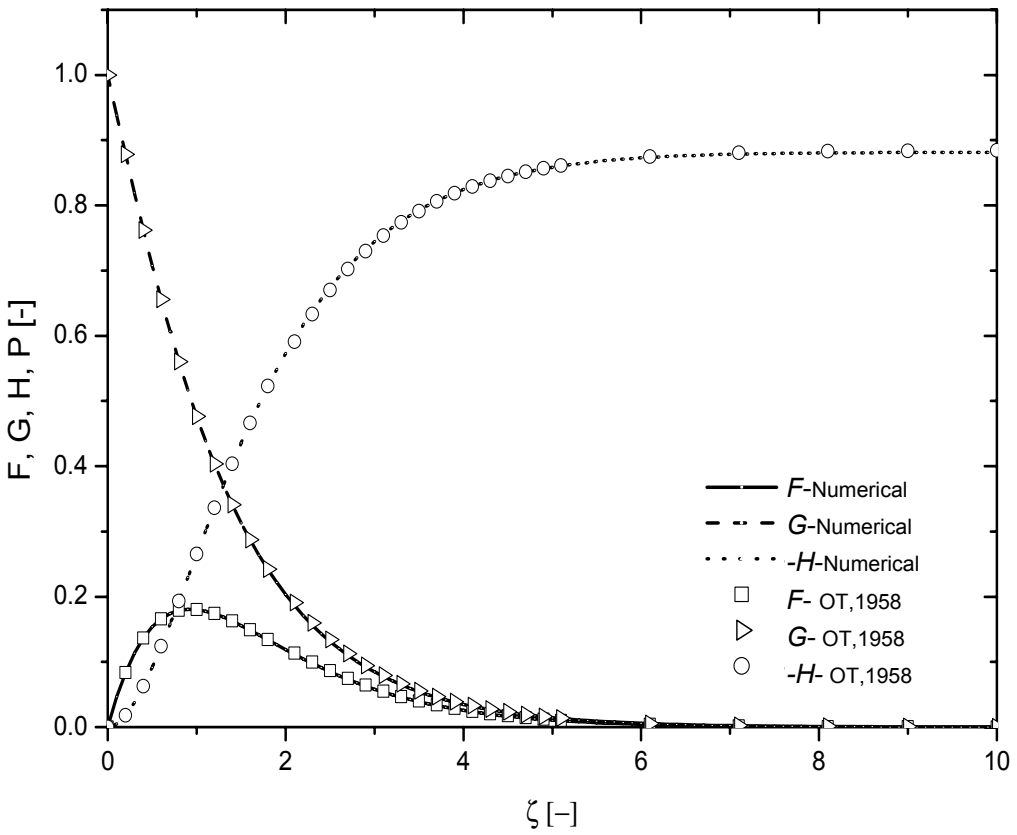

Figure 4.1: Velocity distribution near a rotating disk for a Newtonian fluid

Due to the sensitivity of the problem, precise values of the two missing boundary conditions $F'(0)$ and $G'(0)$ are required; these represent the derivatives of the dimensionless radial and tangential velocity functions at the disk surface, respectively. The present solution to the problem determines the following values (six digits) for $F'(0)$ and $G'(0)$ that were also predicted by Lance and Rogers (1961):

$$F'(0) = 0.510232 \tag{4.2}$$

$$G'(0) = -0.615922 \tag{4.3}$$

This level of accuracy is necessary for an accurate calculation of heat and mass transfer from a rotating disk (Millsaps and Pohlhausen, 1952; Sparrow and Gregg, 1960; Hansford and Litt, 1968; Rashaida et al., 2005). The derivatives, F' and G', along the axial direction are shown in Fig. 4.2 and outlined along with the dimensionless velocity

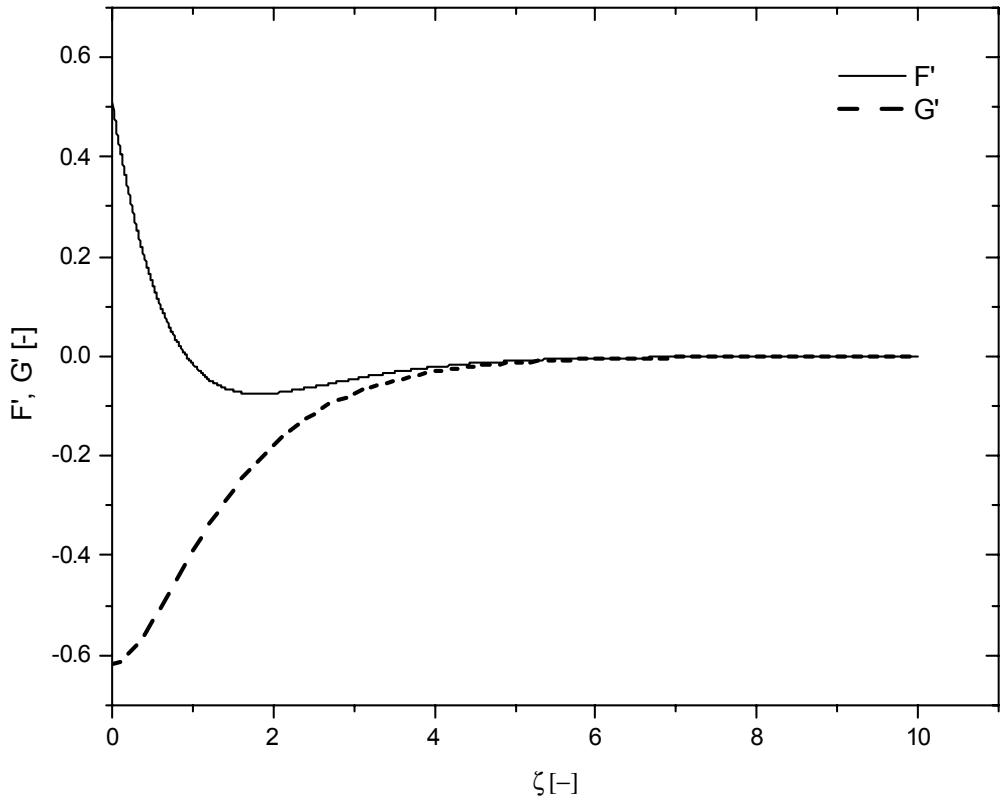

Figure 4.2: Distributions of F' and G', along axial direction for a Newtonian fluid

profiles in Table C.1, Appendix C.

Validation of the present numerical method was also achieved by obtaining the numerical solution for the case of power-law fluids. The sample results in Fig. 4.3 exhibit the same features as in the Newtonian case. A comparison with the results reported by Andersson et al. (2001) is given in Table 4.1. Consideration of the data shows that the values of $G'(0)$ and $H(\infty)$ in the present simulation differ by as much as 19% and 7%, respectively, from that of Andersson et al. (2001) for high shear thickening fluids (n = 1.5 and 2). The value of $F'(0)$ is within 0.5% of the values of Andersson et al. (2001).

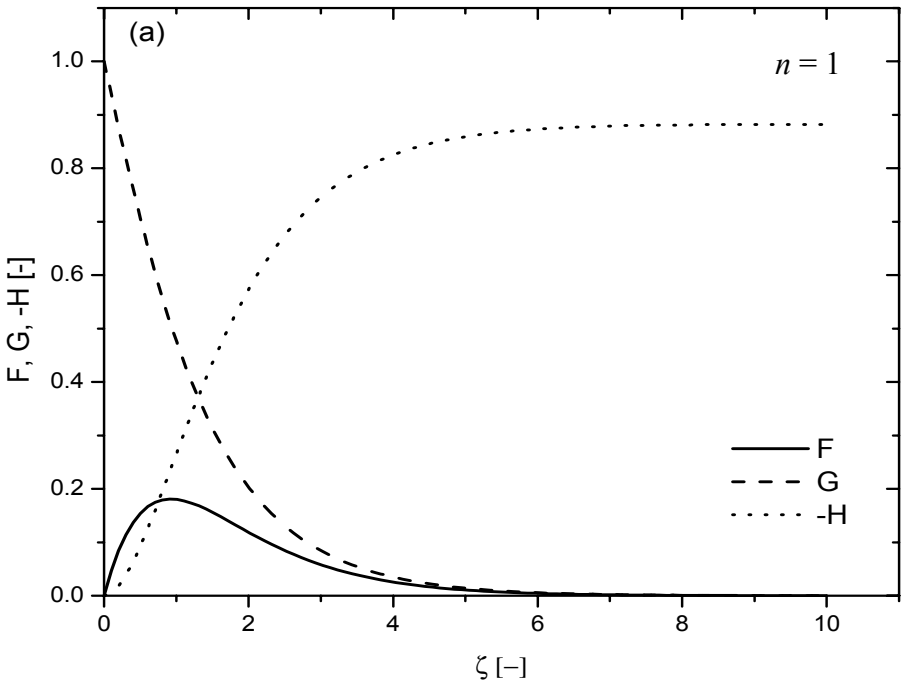

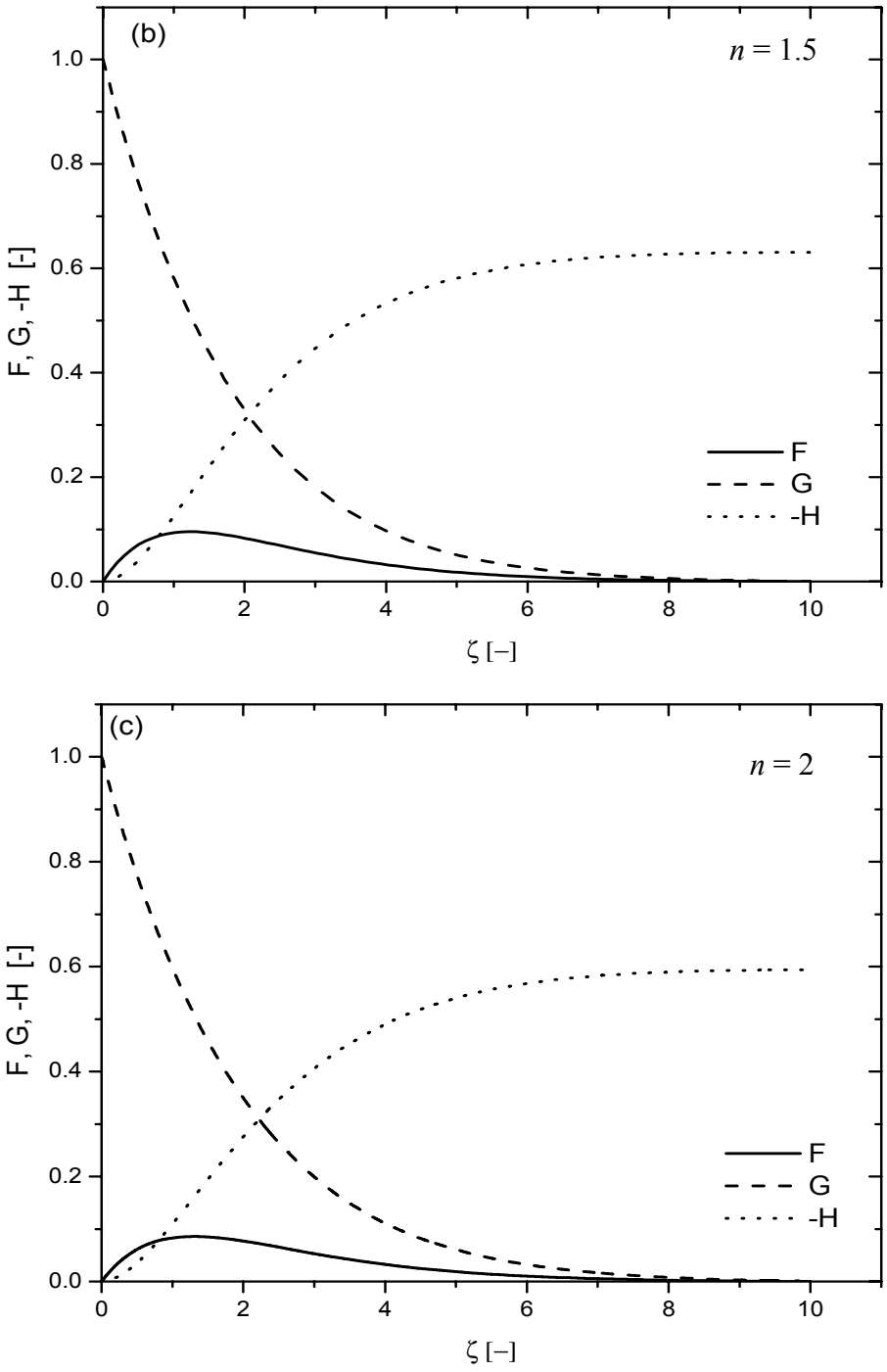

Figure 4.3: Variation of the dimensionless velocity profiles, F, G and H, with the axial dimensionless distance, ζ, for different value of power-law index, n. (a): n =1, (b): n = 1.5 and (c): n = 2

Table 4.1: Comparison of some characteristics of the present calculations with numerical results of Andersson et al. (2001) for power-law fluids

Power-law index n	$F'(0)$		$-G'(0)$		$-H(\infty)$	
	Present	Andersson	Present	Andersson	Present	Andersson
1	0.5102	0.510	0.6159	0.616	0.8822	0.883
1.5	0.5282	0.529	0.5298	0.601	0.6319	0.676
2	0.5449	0.547	0.5085	0.603	0.5939	0.586

Next, consider a Bingham fluid, for which the flow is characterized by the dimensionless yield stress Bingham number, B_y. Physically, the Bingham number is the ratio of the yield stress of a Bingham plastic fluid to the tangential shear stress induced in a fluid of viscosity μ_p on a rotating disk. The Bingham number varies with the radial location (local) and rotation rate. The smaller the radial distance, the larger the Bingham number. The Bingham number decreases as the rotation rate increases. As seen, the Bingham number is an important dimensionless number for rotating disk flow. The computed velocity profiles F, G and H are plotted in Fig.4.4 versus the dimensionless axial distance, ζ, for different values of Bingham number, B_y. From the results obtained for $B_y > 0$, the following trends can be noted for the dimensionless axial, radial and tangential velocity components, respectively:

1. Axial Velocity Distribution

As can be seen from the Fig. 4.5, the value of $-H(\infty)$, the asymptotic limiting value of the axial velocity, decreases with an increase in the value of B_y, implying that the quantity of fluid drawn in from the surroundings decreases. In comparison with the case of a

Newtonian fluid, $B_y = 0$, the flow of a Bingham fluid produced by the rotation of the disk, is reduced due to the yield stress characteristics of the fluid. The greater the Bingham number, the stronger this effect.

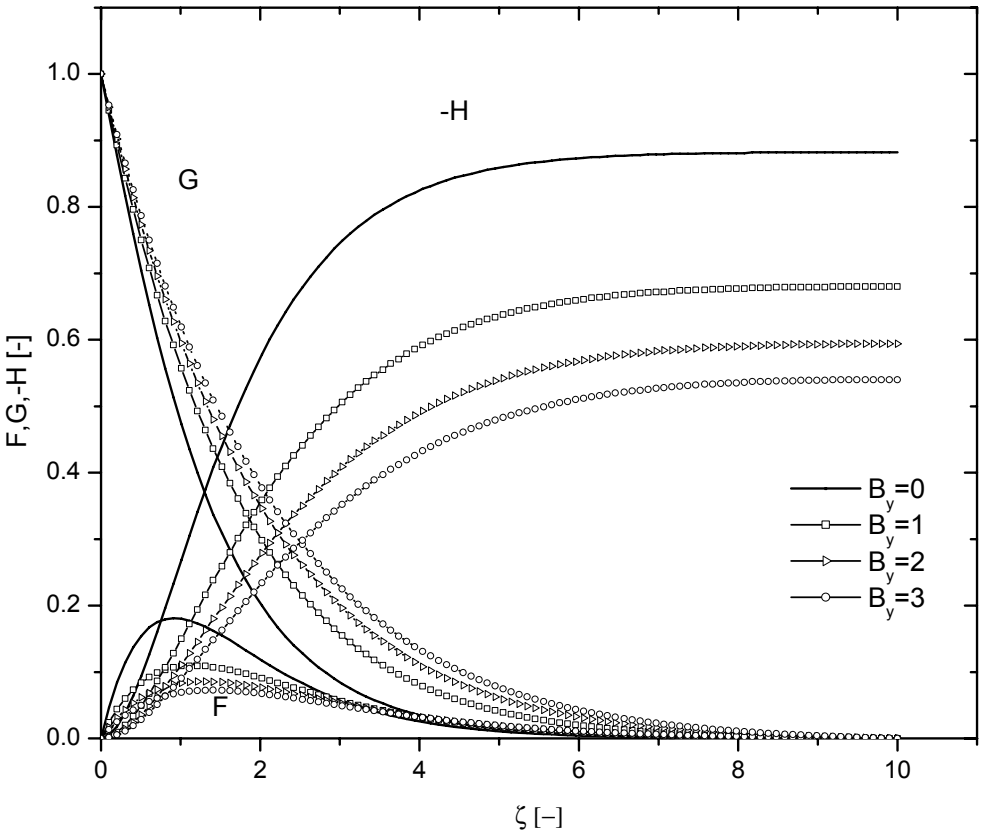

Figure 4.4: Variation of the dimensionless velocity profiles, F, G and H, with the axial dimensionless distance, ζ, for different values of Bingham number, B_y

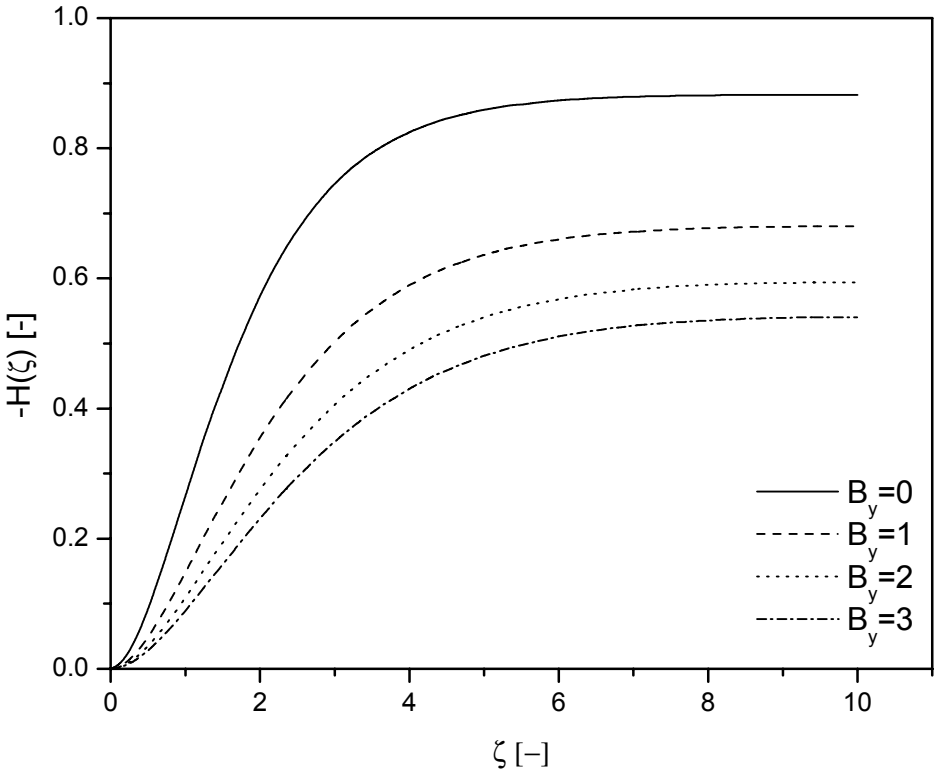

Figure 4.5: Variation of the axial velocity profile, H, with ζ, for different values of Bingham number, B_y

2. Radial Velocity Distribution

Representative radial velocity distributions are given in Fig. 4.6. As noted previously, since the radial velocity is zero at both the surface of the disk and in the far field, there must be a maximum value somewhere in between. The profile of the radial velocity component shown in Fig. 4.6 becomes flatter as the value of B_y is increased, i.e., the maximum velocity decreases, and its location moves slightly further from the disk. For $B_y > 0$, the radial outflow must carry away the incoming axial flow with an apparent viscosity now consisting of two parts, i.e., the Bingham plastic viscosity and the yield stress. Thus, the level of the radial velocity component decreases with increasing B_y, and

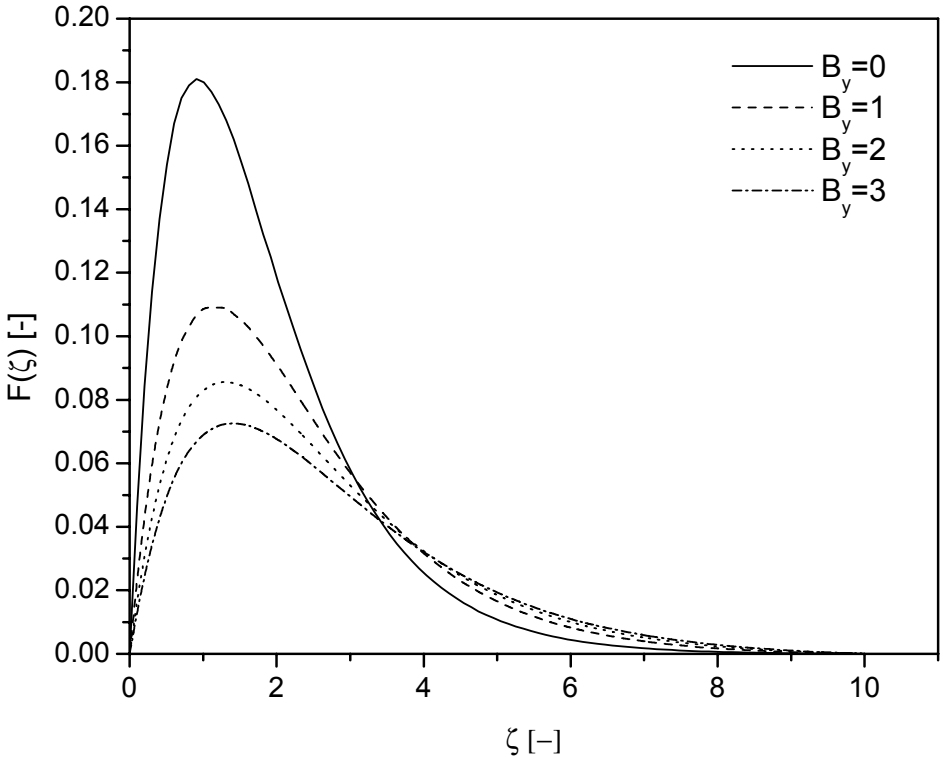

Figure 4.6: Variation of the radial velocity profile, F, with ζ, for different values of Bingham number, B_y

also persists a longer distance from the disk before it vanishes. Notice the cross-over point of the curves near $\zeta = 3.5$, showing that although increasing Bingham number decreases the velocity near the disk, it increases the velocity far from the disk.

3. Tangential Velocity Distribution

The tangential velocity is driven by the action of viscosity and the rotation of the disk. It is readily seen from Fig. 4.7 that the profile of the tangential velocity component, G,

follows the same trend as that of the Newtonian fluid, i.e. an exponentially decaying function of ζ. As B_y is increased, the shear-driven motion represented by G also increases.

Overall, all velocity components require a longer distance from the disk to approach their asymptotic values as B_y is increased (see Figs. 4.5-4.7). Accordingly, in the numerical solution process, the value of $\zeta(\infty)$ has to be increased for larger values of B_y in order to obtain accurate results. For example, with a Newtonian fluid a value of $\zeta(\infty) = 6$ is usually considered large enough (Ariel, 1992). However, for the range of Bingham numbers considered in this study (B_y = 0 to 3), values of $\zeta(\infty)$ as large as 10 were used in the present algorithm.

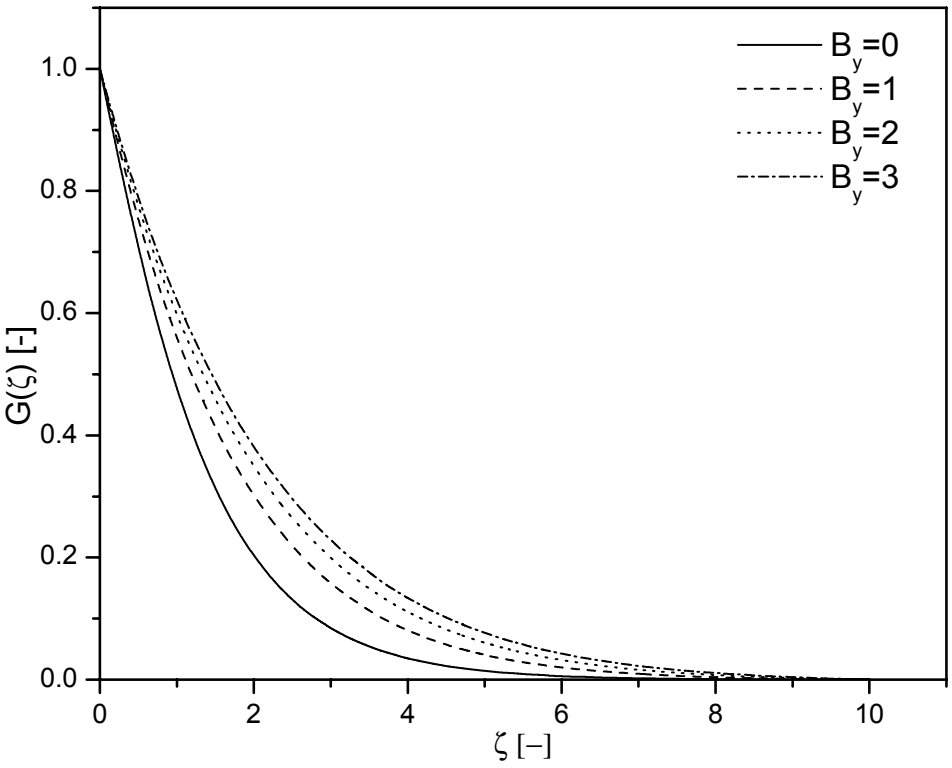

Figure 4.7: Variation of the tangential velocity profile, G, with ζ, for different values of Bingham number, B_y

It is of practical interest to determine $F'(0)$ and $G'(0)$. A list of these values as a function of Bingham number is given in Table 4.2. Corresponding velocity profiles can be generated using these initial values. Moreover, it will be shown in the next section that $F'(0)$ and $G'(0)$ are required to compute the torque.

Table 4.2: Values of the functions $F'(0)$ and $G'(0)$ for different values of B_y

B_y	$F'(0)$	$G'(0)$
0.0	0.5102	-0.6159
0.1	0.4598	-0.6124
0.2	0.4197	-0.6070
0.3	0.3869	-0.6007
0.4	0.3596	-0.5941
0.5	0.3363	-0.5873
0.6	0.3164	-0.5806
0.7	0.2989	-0.5741
0.8	0.2836	-0.5678
0.9	0.2700	-0.5617
1.0	0.2578	-0.5558
1.5	0.2119	-0.5298
2.0	0.1814	-0.5085
2.5	0.1595	-0.4906
3.0	0.1429	-0.4754

4.3 Torque and Shear Rate

The action of viscosity in the fluid adjacent to the disk creates a tangential shear stress which opposes the rotation of the disk. As a consequence, to sustain steady rotation of the disk, it is necessary to apply a torque at the shaft. This turning torque is equivalent to the resisting moment due to friction. If we neglect edge effect, it can be calculated from the product of the shear stress at the wall, the surface area and the moment arm integrated over the surface of the disk. The neglect of the edge effect is justified if the radius is large compared with the thickness of the boundary layer. The contribution of the frictional moment on an annular element of width dr at radius r is $dM = -2\pi r\, dr\, r\, \tau_{z\phi}$.

The total moment for a finite disk wetted on one side can be approximated by

$$M = -2\pi \int_0^R r^2 \tau_{z\phi}\, dr \tag{4.4}$$

using the infinite disk solution for $\tau_{z\phi}$. For the sheared fluid, $\tau_{z\phi}$ is given by equation (3.26), and takes the following form after substituting the dimensionless velocity relations and Bingham number (see Appendix C):

$$\tau_{z\phi} = \left[1 + \frac{2B_y}{\left(F'(0)^2 + G'(0)^2 \right)^{\frac{1}{2}}} \right] \Omega\, r\, G'(0)\, (\Omega\kappa)^{\frac{1}{2}}\, \rho \tag{4.5}$$

Given that the Bingham number is a function of r, we cannot proceed with the integration at this stage; instead we approximate the Bingham number by a value based on the tip of the disk ($r = R$) and refer to it as the global Bingham number, B_n. Substituting equation (4.5) into (4.4), and integrating from $r = 0$ to $r = R$ results in the following approximate expression for the total moment, M, acting on a disk wetted on both sides:

$$M \approx -\pi R^4 \left\{ \left[1 + \frac{2B_n}{\left(F'(0)^2 + G'(0)^2 \right)^{\frac{1}{2}}} \right] \Omega \, G'(0) \, (\Omega\kappa)^{\frac{1}{2}} \, \rho \right\} \tag{4.6}$$

The corresponding dimensionless torque coefficient, C_M, for a disk wetted on both sides can then be defined as:

$$C_M = \frac{-M}{\frac{1}{2}\rho\Omega^2 R^5} \tag{4.7}$$

Upon substitution of twice the moment given by equation (4.6) we obtain

$$C_M \approx -\frac{2\pi G'(0) \left(\kappa / \Omega \right)^{\frac{1}{2}}}{R} \left[1 + \frac{2B_n}{\left(F'(0)^2 + G'(0)^2 \right)^{\frac{1}{2}}} \right] \tag{4.8}$$

Note that this expression is only approximate due to the substitution of B_n for B_y in Eq. (4.5). For the Newtonian case, the Reynolds number does not enter into the definition of the basic flow. However, the Reynolds number does enter into various practical problems. There are different definitions of the Reynolds number for a Bingham fluid (Rashaida et. al., 2005), which makes comparison of different results problematic. The fluids considered in this thesis approach a Newtonian fluid at ambient temperature because the ratio of plastic viscosity to yield stress is high (a low yield stress and high plastic viscosity). Therefore, the use of the plastic viscosity of the Bingham fluid to formulate a Reynolds number is reasonable. Here and throughout the thesis we use a Reynolds number based on the disk radius, R, tip velocity, ΩR ,and plastic viscosity, μ_p, following Matsumoto et al., 1982, i.e.

$$\mathrm{Re}_\phi = \frac{\rho R^2 \Omega}{\mu_p} \tag{4.9}$$

For this Reynolds number relation, we can obtain the following expression for the torque coefficient:

$$C_M \approx -\frac{2\pi G'(0)}{\sqrt{\mathrm{Re}_\phi}}\left[1+\frac{2B_n}{\left(F'(0)^2+G'(0)^2\right)^{\frac{1}{2}}}\right] \tag{4.10}$$

The moment coefficient is plotted in Fig. 4.8 for different values of B_n. For each value of B_n, C_M was determined for Re_ϕ up to 10^5. In general, the C_M curves decrease as Re_ϕ increases. In order to illustrate the effect of the Bingham fluid on the magnitude of the turning moment on the disk, Fig. 4.8 includes the moment coefficient for $B_n = 0$ corresponding to a Newtonian fluid. Taking $B_n = 0.5$, corresponding to relatively a low value of Bingham number in this study, the value of C_M is increased above the Newtonian case by about 5% at $\mathrm{Re}_\phi = 10^4$. This increase rises to 30% for $B_n = 3$ at the same Reynolds number. These findings reflect the changes in tangential velocity profiles previously discussed. From Eq. (4.8), it can be concluded that for a Newtonian fluid ($B_n = 0$), $G'(0)$ is the most important parameter for determining C_M. However, for $B_y > 0$ the derivative of the radial velocity component, $F'(0)$, along with the yield stress, τ_y, also have a significant effect on the torque. These comments relate to the discussion at the beginning of this section and re-emphasizes the influence of the apparent viscosity on the tangential shear stress and hence the torque. This effect is more pronounced at low shear rates, where the apparent viscosity is more sensitive to the yield stress. This can be seen from Fig. 4.8, where at lower values of Re_ϕ the effect on C_M of increasing B_n is larger

compared to that at higher values. We conclude that one of the main effects of a Bingham fluid on a rotating disk is to increase the magnitude of the turning moment on the disk. Hence, we require more torque to rotate a disk in a Bingham fluid.

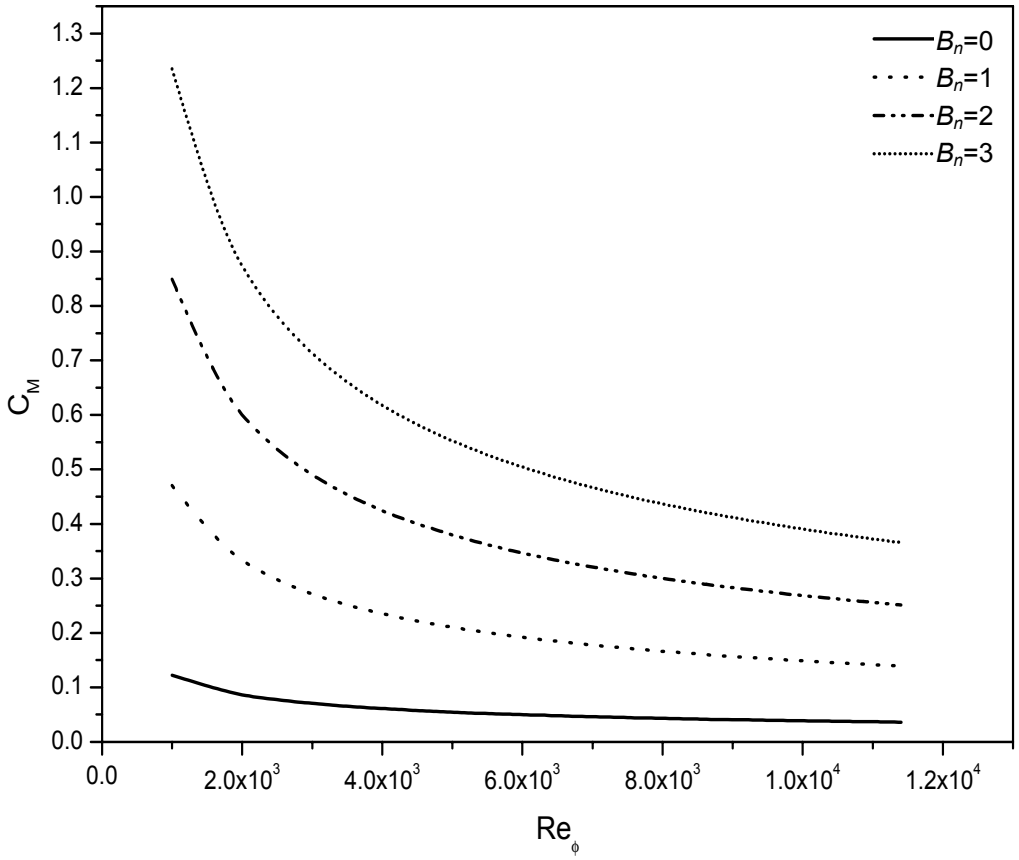

Figure 4.8: Variation of the dimensionless moment coefficient, C_M, with $R_{e\phi}$, for different values of B_n

It is of interest to compare the shear rates on the surface of the disk calculated from this numerical model to the shear rates at a simplified impeller wall (Wichterle et al., 1996; Lutz et al., 1996) and to the analytical solution for the wall shear rate on an infinite rotating disk flow (Schlichting, 1979). Analytically, the wall shear rate over the surface of the disk is generally estimated according to the rheological model of the Bingham fluid. It can be expressed by the following dimensionless function, which is derived in Appendix C.

$$\frac{\dot{\gamma}}{N} = 2\pi G'(0)\,\mathrm{Re}_{\phi}^{1/2}\left\{\left[1+\frac{2B_y}{\left[F'(0)^2+G'(0)^2\right]^{\frac{1}{2}}}\right]-\frac{2B_y}{G'(0)}\right\} \tag{4.11}$$

For $B_y = 0$, Eq. (4.11) reduces to the analytical solution of the wall shear rate on a rotating disk in a Newtonian fluid (Schlichting, 1979),

$$\frac{\dot{\gamma}}{N} = 3.88\,\mathrm{Re}_{\phi}^{1/2} \tag{4.12}$$

Figure 4.9 shows the variation of normalized wall shear rate on a rotating disk with Reynolds number in the range of laminar flow $\mathrm{Re}_{\phi} \le 10^5$. The variation is shown for different values of Bingham number, including the Newtonian case, $B_y = 0$. The solid symbols in Fig. 4.9 represent actual measurements on a simplified impeller (flat disk) of a centrifugal pump taken by Wichterle et al., 1996. It is seen that the shear rate for a Bingham fluid is higher than that for a Newtonian fluid, and that the higher the Bingham number the higher is the shear rate. We also conclude that the shear rate for the simplified impeller is almost the same as calculated from the von Kármán laminar boundary layer theory for a rotating disk (Eq. 4.12).

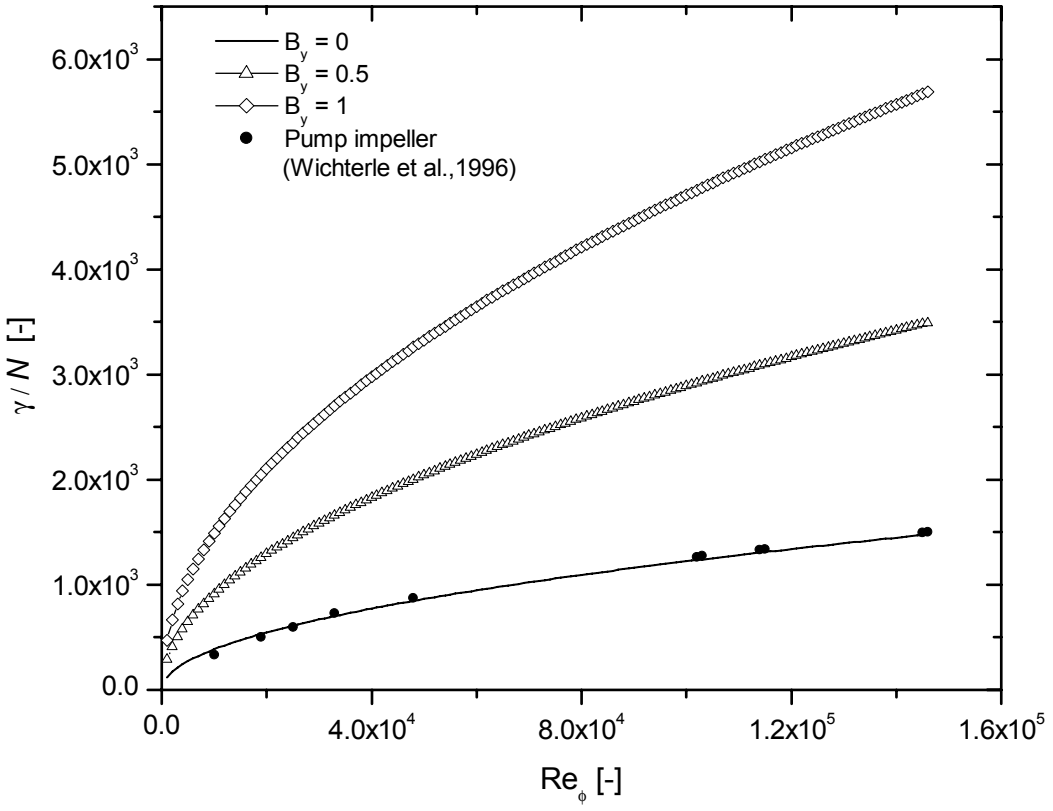

Figure 4.9: Comparison of the variation of the normalized shear rate vs. Reynolds number for Bingham and Newtonian fluids with that of an impeller of a centrifugal pump

4.4 Boundary Layer Thickness

The boundary layer thickness, δ, for a flow over a rotating disk is defined as the distance from the disk surface to where the tangential component of the fluid velocity is reduced to 0.01 of its value at the surface of the disk (Owen and Rogers, 1987). Thus, the tangential velocity is equal to $v_\phi = 0.01\omega r$, (i. e. G = 0.01). An expression for the

boundary layer thickness of a Bingham fluid flowing over a rotating disk is derived in Appendix C to be

$$\delta = \left\{ 1 + \frac{2B_y}{\left[F'(0)^2 + G'(0)^2 \right]^{\frac{1}{2}}} \right\} G'(0) \left(\frac{\kappa}{\Omega} \right)^{\frac{1}{2}} \tag{4.13}$$

The variation of the normalized boundary layer thickness, $\delta / (\kappa / \Omega)^{1/2}$, is shown in Fig 4.8 for different values of the Bingham number, B_y. It is clear that the boundary

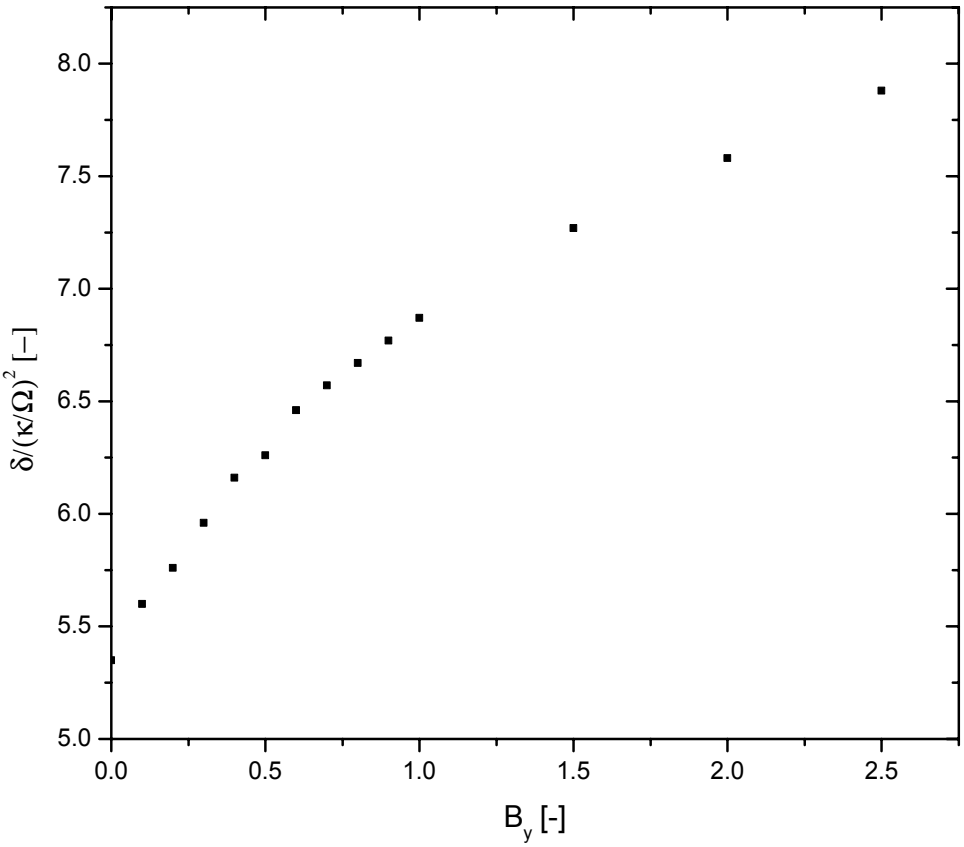

Figure 4.10: Normalized boundary layer thickness for different values of B_y

layer thickness increases with increasing Bingham number. The yield stress reduces both the axial and radial velocity components. The reduction in the radial velocity gives rise to the tangential shear stress (see Eq. 4.5), which is proportional to the tangential velocity. Consequently, the boundary layer thickness is increased as shown in Fig.4.8, where the tangential velocity components, G, claims 0.99% of its values.

4.5 Volumetric Flow Rate

The rotating disk resembles a centrifugal pump in so far as the disk imparts rotation to the fluid, which moves radially outwards and therefore, an axial motion develops towards the disk in order to satisfy continuity. It is obvious from this pump-like action that there is a close relation between the axial inflow and the radial out-flow. This flow phenomena is referred to von Kármán's viscous pump (Owen and Rogers, 1989; Andersson et al., 2001).

The quantity of fluid, Q, which is pumped outward is calculated as follows for one side of a disk of radius R,

$$Q = 2\pi R \int_0^\infty v_r \, dz \tag{4.14}$$

Keeping in mind that $v_r = \Omega \, r \, F(\zeta)$, and using the continuity equation (3.30), equation (4.14) becomes:

$$Q = 2\pi R \int_0^\infty \Omega r F \frac{dz}{d\zeta} d\zeta \tag{4.15}$$

$$Q = 2\pi R \int_0^\infty \Omega r \left(-\frac{H'}{2} \right) \left(\frac{\kappa}{\Omega} \right)^{\frac{1}{2}} d\zeta \tag{4.16}$$

$$Q = -\pi R^2 (\Omega \kappa)^{\frac{1}{2}} H(\infty) \tag{4.17}$$

Using the same definition of Reynolds number as before

$$Q = -\pi \Omega R^3 \, \mathrm{Re}_\phi^{-1/2} H(\infty) \tag{4.18}$$

or

$$Q = -2\pi^2 N R^3 \, \mathrm{Re}_\phi^{-1/2} H(\infty) \,, \tag{4.19}$$

where N is the rotational speed in radians per second. In dimensionless form, this can be written as

$$\overline{Q} = \frac{Q}{N R^3} = -2\pi^2 \, \mathrm{Re}_\phi^{-1/2} H(\infty) \tag{4.20}$$

The delivery coefficient, $\overline{Q}$, is a useful parameter for comparing different pumps (Lutz et al., 1996). In this case, it is used to show how the yield stress can affect the volumetric flow rate of the pump. Increasing B_y decreases $H(\infty)$, which causes a lower volumetric flow rate as shown in Fig. 4.11. This result demonstrates the practical significance of an accurate determination of $H(\infty)$, and its effect on the volumetric flow rate. $H(\infty)$ is a function of Bingham number and is tabulated in Table C.2, Appendix C.

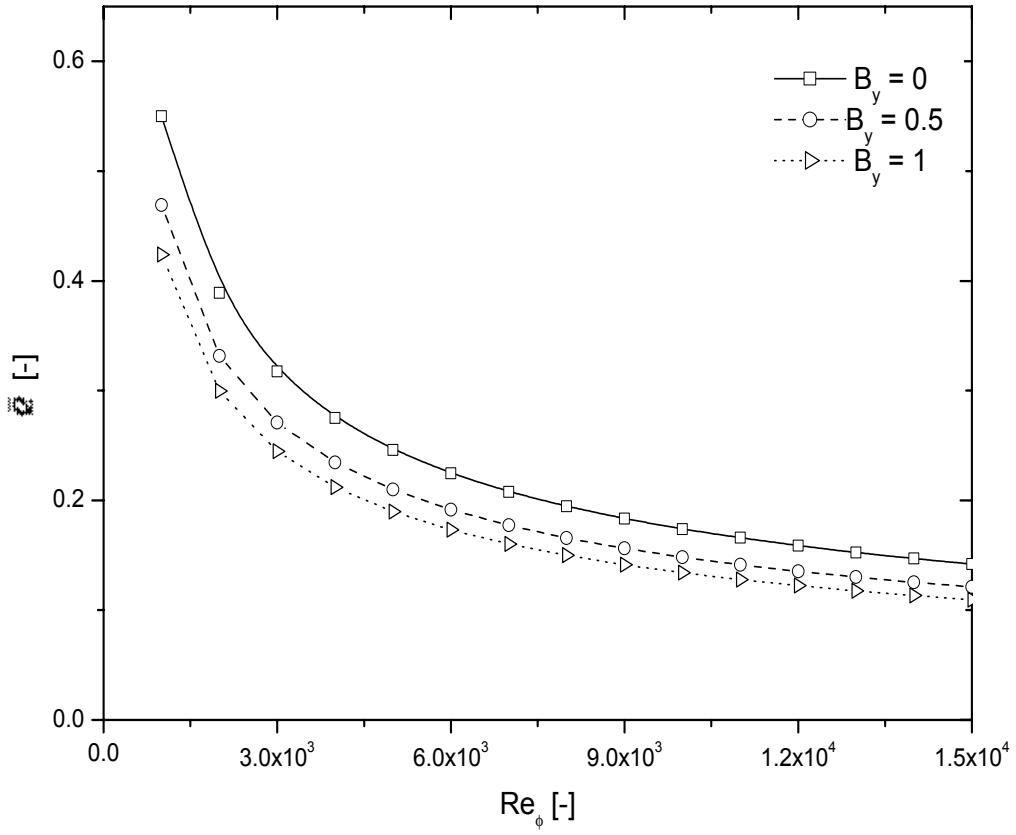

Figure 4.11: Variation of the delivery coefficient with Reynolds number for different values of B_y

4.6 Summary

The numerical solution of the resultant ODEs represents a three-dimensional flow field in the vicinity of the rotating disk. The numerical predictions compare well with the published results of Ostrach and Thornton (1956) and Schlichting (1979), for a Newtonian fluid and Andersson et al. (2001) for a power-law fluid. The Bingham number has a significant effect on the flow behavior. It decreases the magnitude of the radial and

axial velocity components, and increases the magnitude of the tangential velocity component. An accompanying increase of the boundary layer thickness adjacent to the disk is observed. Moreover, the wall shear stress in the tangential direction increases monotonically with increasing B_y, thereby increasing the torque required to maintain rotation of the disk at the prescribed rotational speed. On the other hand, the volumetric flow rate, Q, is reduced with increasing B_y.

CHAPTER 5

Rheological and Wax Appearance Temperature Experiments

5.1 Introduction

In this part of the thesis, the goal was to produce a transparent oil that rheologically simulates the Amna waxy crude oil. This involved conducting rheological measurements of different fluid mixtures. Once the waxy oil was simulated, the intention was to use it for the flow visualization experiments and the PIV measurements to be described in Chapters 6 and 7 respectively. However, preliminary measurements showed that the oil mixtures were not entirely transparent and therefore could not be used for PIV measurements. Instead, they were used only to visualize the flow over a rotating disk (Chapter 6) where a lesser degree of visibility is acceptable. The transparency requirement added an additional research component that was to produce a Bingham fluid that was sufficiently transparent so that it could be used for PIV measurements. A diluted hair gel was found to both exhibit Bingham behavior and was acceptable for PIV measurements. However, it exhibited higher plastic viscosities and yield stresses compared to the waxy oils.

In this chapter, Section 5.2 presents the materials that were used to produce the waxy oil and the gel solution. Section 5.3 describes the preparation of the waxy oils and the gel solutions. Sections 5.4 and 5.5 present the viscometer and the experimental procedure, respectively. Section 5.6 presents the rheological characterisation of both the waxy oils and the gel solutions. A summary of the rheological experiments are presented in Section 5.7.

5.2 Materials

For a fluid to properly simulate a waxy crude and be appropriate for visualization experiments it must be: (i) a fluid that exhibits a yield stress; (ii) transparent and (iii) chemically stable. After an extensive investigation, a mixture of paraffin waxes in white mineral oil was found to adequately simulate waxy crude oils. The mineral oil employed in this study was commercial oil, manufactured for the pharmaceutical industry by Rougier Pharma, Mirabel, QC, Canada. Its physical properties are listed in Table 5.1. The paraffin wax was manufactured by Salathe Oil Co. / Stevenson-Cooper Inc. Philadelphia, USA. Its physical properties are listed in Table 5.2. The level of contaminants in the mineral oil and the wax was less then 1 wt%. Observations show that all the samples of wax/oil mixtures have a foggy appearance, which increased with wax concentration. However, the degree of transparency was sufficient to visualize the flow patterns when dye was added and the mixture was sheared with a disk.

Since transparency of the mixture is essential for the PIV measurements, several substitutes were investigated with respect to their fluid properties. For the model

experiments, a hair gel was chosen because it satisfied the transparency requirement under the conditions of the model experiments and it exhibited Bingham fluid behaviour. The fluid appeared to exhibit a yield stress based on two observations. The substance does not return to a plane surface if the free surface is disturbed and air bubbles within the fluid do not rise to the surface.

Table 5.1: Properties of the mineral oil (based on Manufacturer's MSDS)

Density at 15.6 $^{\circ}$C, kg/m^3	845-855
Boiling point, $^{\circ}$C	343
Flash point, $^{\circ}$C	188
Pour point, $^{\circ}$C	-9
Color	Clear
Water solubility	Insoluble
Hydrocarbon solubility	Soluble
Viscosity at 25 $^{\circ}$C, cP	18

Table 5.2: Properties of the paraffin wax (based on Manufacturer's MSDS)

Density at 15.6 °C, kg/m^3	810
Boiling point, °C	343
Flash point, °C	213
Pour point, °C	NA
Color	White
Water solubility	Negligible
Hydrocarbon solubility	Soluble
Viscosity at 25 °C, cP	NA

5.3 Preparation of Experimental Fluids

5.3.1 Synthetic Waxy Oils

The following procedure was employed to prepare the mixture:

1. The paraffin wax was melted in a beaker at 63°C. The beaker was immersed in a heated water bath. The temperature was maintained at 10 degrees above the wax melting point (53°C), for 1 h. This pre-treatment was carried out to remove any thermal history effects.
2. The mineral oil was then slowly mixed with the melted wax under continuous stirring conditions until a pre-specified concentration was attained. Additions of

mineral oil to the paraffin wax were made on the basis of percentage by weight of paraffin in the mixture. For this work, concentrations of 3, 4 5, 7, 10, 15 and 20 wt% of wax in the mineral oil were selected. The choice of these concentrations was guided by preliminary experiments and by published data on the wax content in many of the waxy crude oils that exist in the world (Hydrocarbon Management, 2004).

3. Two batches at each of the concentrations were prepared, stored in 8 oz jars (225 g), and kept in the water bath at 63°C until the time of measurement.
4. The mixtures were cooled from 63°C to the desired temperature at a rate of 10 °C /h. This rate of cooling was necessary in order to avoid time dependency, thixotropic behavior due to the crystallization of the wax (Wardaugh and Boger, 1987).

A compromise between the transparency and the desired properties of the fluid was taken into account in creating the waxy oil mixture. A series of rheological measurements of different waxy mixtures was performed to determine which concentration matched the rheological properties of the Amna waxy crude oil from Libya and at the same time met the transparency requirements. A mixture of 93 wt% mineral oil and 7 wt% paraffin wax was found to meet these requirements. The rheological properties of the Amna waxy crude oil are presented in Table 5.3. This table was prepared using information from Barry (1970) and Seitzer and Lovell (1981). However, experiments show that this oil can not be used for the PIV measurements because the

clarity of the fluid is not suitable. Instead, it can be used for flow visualization where a lesser degree of visibility is acceptable.

Table 5.3: Properties of the Libyan Amna waxy crude oil

Density, kg/m^3	846		
Pour point, $^{\circ}C$	24		
Wax content, wt%	10-20		
Viscosity, cP (mPa.s)	Temperature, $^{\circ}C$	Yield stress, N/m^2 (Pascal)	Temperature, $^{\circ}C$
10	50	0.375	25
12.1	40	-	24
18	27	1	21.1
20	25	2	19
30.7	21.1	40	15.6
50	15	-	-

5.3.2 Gel solutions

In producing the hair gel solution, air bubbles became trapped within the fluid due the yield stress exhibited by the fluid. The presence of air bubbles compromises the transparency of the material because a laser light sheet will scatter significantly when it encounters the bubbles and thus would not penetrate the hair gel mixture adequately. The appearance of these bubbles gives the fluid a misty appearance similar to that experienced in the waxy oils. Several methods of removing the bubbles from the gel were investigated. These included:

1. Placing the gel in a high vacuum of 5 kPa absolute pressure for an extended period of time. This method was not successful since it caused the gel to boil and foam.
2. Placing the gel in a high pressure chamber for an extended period of time. This method was successful in releasing the bubbles to the air; however, it also changed the color of the gel.
3. Finally, centrifuging the gel removed the bubbles, making the gel more transparent.

Since the gel is water soluble, dilution with water was used to reduce the yield stress of the gel. The gel was diluted with specific amounts of water (12.5, 25 and 50 wt %). This permitted tests to be performed with yield stress values varying between 0.4 and 28 times the yield stress of the waxy crude oil.

5.4 Cone and Plate Viscometer

Of the viscometers available, the cone and plate viscometer represents the most desirable viscometer geometry for this investigation because it resembles the rotating disk in that the shear increases from zero at the axis to a maximum value at the tip of the cone. Another significant advantage of the cone and plate viscometer is that it requires only a small sample volume, which simplifies temperature control.

The rheological properties of the oil mixtures and the gel solutions were measured using a cone and plate viscometer manufactured by Brookfield Engineering Laboratories

Inc, Stoughton, MA, U.S.A. as shown in Fig. 5.1. The viscometer is connected, through the ports on the sample plate, to a circulating temperature bath which controlled the temperature to within +/- 0.1 °C.

The principle of the cone and plate viscometer shown in Fig. 5.1 involves the rotation of a cone upon a plane surface at selected rotational speeds (shear rates). A torque measuring device connects the driving mechanism to a vertical axel from which the cone is suspended. The small sample of fluid between the cone and plate resists the rotation of the cone and the torque that develops is related to the shear stress experienced by the fluid. Knowing the geometric constants of the cone, and measuring the rate of rotation and the torque, one can determine the shear stress and the shear rate in the liquid.

For a cone and plate geometry (Fig. 5.2), with the conical spindle properly positioned, the shear stress and shear rate relationships are calculated from the measured torque and cone rotational speed by

$$\tau = \frac{M}{\frac{2}{3}\pi R^3} \tag{5.1}$$

$$\dot{\gamma} = \frac{2\pi\ \Omega}{\tan\theta} \tag{5.2}$$

where: τ = shear stress

$\dot{\gamma}$ = shear rate

M = torque

R = cone radius

Ω = cone speed

θ = cone angle

The type of plate and spindle employed was determined by the viscosity of the sample. Since the torque of the mixtures ranged widely for different test conditions, two different cones (CP-40 with 0.8 º cone angle, and CP-42 with 1.565 º cone angle) were used with a low torque viscometer (LVTDVCP-II). The CP-40 and the CP-42 spindles require 0.5 ml and 1.0 ml of sample, respectively. The gap between the cone and the plate must be adjusted to a specific value before measurements are performed. This is done by moving the plate up towards the cone until pins on the cone and plate come into contact and then the plate is lowered by 0.0005 inches (0.013mm).

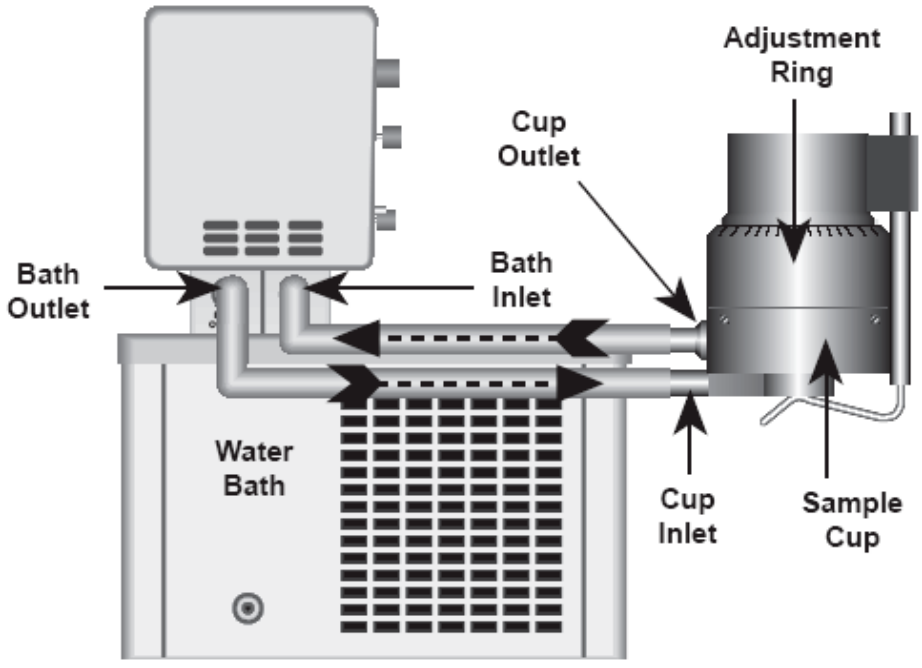

Figure 5.1: Cone and plate viscometer (Brookfield Cone/Plate Viscometer manual)

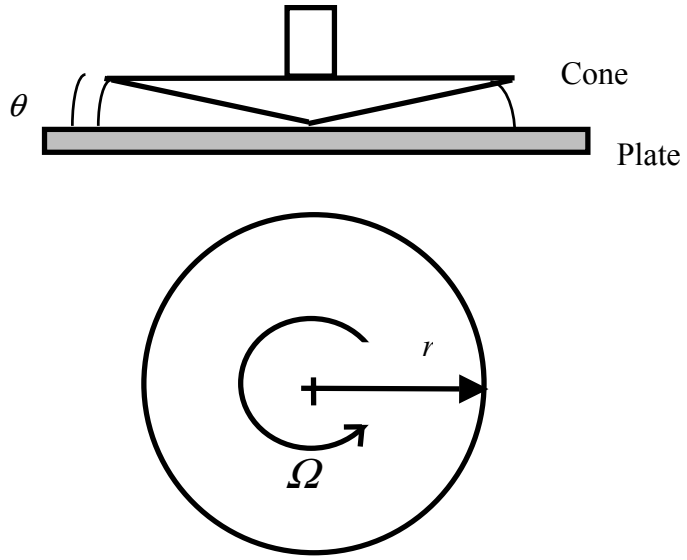

Figure 5.2: Cone and plate geometry

5.5 Experimental Technique

Viscosity measurements were made under controlled conditions. Below are the steps that were followed in conducting the measurements:

1. Prior to testing, the water bath was turned on and the temperature was adjusted to the desired temperature.
2. The plate was detached from the viscometer
3. The required sample volume was transferred to the center of the plate using a plastic syringe.
4. The plate was reattached to the viscometer and secured with the clip

5. The viscometer was suspended in a constant temperature water bath at the desired temperature for 30 minutes to bring the sample to thermal equilibrium.
6. The viscometer was started and the rotational speed was adjusted to give a torque higher than 10% but lower than 100% of the full scale to be in the viscosity range (Table 5.4).
7. The viscometer was run for 1 minute or until the torque did not drift more than 1%, then a measurement was taken.
8. For each determination, the following information was recorded:
    - apparent viscosity in mPa.s (cP)
    - spindle speed
    - temperature of sample to nearest 0.1°C
9. Following the measurement, either the sample was tested at another temperature or the plate was removed from the viscometer. If the plate was removed, it was cleaned using the steps described in the procedure below, prior to the measurement of a different sample.

5.5.1 Viscometer Quality Control Procedure

To ensure the instrument operated at its highest precision and accuracy the following quality control procedures were conducted. Whenever the plate was removed from the viscometer, the sample was discarded and the plate was cleaned thoroughly according to the following procedure:

1. The plate was soaked in toluene to wash off the remaining wax.
2. It was then washed with a detergent soap solution to remove oil residue.

3. The plate was then rinsed with water..
4. Then, it was wiped with a soft cloth.
5. Finally, it was wiped with an acetone-soaked cloth. This procedure was done between each trial.

5.5.2 Viscometer Calibration Procedure

The viscometer was calibrated according to manufacturer's instructions, using two viscosity standards (Brookfield Engineering Lab, Stoughton, MA). The standards were chosen within the viscosity range of the material being measured and the range of the viscometer. Therefore, a 10 cP at 25°C, standard silicone oil was chosen to account for the test material at high temperatures (10 cP at 40°C) and a 50 cP at 25°C, silicone oil was used to account for the test material at low temperature (50 cP at 15°C). Calibration of the viscometer was accomplished by a simple mechanical procedure. This procedure was performed every time the spindle was removed from the viscometer. This procedure was:

1. Turn on temperature bath and allow sufficient time for sample plate to reach the desired temperature. Ensure that the circulating bath used maintains the stated calibration temperature (25°C) to within ± 0.1ºC.
2. Set speed at 12 rpm with motor OFF.
3. Remove the sample plate and attach the cone to the viscometer.
4. Start the viscometer running at 12 rpm. Percent of full-scale spring torque readings were utilized for setting the cone/plate gap. If the display reading jumped to 0.3 of scale (or higher), or did not settle to zero (indicating that the

cone and plate are hitting), unscrew the adjustment ring by turning it to the left (clockwise as you look down on the instrument) until the reading settles at 0.0.

5. Turn the adjustment ring to the right in small increments while watching the viscometer display. Remember that you are trying to raise the plate so that the pin on the cone touches the pin on the plate. Once you have found this contact point, you can turn the ring counter clockwise to create the desired gap between cone and plate. Turn the adjustment ring until the display reading jumps from 0.0 to 0.3. This is the CONTACT POINT. The plate may have to be adjusted up and down several times before this torque deflection is satisfactorily reached.
6. When you are satisfied that the pins of the cone and plate are just making contact, make a pencil mark on the adjustment ring directly under the index mark on the pivot housing.
7. Turn the adjustment ring to the left one division from the pencil mark you have just made. This will separate the pins by 0.013 mm. This is a very important step because if it is not done, the cone and plate may touch constantly and the instrument will make inaccurate measurements. The viscometer is now mechanically set and ready for sample measurement.
8. Put the proper amount of viscosity standard fluid into the sample plate (0.5 ml for the CP-40 spindle and 1.0 ml for the CP-42).
9. Attach sample plate to viscometer and allow approximately 15 minutes for temperature equilibrium.
10. Measure the viscosity of the fluid and record the viscometer readings in cP.

Table 5.4: Full scale viscosity ranges (Brookfield Cone/Plate Viscometer Manual)

1.565° CONE SPINDLE			
Speed (RPM)	Shear Rate (sec^{-1})	Cone #CP-42 1 ml Sample	Cone #CP-51 0.5 ml Sample
60.0	230.00	10.00	80.90
30.0	115.00	20.00	161.80
12.0	46.00	50.00	404.50
6.0	23.00	100.00	809.00
3.0	11.50	200.00	1,618.00
1.5	5.75	400.00	3,236.00
0.6	2.30	1,000.00	8,090.00
0.3	1.15	2,000.00	16,180.00
0.8° CONE SPINDLE			
Speed (RPM)	Shear Rate (sec^{-1})	Cone #CP-40 0.5 ml Sample	
60.0	450.00	5.14	
30.0	225.00	10.28	
12.0	90.00	25.70	
6.0	45.00	51.40	
3.0	22.50	102.80	
1.5	11.25	205.60	
0.6	4.50	514.00	
0.3	2.25	1,028.00	

5.5.3 Accuracy for the Calibration Check

The total error is a combined error of the standard fluid and the viscometer. The instrument accuracy is 1% of Full Scale Range (the maximum viscometer range at each shear rate) in use and the standard fluid is accurate to 1% of the actual viscosity value written on the jar in cP. Using a digital cone and plate viscometer LDVCP with a CP-40 spindle rotating at 12 rpm and a Brookfield standard fluid of 10 cp with the actual viscosity of 9.7 cP at 25°C, yielded a measurement of 9.9 cP. Therefore, the allowable

range was 9.7 ± 0.354 cP. A measurement of 9.9 was within this range means the operation of the viscometer was verified. The same procedure was followed for the CP-42 spindle rotating at 6 rpm and a Brookfield standard of 50 cP with the actual viscosity of 48 cP at 25°C, and was found that the measurements within the allowable range. Figure 5.3 (a, b) shows the results of Newtonian fluids dynamic viscosity measurements. From the figure, the accuracy (as compared to the standard fluid) is better than $\pm$ 1% and the reproducibility is also better than $\pm$ 1%. A summary of the calibration data was given in Table 5.5.

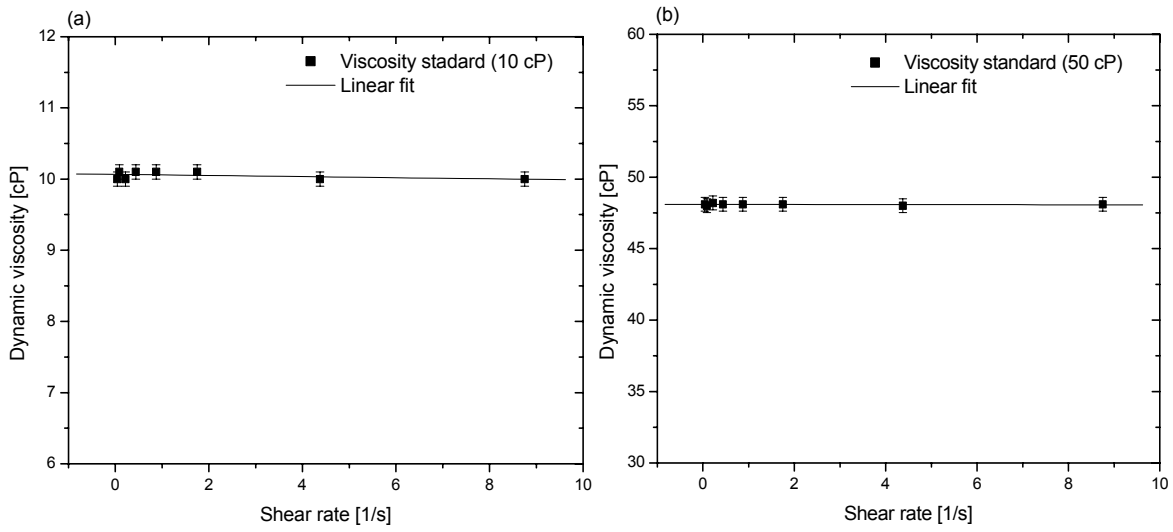

Figure 5.3: Viscosity measurements for Brookfield standards at 25°C: (a) 10 cP silicone oil; (b) 50 cP silicone oil

Table 5.5: Summary of the calibration data

Sample silicone oil	Speed (rpm)	Measured viscosity (cP)	Nominal value (cP)	Actual value (cP)	Deviation from actual Value (cP)	Accuracy Allowance by Brookfield (cP)	Total errors	Range Allowance
10 cP	12	9.9	10	9.7	0.097	0.257	0.354	9.7 ± 0.354
50 cP	6	48.1	50	48	0.48	0.514	0.994	48 ± 0.994

5.6 Rheological Characterization

5.6.1 Synthetic Waxy Oils

The prepared mixture samples were characterized at a wide range of temperatures (from 15 to 40°C), employing the rotational viscometer at speeds of 0.3, 0.6, 1.5, 3, 6, 12, 30 and 60 rpm. These speeds correspond to shear rates of 2.25, 4.5, 11.25, 22.5, 45, 90, 225 and 450 s^{-1}. In order to get stabilized readings, measurements were made every 30 s for a total of 30 min at each shear rate. Isothermal conditions were maintained during measurements using the circulating water bath. All of the rheological measurements were conducted on duplicate samples (a sample from each batch), and the whole process including sample preparation was repeated twice. In order to check the reproducibility of the experiment, one of the runs was chosen at random and repeated twice. The reproducibility was observed to within ± 2%.

Measurements were repeated 60 times to arrive at an acceptable estimate of the average value, and, more importantly, to observe the scatter in the results. This allows an

assessment of the uncertainty in the measurements. The total uncertainty is given by (Stern, 1999):

$$U_v = \sqrt{B_v^{\,2} + P_v^{\,2}} \tag{5.3}$$

The Bias error, B_v, is a systematic error which is constant for the duration of the measurement and is estimated by non-statistical methods. According to the viscometer manufacturer and the calibration tests the viscometer was accurate to within ±1.0% of the working range. The precision error, P_v, is caused by lack of repeatability in measurement. It is given by:

$$P_v = \frac{a_c\ S}{\sqrt{N}}, \tag{5.4}$$

where a_c =1.96 for 95% confidence interval and S is the standard deviation. The range of the standard deviation of the measurements (0.08-0.1%) estimated the precision error to fall within the ±0.2% reproducibility claimed by the viscometer manufacturer. Therefore, in all of the viscosity measurements, the error bars on the graphs are 3.0% of the range of viscosity at each shear rate.

5.6.1.1 Effect of Wax Concentration on the Shear Stress-Shear Rate Curve

The viscometric tests were performed on all of the mixtures (3, 4, 5, 7, 10, 15, and 20 wt% waxes) as well as the wax free oil. However, for some mixtures viscosity measurements could not be obtained, because the torque range was higher than the capability of the viscometer. The mixtures with concentrations of 3, 4, 5, 7 and 10 wt% are those for which the viscometer measurements were valid. Rheological measurements were performed for the different concentrations at room temperature (25°C) and are

shown in Fig. 5.4. It is clearly seen that the influence of wax concentration on the mineral oil rheology was significant since various ranges of wax concentration can lead to different types of flow curves. Linear fits of the experimental data show that at concentrations below 4 wt%, including wax-free oil, the fluids exhibit Newtonian behaviour (Figs. 5.4. a, b). Clearly, the oil rheological behaviour was transformed from Newtonian behaviour to that of a Bingham plastic, when the wax concentration was increased above 3 wt%. Thus, the shear rate appears to be linearly proportional to the shear stress with a reasonable correlation factor, R^2, for all the wax concentrations.

5.6.1.2 Effect of Wax Concentration on the Bingham Yield Stress and Bingham Plastic Viscosity

Extrapolation of the linear section to its intersection with the shear stress axis gives the yield value of the ideal Bingham plastic, i.e. due to the limited capability of the viscometer to perform measurements at low values of shear rate, experimental data in relatively a higher range of shear rate (> 5 s^{-1}) was extended using a trendline. The 3 wt% sample (Fig. 5.4.b) did not appear to have yield stress, which is due to the relatively low wax concentration, compared to the other samples (Fig. 5.4. c, d, e, f). The extrapolated Bingham yield stress values for the oil samples as a function of wax concentration were plotted in Fig. 5.5. The extrapolated yield stress increases rather sharply in a non-linear form with increasing wax concentration when the wax concentration is larger than 3 wt%. It varied from 0.087 Pa at 4 wt% to 0.7 Pa at 10 wt%.

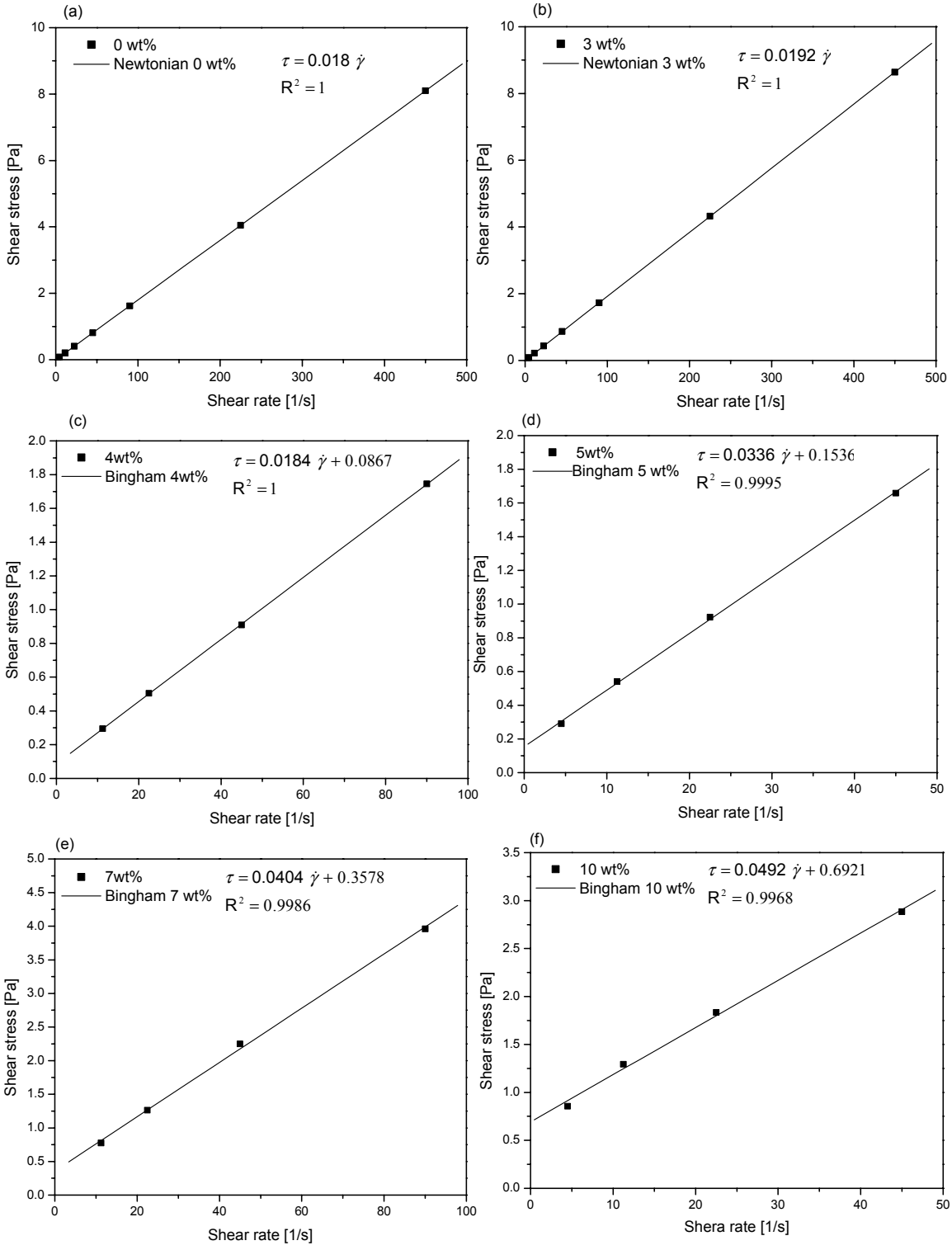

Figure 5.4: Shear stress-shear rate curve for the oil/ wax mixtures at 25°C, (a) 0 wt%; (b) 3 wt%; (c) 4 wt%; (d) 5 wt%; (e) 7 wt%; (f) 10 wt%

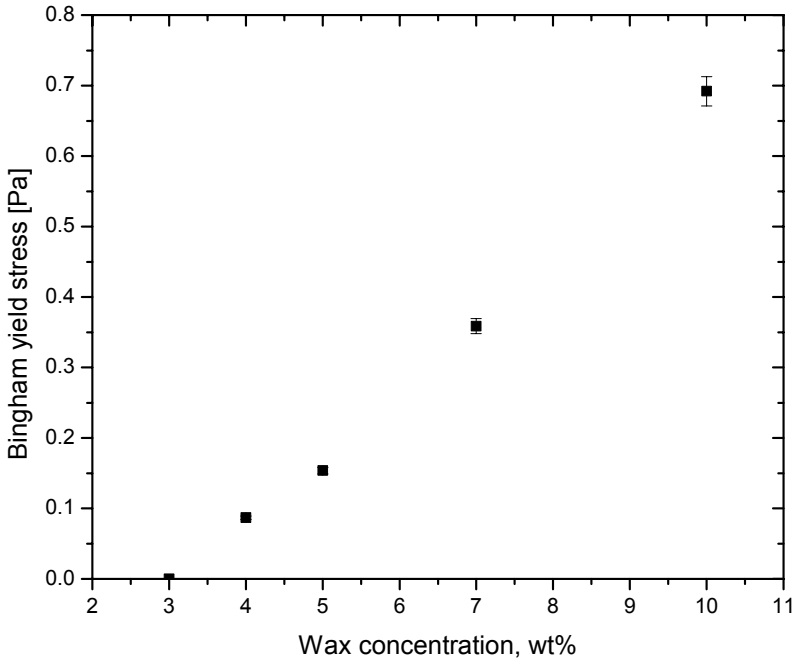

Figure 5.5: Bingham yield stress versus wax concentration at 25°C

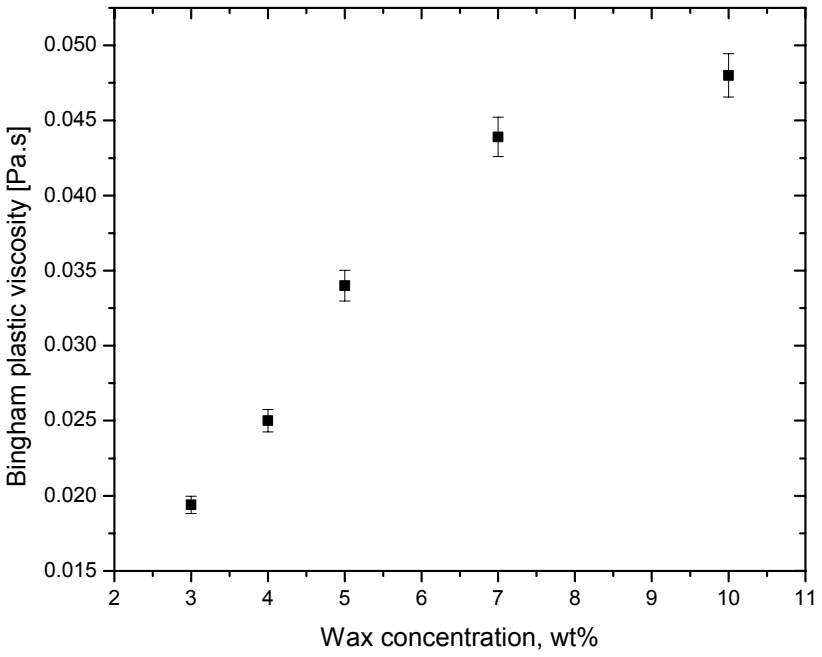

Figure 5.6: Bingham plastic viscosity versus wax concentration at 25°C

The Bingham plastic viscosity was found to increase with increasing wax concentrations as shown in Fig. 5.6. From this figure, an inverse proportion was noted between the increase in the Bingham plastic viscosity and wax concentrations.

It can be concluded from Figs. 5.4-5.6 and Table 5.3 that a 7 wt% mixture resembles the rheological properties of the Amna waxy crude oil.

5.6.1.3 Effect of Temperature on the Wax-Oil Mixture

Rheological measurements with the 7 wt% mixture were performed at different temperatures, from 19.7°C to 40°C. These temperatures were chosen in accordance with the documented properties of the Amna waxy crude oil. The shear stress developed in the sample as a function of increasing shear rate was plotted in Fig.5.7. As indicated in Figs. 5.7 a, b, c and d, at low temperatures (i.e., 19.7°C to 25°C), the change in temperature does not change the rheological behaviour that the oil exhibits (i.e., Bingham fluid). However, both the Bingham extrapolated yield stress and the Bingham plastic viscosity of the oil decrease with increasing temperature. This non-Newtonian behaviour results from the ability of the precipitated waxes to crystallize. Once these crystals have formed, they show a strong tendency to aggregate (Lorenzo, 2003).

At the intermediate and high temperatures (30°C to 40°C), the curves shown in Figures (e) and (f) are straight lines passing through the origin. This suggests that high temperatures increase the solubility of the wax in the oil, resulting in Newtonian behaviour.

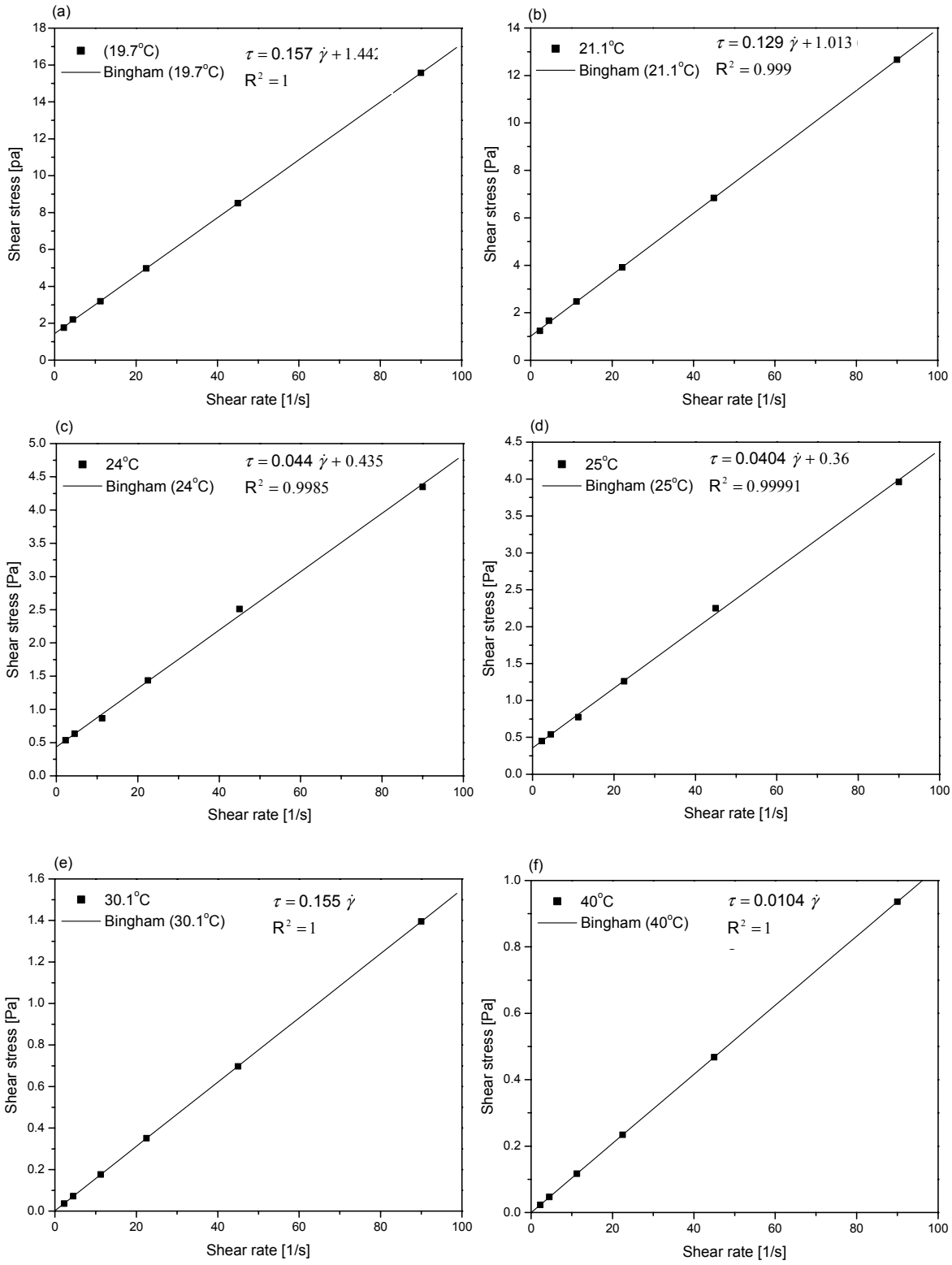

Figure 5.7: Shear stress-shear rate curve for the waxy oil simulant (7 wt%) at different temperatures, (a): 19.7°C; (b) : 21.1°C; (c): 24°C; (d): 25°C; (e): 30.1°C; (f): 40°C

The effects of temperature on the Bingham plastic viscosity, μ_p, and Bingham yield stress, τ_y, of the Amna crude simulant are shown, respectively, in Figs. 5.8 and 5.9. It is clear from Fig. 5.8 that the value of the Bingham plastic viscosity increases sharply as the temperature decreases. Also, from Fig. 5.9, as the temperature increases the Bingham yield stress decreases. At 30°C, the oil behaves as Newtonian fluid, i.e. the value of yield stress is equal to zero. At temperatures up to 25°C the mixture simulating Amna crude follows the non-Newtonian behaviour with a yield stress.

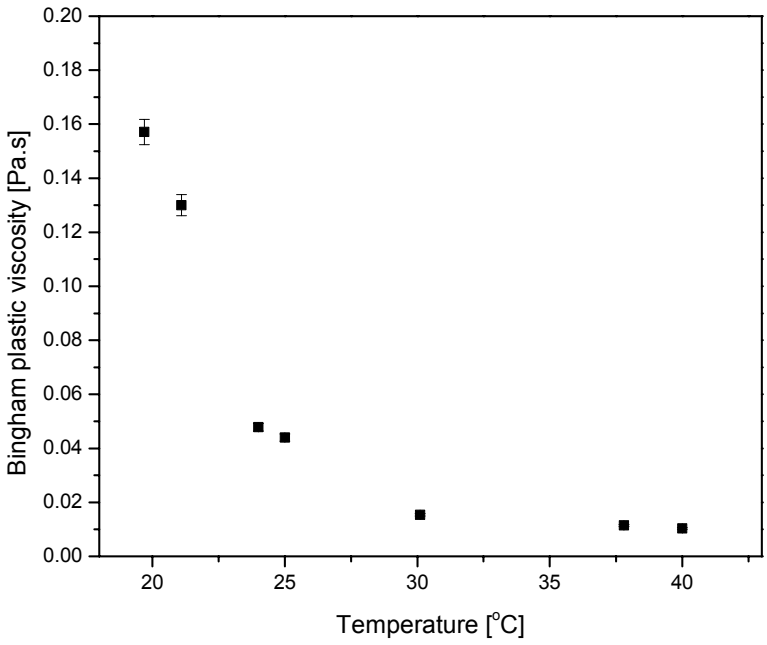

Figure 5.8: Bingham plastic viscosity versus temperature for the Amna crude oil simulant (7 wt%)

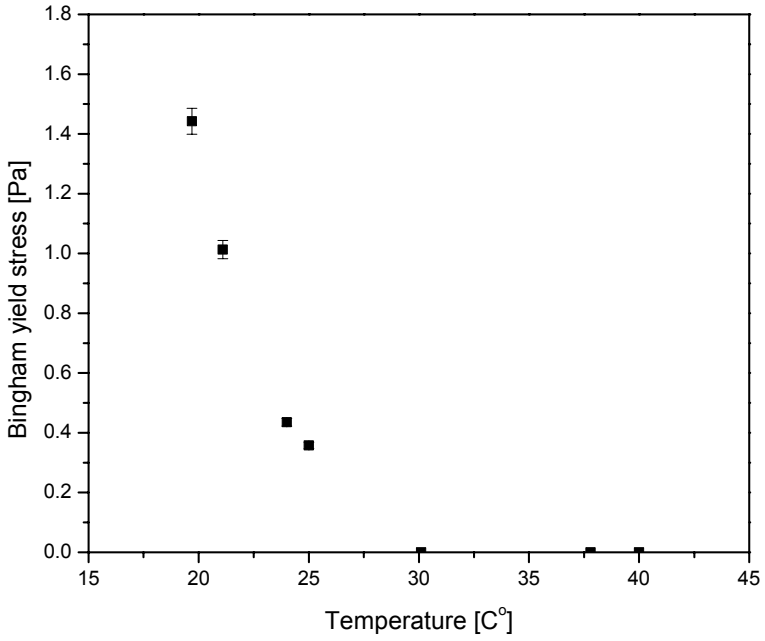

Figure 5.9: Bingham yield stress versus temperature for the Amna crude oil simulant (7 wt%)

5.6.1.4 Wax Appearance Temperature

To obtain an estimate of the pour point, the wax appearance temperature (WAT) approach developed by Khan et al. (1993) was adopted instead of the standard ASTM D-97 procedure. This takes advantage of the ability to judge mixture transparency. The temperature at which cloudiness first occurred was recorded as the wax appearance temperature. All waxy oil samples show increased WAT with increasing wax concentration, sharply at first and then less rapidly, as shown in Fig. 5.10. It is also shown in Fig. 5.10 that the WAT of the 7 wt% mixture was 24°C, which matches the pour point of the Amna oil.

Khan et al. (1993) have demonstrated that the technique was accurate to ± 0.5°C, and the reproducibility of the results was ± 1°C. This accuracy was in agreement with our measurements.

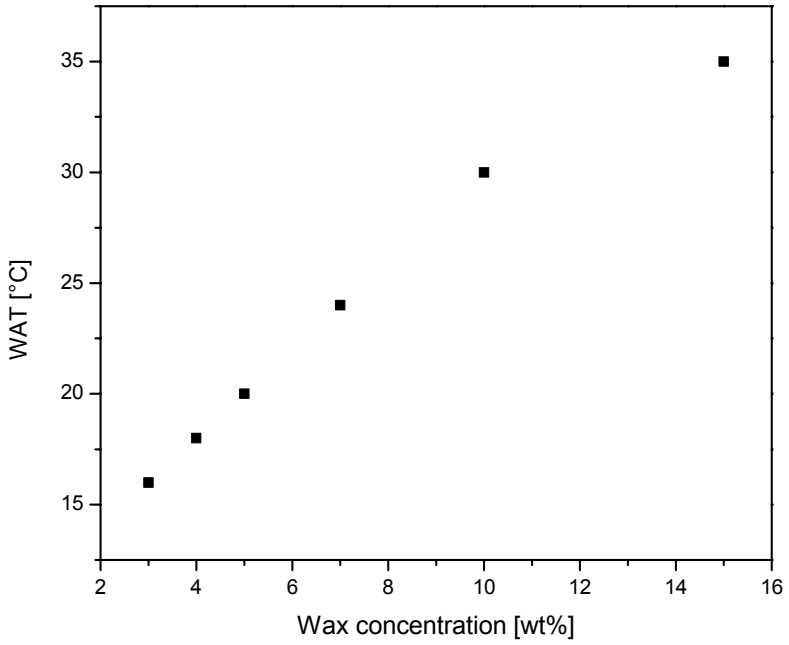

Figure 5.10: Wax Appearance Temperature of paraffin wax and mineral oil samples.

5.6.2 Gel Solutions

The physical properties of the different dilutions of gel with water were measured and plotted in Fig. 5.11. In all of the samples, the shear stress as a function of shear rate was displaced from the origin indicating that the gel solutions exhibit a yield stress. The Bingham yield stresses for all the samples can hence be obtained from the least squares

fitted lines by extrapolating the linear lines to the zero shear rates. The yield stress of gel mixtures increased markedly, by about 28 times, as the concentration of gel was raised from 25 wt% to 50 wt% (Fig. 5.11).

Viscosity measurements of the gel mixtures are more stable than those of the oil-wax mixture. Repeatability was estimated to be within 2% and the percent error of viscosity caused by variation in temperature was negligible. Because the error bars are the size of the symbols, they have not been plotted.

5.6.3 Suitability of the Bingham Model

The reliability of the experimental results presented in Figs 5.4, 5.7 and 5.11 was evaluated using regression analysis. By using this approach, trendlines of data were extended to include values at zero shear rates . Thus, the flow behaviour can be characterised by a slope (Bingham plastic viscosity) and intercept (Bingham yield stress). A trendline is most reliable when its coefficient, R^2, is at or near 1. The regression coefficients were calculated automatically by Origin 6.0 software and their values were displayed on the figures.

Based on the values of the regression coefficients, it can be observed that good agreement is achieved between the experimental data and the Bingham model for both the waxy oils and the gel solutions.

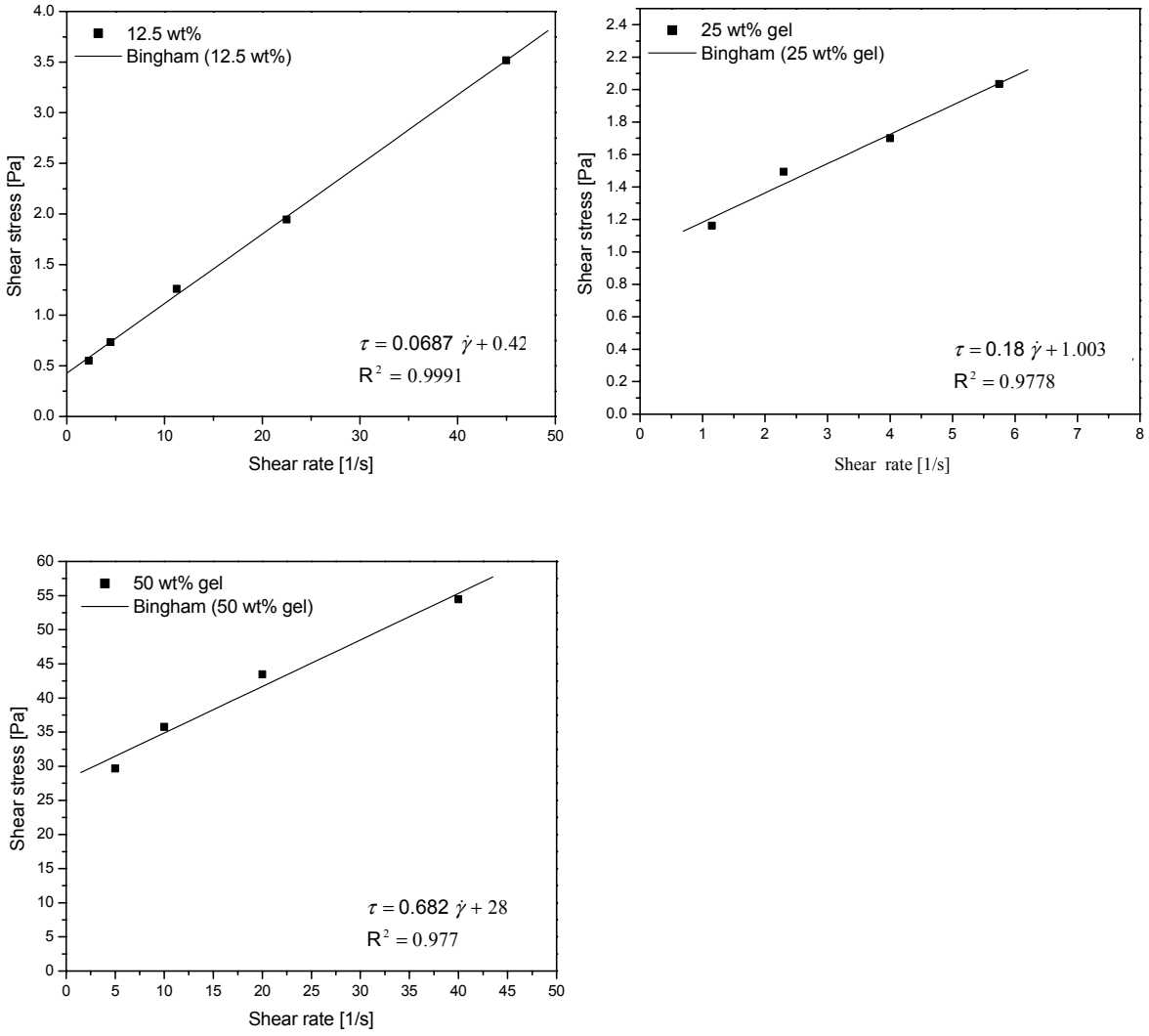

Figure 5.11: Shear stress-shear rate curve for the diluted gel mixtures for 12.5, 25, and 50 wt% gel concentrations, respectively.

5.7 Summary

Since waxy crude oils are naturally opaque, an experimental plan was undertaken to develop a transparent oil that is rheologically similar to the Amna waxy crude oil from Libya. A wide range of mineral oil-paraffinic wax mixtures were considered. Bingham plastic behavior was observed at wax concentrations higher than 3 wt% at a temperature of 25°C. An oil-wax mixture that simulated specific properties of Amna waxy crude oil was achieved at a wax concentration of 7 wt% at a temperature of 25°C. At this concentration, the rheological parameters (i.e., plastic viscosity and Bingham yield stress), and WAT (which approximates pour point) of the crude were simulated. The plastic viscosity and yield stress, including their dependence on temperature and shear rate, were documented for the flow visualization experiments (Chapter 6). A summary of these parameters for the Amna oil and oil-wax mixtures is given in Table 5.6.

To meet the requirements of the PIV system (Chapter 7), a higher degree of transparency was required. A second Bingham fluid was created and rheologically investigated. Despite its high yield stress, a solution which had a gel concentration of 50 wt% was found to be sufficiently transparent to perform the PIV measurements.

Table 5.6: Properties of the investigated waxy crude oil and the oil-wax mixtures

Property	**Sample**						
	Amna Oil		**3%**	**5%**	**7%**	**10%**	**15%**
Density, kg/m^3	846		-	-	880	-	-
Pour point, $^{\circ}$C	24		16	20	24	30	35
Wax content, wt%	10-20		3	5	7	10	15
Viscosity, cP	37.8 ^{o}C	11	10.6 †	10.8 †	11.5†	18.4†	-
(mPa.s)	25 ^{o}C	20	19.4 †	37 *	50*	64.1*	-
	21.1 ^{o}C	30.7	25.1 *	50*	152*	319*	-
Yield stress, N/m^2	25 ^{o}C	0.375	-	0.15	0.36	0.7	-
(Pascal)	21.1 ^{o}C	1	0.03	0.25	1.01	2.4	-

*Data recorded at 6rpm
† Newtonian

CHAPTER 6

Flow Visualization

6.1 Introduction

Rotating a solid body (disk, impeller or turbine) in a Newtonian fluid generates two effects. The first effect, which produces shear in the fluid, occurs in close proximity to the disk. The second effect of disk rotation is the generation of a circulation pattern that exchanges the fluid in the intensively rotated region near the disk with the fluid in the remainder of the tank. These two effects are the essence of designing mixing equipment, where a good balance between these two functions is required to achieve economical operation for a low-viscosity Newtonian fluid (Wichterle and Wein, 1981).

The situation changes when standard mixing equipment is used for mixing non-Newtonian fluids. Wichterle and Wein (1981) compared the flow of a non-Newtonian pseudoplastic fluid with that of a Newtonian fluid with a viscosity approximating the range of apparent viscosities of the pseudoplastic fluid. They noted that the flow in the region of higher shear forces near the agitator is enhanced, while the slow recirculating flow is suppressed by the higher non-Newtonian apparent viscosities near the walls. In a Newtonian fluid, reducing the speed of the agitator is accompanied by a reduction of both

mixing effects. In a pseudoplastic fluid, reducing the agitator speed causes a nearly step-wise change in the quality of the mixing at the point where the circulation no longer reaches the wall which produces a stagnation region.

A similar effect is observed with fluids which exhibit a yield stress. This effect can be detected by observing the formation of the so-called yield surface (Solomon et al., 1981), i.e., the interface between the fluid in motion and the fluid at rest. The shear stress decreases with distance from the disk. The fluid in the tank will be sheared in the region of the tank where the applied stress exceeds the yield stress. However, if the stress acting on the fluid is less than the yield stress, then there will be a region that is not sheared and which will stay stagnant. The flow pattern exhibits a recirculating zone separated from the walls by a region of stagnant fluid. The recirculating zone is to be considered in this study. In this section, the nature of this phenomenon will be described. A qualitative discussion of the development of the flow patterns around the rotating disk as the Bingham number changes will be presented.

6.2 The Rotating Disk Apparatus

To assess the behavior of non-Newtonian fluids under shear, a special rotating disk device was required. A rotating-disk apparatus, which is normally used for studying electrochemical kinetics, was adapted for this study. The disk apparatus, shown in Fig. 6.1, consists of a disk on the end of a shaft that is mounted up to a Pine Instrument Company Model AFPIR analytical rotator.

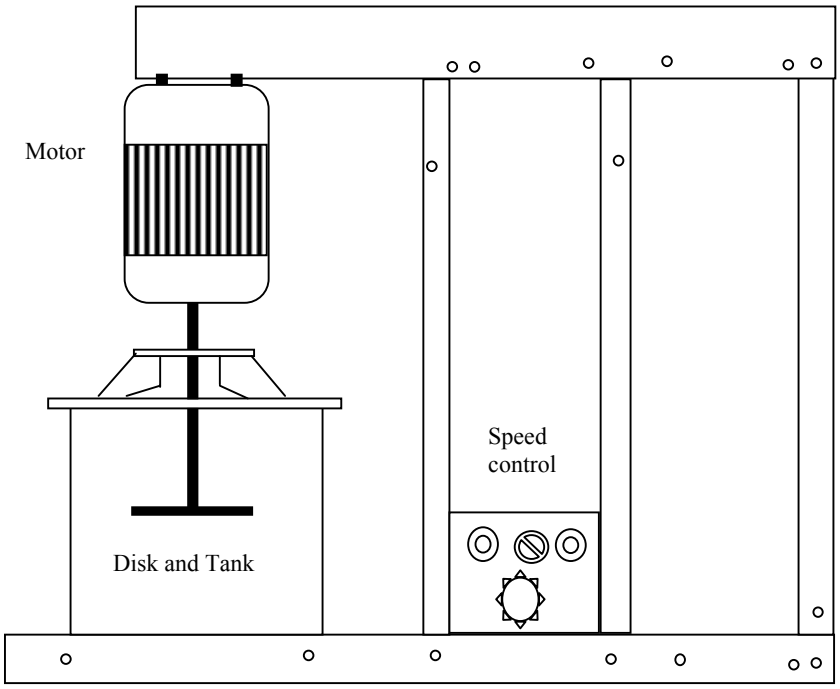

Figure 6.1: Experimental arrangement for flow visualization measurements

This instrument has a variable speed motor drive, which allows it to be driven at a constant speed in the range 0-10,000 rpm. The rotation direction is clockwise. The disk is 34.6 mm in diameter and 1 mm in thickness. It was fabricated from aluminum as a single unit with a 6 mm shaft to ensure satisfactory alignment. To avoid reflection of light, the cylindrical shaft and disk were painted flat black. The disk is immersed to a depth of 25 mm near the center of a 183 mm x 183 mm x 150 mm transparent box open at the top. Hansford and Litt (1968) demonstrated that a tank of these dimension was suitable for a disk of this size rotating in water and their results indicated that there were no wall effects. The rotation rate and fluid properties define the extent of the recirculating zone which then sets the limits of the flow.

6.3 Equipment and Fluids

In this work, the flow visualization equipment included a digital camera (Nikon D70) and an image analysis system. The digital camera was used to observe the flow around the disk. The camera has a high magnification and a large depth of field. This allows the flow patterns throughout the tank to be clearly observed. In the experiment, the working distance between the camera lens and the centerline of the disk was 700 mm. Illumination was applied by placing the disk and the tank facility on a light table where the light was placed over top of the field of view. For successful flow visualization, the light intensity should be evenly distributed throughout the tank.

The observed results were recorded and stored in the memory of the camera, and subsequently processed by the image analysis system. The image analysis software that was used was a Corel Draw^{TM}. The image quality was improved using this image analysis system permitting quantitative conclusions to be drawn.

The Bingham fluid used in the experiment was the paraffin wax-mineral oil mixture (7 wt% wax) which modeled a waxy crude oil. The rheology of the fluid was described in Chapter 5. Two fluid mixtures of the same rheology were prepared; one was kept as a clear solution and one was dyed with an oil-soluble dye powder. Based on yield stress and plastic viscosity measurements, the presence of the dye did not have any effect upon the rheology of the solution.

6.4 Experimental Technique

The tank was filled to a depth of 90 mm with the clear solution. The disk was positioned at the center, approximately 90 mm from the sides of the tank. Then, with the disk rotating slowly, a small quantity of the colored solution was added via a syringe into the disk region. The colored fluid subsequently mixed with the clear fluid, and formed a cavern of sheared material close to the disk. The fluid at a distance from the disk was assumed to be stagnant since the dye was not convected into this region. Thus the cavern was visualized as a colored region surrounding the disk. Observations were initiated at the lowest speed and then the speed was gradually increased. In this way the cavern size, as indicated by the colored region, always increased from one observation to the next. Occasionally it was necessary to inject additional colored solution into the cavern to increase the contrast between the fluid in the cavern and the surrounding stagnant fluid. This was due to the dilution of the colored fluid by the clear fluid as the cavern increased in size. When the rotation started, a uniform shape was immediately observed and the cavern size reached steady state after a few rotations. This was confirmed by monitoring the cavern size for approximately 1 minute during which no significant change occurred.

The goal of this part of the experimental investigation was to visualize the development of the cavern around the disk as a function of the global Bingham number, B_n (based on the disk radius, R). For a specific fluid, the global Bingham number can only be changed by varying the speed of the disk. The range of rotational speed in this experiment was between 10 to 1000 rpm. The corresponding range of the Bingham

number for $r = R$, i.e. at the outer edge of the disk was $0.001 > B_n < 0.7$. Photographs of the cavern at low and high speeds are shown in Fig. 6.2.

6.5 Flow Patterns

Agitation and mixing of Newtonian and power law fluids by impellers and disk turbines are reported elsewhere (Elson et al., 1986). When the fluids agitated at very low speeds, the main flow was an outward radial discharge with a return flow into the impeller at approximately 45° ; at higher speeds, a region of rapid turbulent motion developed close to the impeller.

In our case, the flow of a Bingham fluid caused by rotation of a disk is observed to be quite different. The body of fluid is divided into two distinct zones, i.e. the cavern and stagnant fluid. Even at low speeds, a cavern could be seen with the fluid rotating due to the disk. As the speed was increased the cavern maintained the same shape but grew in size; the fluid outside of the cavern remained stagnant (see Fig. 6.2). Further increase in speed continued to increase the cavern size.

Solomon et al. (1981) developed a theoretical model for a spherical cavern centered upon an impeller mixing a fluid with a yield stress. The present flow visualizations (see Fig. 6.2) suggested that the assumption of a spherical cavern is not appropriate. The caverns are obviously not spherical, but instead are somewhat "squashed" giving an

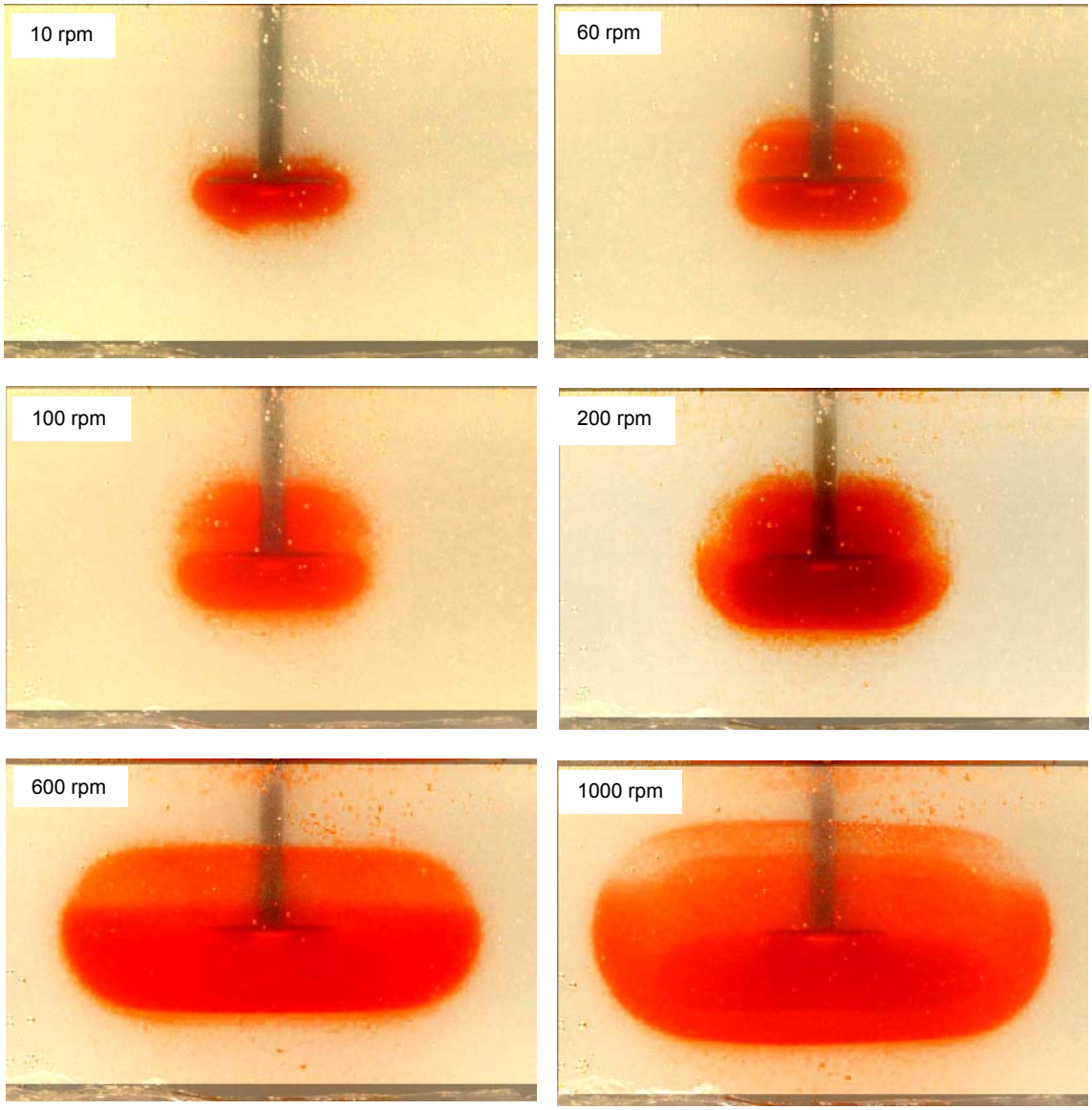

Figure 6.2: Growth of the cavern with speed for a disk rotating in a waxy crude oil simulant

elliptic shape. The dimension of the cavern was characterized by its dimensionless height to diameter ratio h_c/d_c (see Fig. 6.3). It should be noted that the shaft interferes with the upper region, so that for the sake of the experiment, only the bottom region will be considered, as it is shown in Fig. 6.3. The measurement uncertainty for the dimensions of the cavern was estimated to be around 0.5 mm according to the pixel resolution. This uncertainty is partially due to the resolution of the camera, and partially due to the disk position.

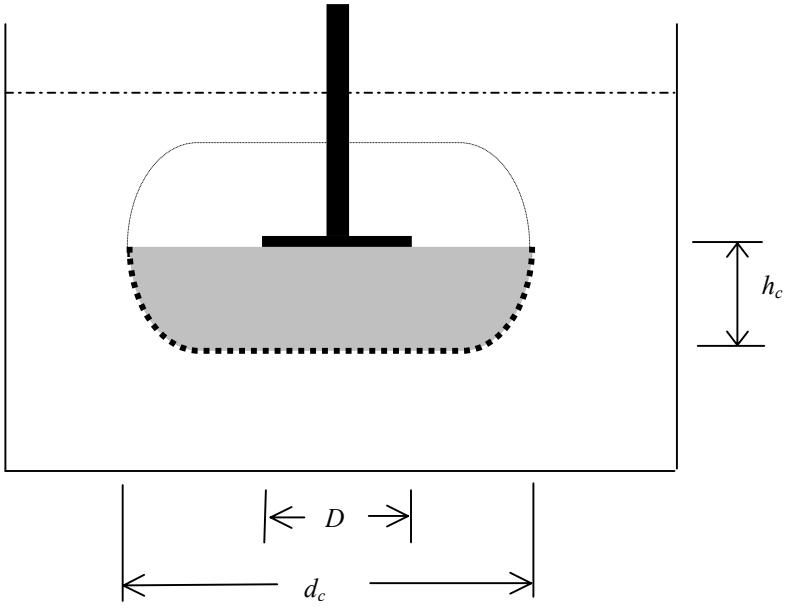

Figure 6.3: Schematic diagram of the shape and dimensions of the cavern

Figure 6.4 shows how the cavern shape, in terms of h_c/d_c, varies with disk speed. It is observed that for rotational speeds up to those at which the cavern boundary

approached the wall or the base, the height to diameter ratio varied over the following range:

$$0.5 \le {h_c}/{d_c} \le 0.6 \qquad (6.1)$$

Thus a value of $h_c/d_c = 0.55$ is a reasonable approximation. Therefore, an ellipse centered on and coaxial with the disk, with a height equal to 55% of its diameter, would be a better model of the cavern shape than a sphere.

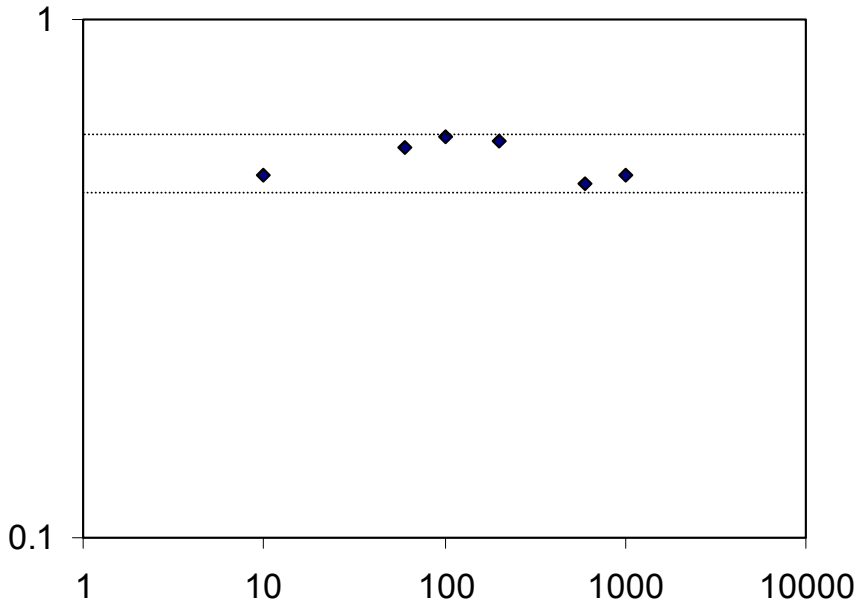

Figure 6.4: Variation of cavern height to diameter ratio with disk rotational speed

A plot of the dimensionless size of the cavern, d_c/D, *and* h_c/D, where D is the disk diameter, versus global Bingham number, B_n, is presented in Fig. 6.5. Figure 6.5

(using logarithmic scales) shows that the dimensions of the cavern decrease with increasing Bingham number, and they can be approximated by the following equations:

$$\frac{d_c}{D} = 0.68\ B_n^{-0.23} \tag{6.2}$$

$$\frac{h_c}{D} = 0.437\ B_n^{0.189} \tag{6.3}$$

From Eqs. (6.2) and (6.3) and the definition of Bingham number which was given in Chapter 3, at a given radial location and for a given fluid, i.e., constant τ_y, it can be concluded that the cavern size depends mainly on the rotational speed. Thus, a higher speed results in a lower Bingham number and larger cavern size.

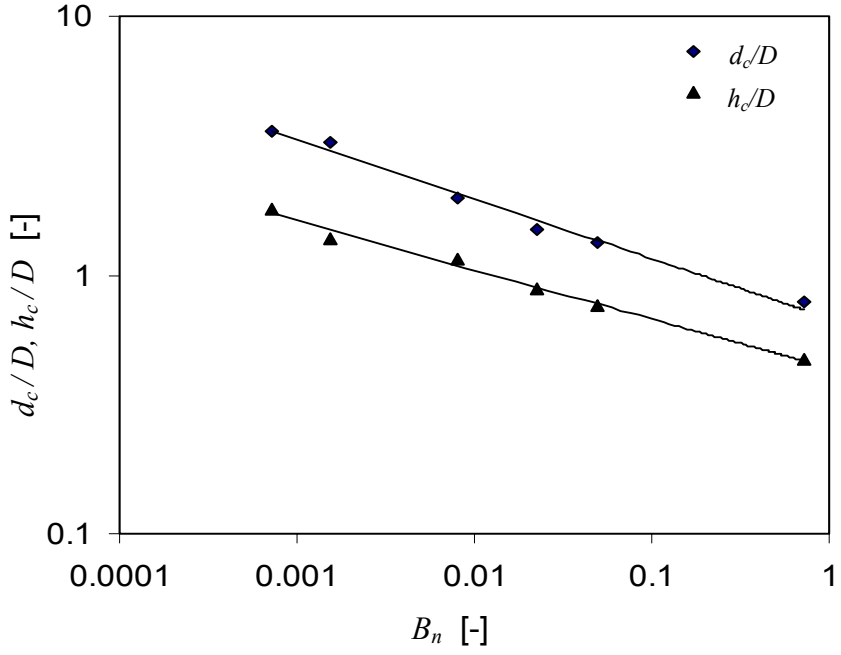

Figure 6.5: Dependence of cavern geometry on Bingham number

Elson et al. (1986) have developed a cavern model for mixing a Bingham plastic fluid with an impeller. It has been used successfully to predict cavern dimensions for a wide range of impeller designs, including a flat disk. The basis of this model is similar to this research in that the stress imparted by the impeller or the disk at the cavern boundary is equal to the fluid yield stress. The model developed by Elson et al. (1986) relates the cavern dimensions, h_c and d_c, the impeller diameter, D, rotating speed, Ω, and material yield stress, τ_y, as follows:

$$\Omega = \sqrt{\frac{4 V_c \pi \left(\frac{h_c}{d_c} + \frac{1}{3} \right) \tau_y}{\left(\frac{h_c}{d_c} \right) \rho N_p D^5}} \tag{6.4}$$

where, V_c is the cavern volume (m^3), ρ is the fluid density (kg/m^3), and N_p is the impeller power number given by

$$N_p = \frac{\rho D^5 \Omega}{P_w} \tag{6.5}$$

where P_w is the power required to rotate the impeller (watts). By adopting this model and using the correlations derived from our experiments, the cavern size of a given fluid can be predicted.

6.6 Summary

The flow visualization technique allows observation of the shear flow patterns resulting from the rotation of a disk in a transparent Bingham fluid. Photographs clearly show the presence of a well-sheared cavern around the disk which grows in size with increasing rotation speed. Outside the cavern, the fluid is stagnant because of the yield stress.

Working with correlations derived from these experiments, the size of the cavern in opaque waxy crude oils of similar rheology to the model fluid can be obtained.

CHAPTER 7

PIV Measurements

In this chapter, the particle-image-velocimetry (PIV) technique is employed for the investigation of both the flow of a Newtonian and a Bingham fluid over a rotating disk. To the author's knowledge, the present study is the first attempt to use PIV to explore the rotating disk problem for a Bingham fluid. The aim of this chapter is to present the experimental results, and compare them to the results predicted by the numerical model, discussed in Chapter 4, and visualization, presented in Chapter 6.

7.1 Experimental Set-Up

PIV measurements were conducted using the experimental configuration shown schematically in Fig. 7.1. The tank and the rotating disk apparatus were the same ones used for the flow visualization described in Chapter 6. The tank provided optical access through all four sides, as well as from beneath via a 150 mm diameter hole in the base table. The laser head was placed horizontally in alignment with the apparatus's base table at a distance of 700 mm from the center of the disk. The laser sheet illuminates the plane of interest within the flowing fluid which is seeded with tracer particles. It extends vertically (normal to the disk surface) and horizontally (parallel to the disk surface) so

that a measuring plane in the axial and radial directions can be illuminated. The particle images were recorded using a cross-correlation digital CCD camera viewing perpendicular to the laser sheet through the side of the tank for vertical plane measurements; then it was moved to the bottom of the tank for horizontal plane measurements.

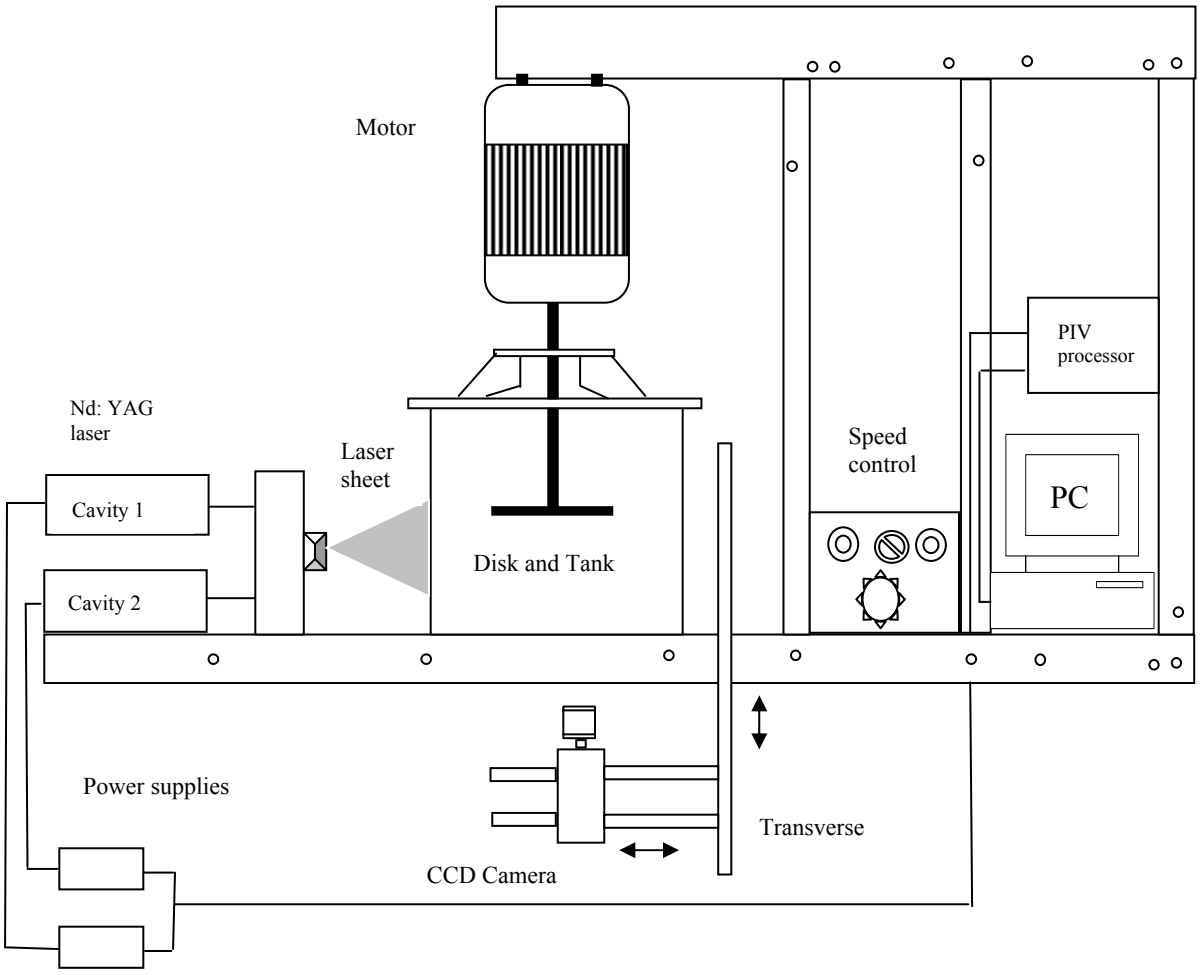

Figure 7.1: Schematic of the PIV set-up

7.2 The PIV System

The PIV system used for this investigation has been constructed in house over the last six years by Prof. J. D. Bugg, and allows two-dimensional planer measurements. Dual Nd:YAG lasers manufactured by New Wave Research Ltd. are used as the illumination source. They can supply pulses at a wavelength of 532 nm with energy of 50 mJ/pulse and a very short individual pulse duration of 6 ns. A Berkeley Nucleonics Inc. 500B pulse generator was used to trigger the lasers and provide synchronization with the camera. It could be programmed to give any desired pulse separation. It is important to match the thickness of the illuminating light sheet to the flow field being investigated using PIV measurements. If too thin, particles will traverse the sheet too quickly and data will not be obtained; if too thick, the light intensity will not be great enough to illuminate the seeding particles and it also decreases spatial resolution. A spherical lens (250 mm focal length) combined with a cylindrical lens (-12.7 focal length) transform the laser beam into a thin light sheet. By adjusting the distance between these two lenses and the distance from lenses to field-of-view, the desired thickness and width of the light sheet can be obtained. The light sheet thickness in this work was approximately 1.0 mm at the center of the field-of-view.

The field-of-view was imaged with a 1008 x 1018 pixel Kodak ES 1.0 Megaplus camera operating in dual capture. The camera was equipped with a 60 mm Nikon Micro Nikkor lens and the object distance was adjusted to give the field-of-view required for each image. The camera was then focused and calibrated by taking a picture of a ruler in the tank. This allowed the computer to relate the actual length of the disk in the tank to

the distance in pixels on the computer screen. This calibration also allowed the system to accurately determine the distance between two moving particles and it calibrates all positions on the image. The raw images typically looked like the image shown in Fig. 7.2.

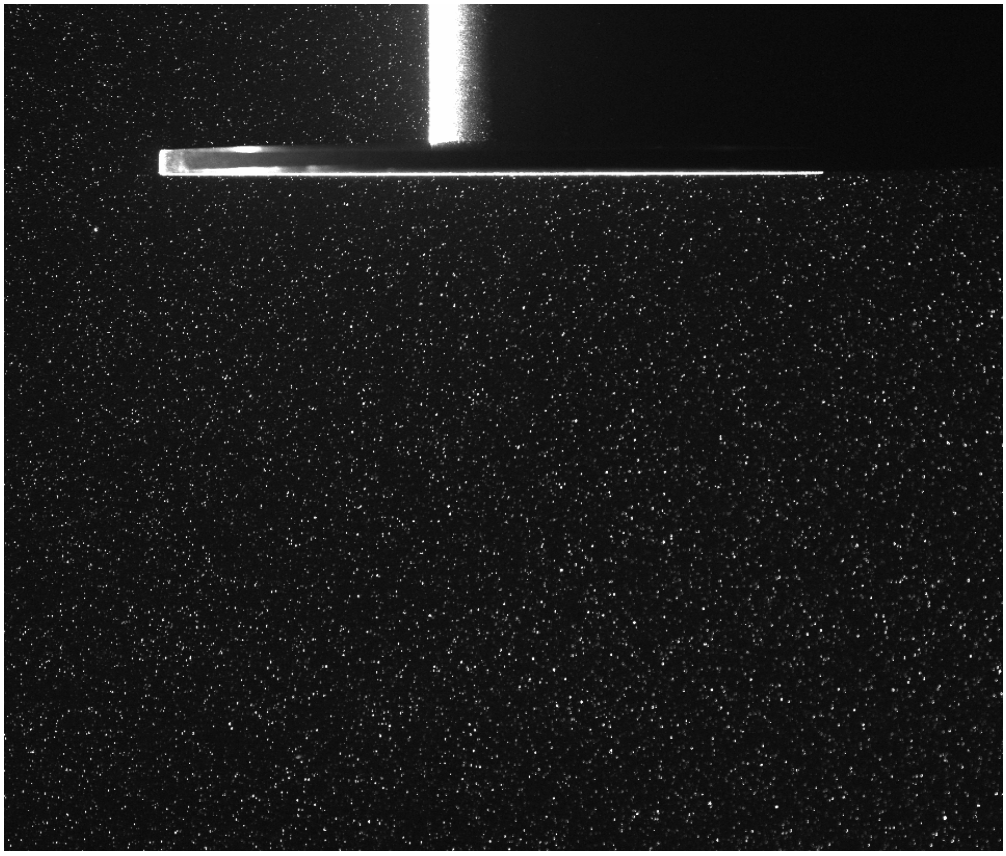

Figure 7.2: Typical instantaneous image in a vertical plane at Ω = 30 rpm

7.3 Test Fluids and Flow Seeding

In this study, the test fluids were filtered tap water and a commercial hair gel (Alberto ultra gel) diluted with water to a concentration of 50 wt%. Excessive dilution of the hair gel causes a loss of transparency of the fluid, which is a key issue for optical

access. Therefore, the 50 wt% concentration was the limit, even though the fluid is still very viscous with a high yield stress, all of which makes it very challenging to work with. The properties of the mixture were given previously in Chapter 5.

Both fluids were seeded with tracer particles, in this case silicon carbide 2 μm in diameter and with a density of 3200 kg/m^3. Even though the density of silicon carbide is high compared to water, the small particle size ensures that they passively follow the motion of the fluid. A specific advantage is that their refractive index is high (2.65) so they appear quite bright. Seed density control is important for the quality of PIV images. Keane and Adrian (1995) recommended minimum seed densities of 10-12 particle images within each interrogation volume.

Flow seeding can be a problem in centrifugal flows, especially when the rotational speed is high. In swirling flow, a particle tends to move radially outward, and may vacate the flow region of interest. Durst et al. (1981 p 292) and Burson et al. (1967) analyzed particle motion in a centrifugal field. They noted that the radial drift of the particle in a rotating flow may cause low particle concentration. The particle radial velocity V_p, following Stokes drag law can be calculated from the following equation (Burson et al., 1967),

$$V_p = \frac{r\,\Omega^2\,{d_p}^2\,\rho_p}{18\mu} \tag{7.1}$$

where r is the radial location, Ω is the rotational speed, d_p is the diameter of the particle, ρ_p is the particle density and μ is the fluid viscosity. Clearly the particle radial velocity increases with both the square of the particle diameter and the rotational speed. If an

average particle diameter of 2 μm is assumed for this study, the V_p of a particle in water at r = 9 mm (approximately one half of the radius of the disk) for Ω = 1000 rpm was calculated to be approximately 1 μm/sec. This relatively low speed allowed sufficient time for operating the camera shutter and firing the laser. It was found that satisfactory particle concentration could be achieved for the disk rotating at speeds below 5,000 rpm, if sufficient care was taken (Durst et al., 1981). Particles with small diameters will easily follow the liquid flow induced by the disk.

7.4 Field-of-View

The fluid velocity was measured along the vertical (*r-z* plane) and horizontal (*r-*ϕ plane) planes. The vertical plane, for which the plane of illumination was normal to the disk and intersected the axis of rotation, gives the velocity field in the radial and axial directions. Velocities on the vertical plane were measured for both water and the gel for a range of rotational speeds, Ω. For water (B_y = 0) the measurements were taken at Ω = 10, 30 and 60 rpm. For the purpose of comparison with numerical results, the measurements for the gel ($0 < B_y \leq 3$) were taken at Ω = 30, 60 and 1200 rpm.

Since the flow over a rotating disk is symmetric (Owen and Rogers, 1987). , only a single quadrant of the entire flow field was recorded in the vertical plane (*r-z* plane). The design, dimensions and the coordinate system related to the experimental setup are shown in Fig.7.3. It also shows the two fields of view, the field of view denoted “I” was used for water, while the field of view denoted “II” was used for the gel. For water the field of view was relatively large, 21 mm x 16 mm, which corresponds to 22% and 12%

of the width and height, respectively, of the quarter of the tank profile located beneath the disk. However, due to the poor visibility of the diluted gel, which is less transparent than water, the camera was moved closer to the tank. In doing so, the size of the field of view was compromised; for the gel it was 14 mm x 10.7 mm, or 15% and 8% of the width and height, respectively, of the quarter of the tank profile beneath the disk.

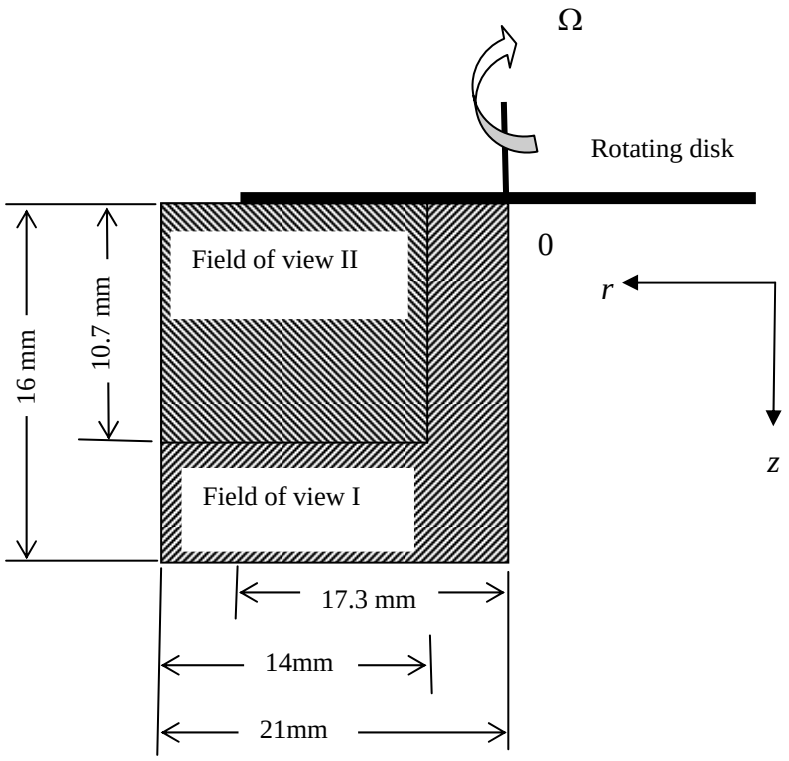

Figure 7.3: Location of PIV measurement field in the vertical plane: I-Newtonian fluid; II-Bingham fluid

The horizontal plane, for which the plane of illumination was parallel to the disk, gives the velocity field in the radial and tangential directions. Velocities on the horizontal plane were measured for both water and the gel just below the surface of the disk (z = 0.5 mm). The schedule for using the PIV system did not allow time to consider additional z locations. Even though measurements at the disk surface will not give information about

Table 7.1: Characteristics of the two PIV measurement planes

Orientation of measurements plane		Rotational speed (Ω)	Bingham number (B_y)	Size (mm x mm)	Δt (μs)	Spatial resolution (mm)*
Water	Vertical	10	0	16 x 21	30,000	0.1744
	Vertical	30	0	16 x 21	33,000	
	Vertical	60	0	16 x 21	26,000	
Gel	Vertical	30	2.2	10.7 x 14	25,000	0.116
	Vertical	60	0.77	10.7 x 14	10,000	
	Vertical	1200	0.0086	10.7 x 14	800	
Horizontal		10	0 & 11.3	44 x 44	18,000	0.348
Horizontal		30	0 & 2.2	44 x 44	15,000	
Horizontal		60	0 & 0.77	44 x 44	7,500	
Horizontal		100	0 & 0.35	44 x 44	6,500	
Horizontal		250	0 & 0.09	44 x 44	4,000	
Horizontal		1200	0& 0.0086	44 x 44	400	

* corresponds to 8 pixels

the variation of the velocity field along the axial direction, they can help to visualize the flow and understand the behavior of the material under shear. Thus, flow measurements at z = 0.5 were taken at a wide range of speeds, i.e., Ω = 10, 30, 60, 100, 250 and 1200 rpm. Table 7.1 summaries the range of rotational speed, size of the two measurement planes considered in this study, the time between frames, and the achieved spatial resolution.

7.5 Data Analysis

7.5.1 PIV Image Analysis

Interrogation of the recorded PIV images was performed by two-dimensional cross-correlation using PIV analysis software (Ver. 1.5.1) developed at the University of Saskatchewan.

The basic image analysis procedure begins by extracting smaller portions (interrogation areas) of these images from the same location on each image. This analysis procedure used an interrogation area of 32 x 32 pixels and adjacent interrogation areas were overlapped by 50%. The software then computes a two-dimensional cross-correlation function for this interrogation area. The correlation-based correction (CBC) method proposed by Hart (2000) was used to enhance the correlation signal-to-noise ratio and limit the number of spurious vectors. This analysis was repeated one more time to complete a two-level analysis and yield a final interrogation area size of 16x16 pixels. The actual computation of the cross-correlation function is most efficiently computed using Fast Fourier Transformations, FFTs. For good images there should be a distinct

peak in this correlation function. The location of this peak (spatial displacement) will correspond to the average particle displacement in the interrogation area. A peak finding algorithm locates the peak to sub-pixel accuracy using a Gaussian peak model. The average displacement of the particle is divided by the time between the laser pulses to yield a two-dimensional velocity measurement for that interrogation area. The procedure is then repeated for all interrogation areas on the image. It should be noted that the time between frames, Δt, varied to accommodate the significant range of rotational speeds (see Table 7.1).

Even though the flow is known to be laminar, 50 images were acquired for each measurement. Ensemble averages based on these 50 pairs of images tend to eliminate any variation that might exist. Example of one velocity vector map and ensemble averaging of 50 velocity vector maps are given in Appendix D

7.5.2 Outlier Rejection Strategy

The raw (non-validated) vector maps resulting from the interrogation of original PIV images have a number of erroneous vectors depending on flow conditions and the PIV image quality. These erroneous vectors (outliers) could be attributed to a combination of the following effects: high velocity gradients; random positioning of particles in the images; out-of-plane velocity components causing one of the particle image pairs to move out of the illumination light sheet; as well as shot noise on the digital imaging device. To improve the measurement, a refinement procedure was necessary to correct any significant erroneous velocities. Outliers were rejected with software

developed in-house by Prof. J. D. Bugg (Ver. 1.1.0 mod). It uses the cellular neural network (CNN) method with a variable threshold as a post-interrogation algorithm to detect spurious vectors. A detailed explanation of how this procedure works was given in Shinneeb et al. (2004). Due to the use of silicon carbide seeding, a good signal-to-noise ratio was obtained even in the close proximity of the disk. Therefore, the number of rejected vectors (outliers) did not exceed 15% and were replaced using a Gaussian mean of their neighbors.

7.5.3 Measurement Errors

The estimation of the uncertainty of PIV velocity measurements requires consideration of several aspects. Systematic errors occur due to the uncertainty in the determination of the geometrical parameters (e.g. variations in the disk speed) and the fabrication tolerances of the camera devices and lenses. Non-systematic errors are mainly due to the uncertainty in the determination of the average particle displacement in the interrogation area. The errors depend on the size of the interrogation area, the time separation between the laser pulses, the magnification of the recording, the out-of-plane velocity component. The choice of the recording and interrogation parameters is therefore of significant importance for accurate and reliable velocity measurements. Also, it is necessary to make a compromise when selecting the minimum pulse time in areas with large velocity gradients in order to enable both the minimum and the maximum velocities to be reliably recorded. Further details of the PIV uncertainties are given in Westerweel (1997). Studies using similar methods have stated uncertainties of approximately 3% to 10% (Prasad and Adrian, 1993).

7.6 PIV Experimental Results

In this section we present PIV results for the shear dominated flow driven by a rotating circular disk. We are particularly interested in the flow characteristics of the near-disk region where the highest shear occurs. Numerous images such as Fig. 7.2 for both the vertical and the horizontal planes were recorded and analyzed following the procedure described in Section 7.5. Note that in all the figures the field of view in the vertical plane is smaller for the Bingham fluid as described in Section 7.4.

7.6.1 Vertical Plane: Water

Typical PIV velocity measurements for water, obtained from ensemble averaging 50 pairs of images, in the disk region of the vertical plane (r-z) are shown in Fig. 7.4. It should be noted that the figure indicates the image boundaries and not the extent of the tank. Figure 7.4 (a), (b) and (c) show the PIV velocity measurements for speeds of Ω = 10, 30 and 60 rpm, respectively. The arrow indicated above each figure represents the scale of the velocity vector. At all rotational speeds, away from the axis of rotation and near the disk surface, the radial velocity component always dominates over the axial one. To satisfy continuity, the axial inflow approaching the disk decreases and the effect of the disk is to redirect the fluid in the radial and tangential directions. Hence, this fluid flow has three non-zero velocity components and is certainly not parallel to the axis of rotation. Figure 7.5 (a), (b) and (c) show a blow-up of the near disk region, to give better idea of the flow pattern in the boundary layer. One may recognize that the upcoming flow is deflected radially before it reaches the disk due to the acceleration associated with the rotation of the disk.

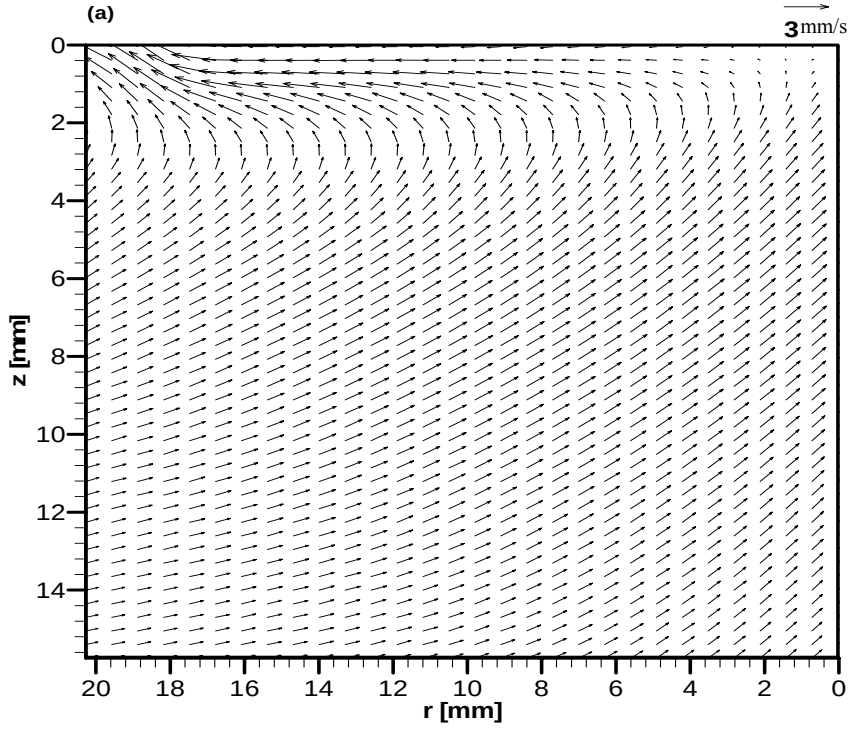
(a)
3 mm/s
z [mm]
r [mm]
0
2
4
6
8
10
12
14
20
18
16
14
12
10
8
6
4
2
0

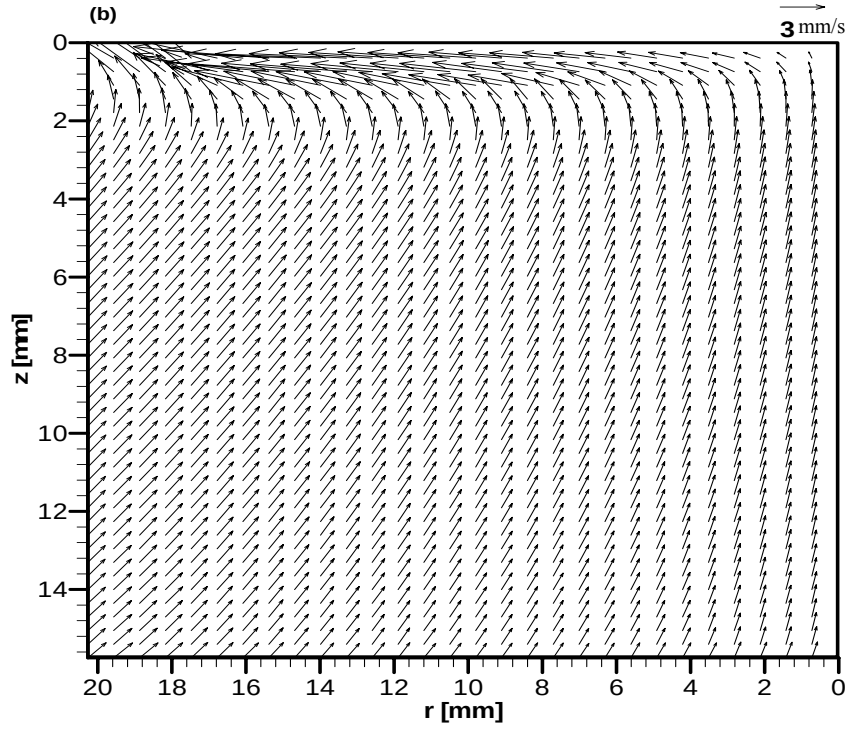
(b)
3 mm/s
z [mm]
r [mm]
0
2
4
6
8
10
12
14
20
18
16
14
12
10
8
6
4
2
0

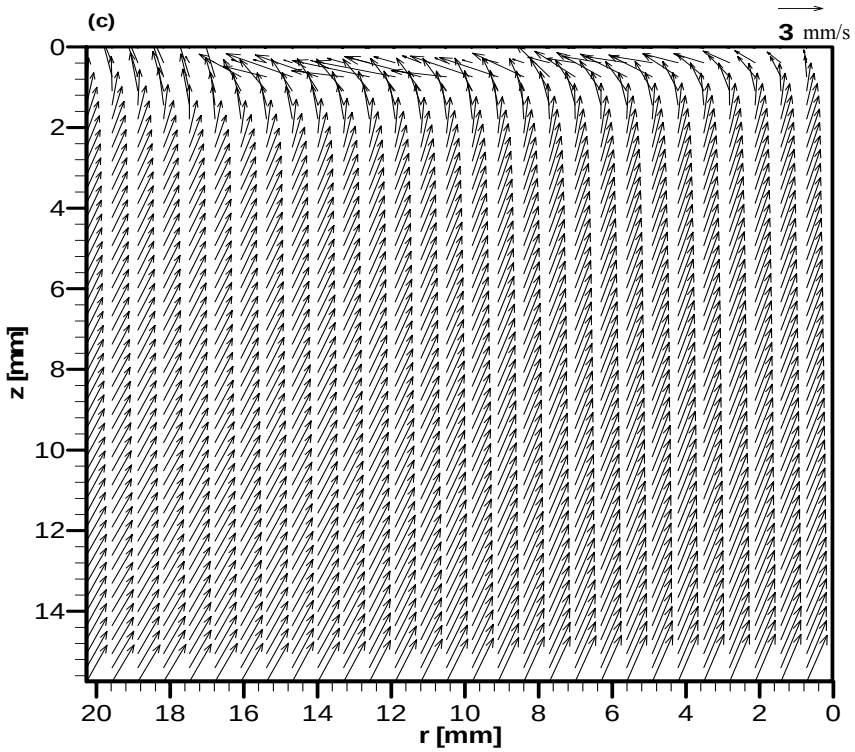

Figure 7.4: PIV velocity measurements of water (field of view I) in the (*r*-*z*) plane: (a) Ω = 10 rpm; (b) Ω = 30 rpm; (c) Ω = 60 rpm

The influence of increasing the rotational speed appears to shift the maximum velocity vector to a location closer to the disk. High velocities near the tip of the disk are apparent. These velocities indicate that the flow being deflected upward as a result of the large effect of the confinement of the tank.

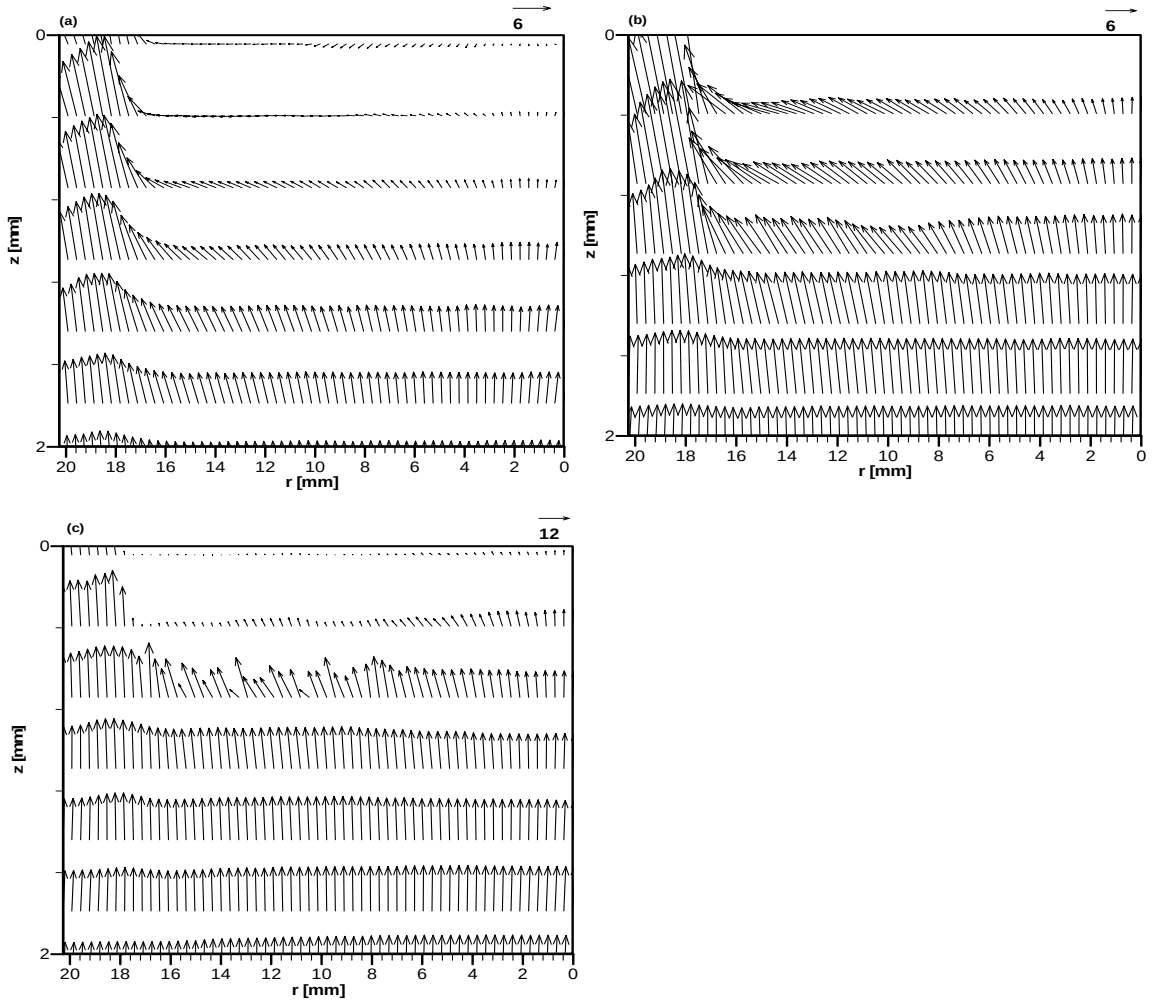

Figure 7.5: A blow up of the PIV velocity measurements of water close to the disk region: (a) Ω = 10 rpm; (b) Ω = 30 rpm; (c) Ω = 60 rpm

The dimensionless axial, H, and radial, F, velocity components were defined in Chapter 3, in Eq. (3.12). Their profiles for water, at Ω = 60 rpm, along the radial axis are shown in Figs. 7.6 and 7.7, respectively. This rotational speed was chosen to compare the flow of water and the gel over a rotating disk, given that a 60 rpm relatively represents high and low rotational speed for water and gel, respectively. The irregularity in the axial

velocity profile near the disk surface is probably due to the perspective effect caused by the large out-of-plane displacement adjacent to the disk or the laser light sheet intersecting with the solid disk. Despite this irregularity, the notion of radial independency that was assumed in the numerical simulation appears to be approximately valid (see Fig. 7.7). The change of the flow from the axial to the radial direction is associated with a narrow boundary layer region, the thickness of which is approximately constant. This is demonstrated in Fig.7.7, which shows the variation of the radial velocity profile along the radial direction. The profile of the radial velocity decreases to zero at a location which marks the edge of the boundary layer. This figure also shows a significant variation of the profile outside the boundary layer region, which might be caused by the presence of the walls of the tank.

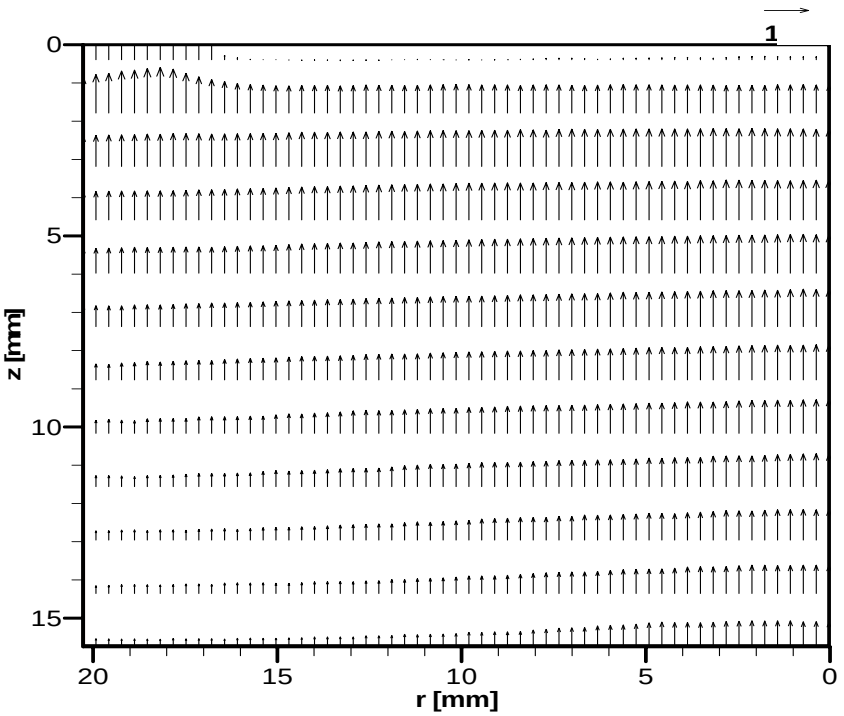

Figure 7.6: Dimensionless axial velocity of water at a rotational speed of Ω = 60 rpm

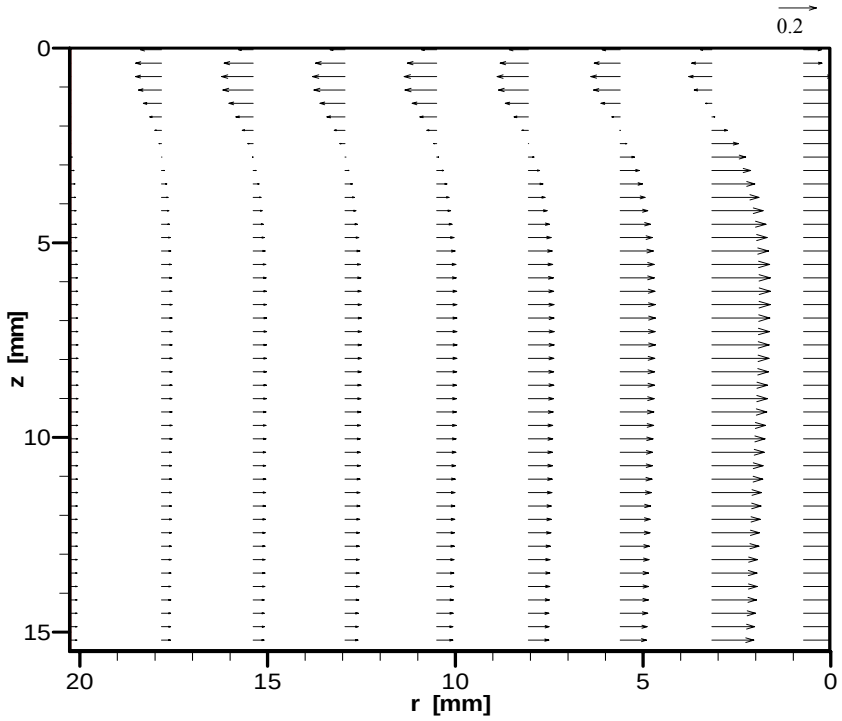

Figure 7.7: Dimensionless radial velocity, F, for water at a rotational speed of Ω = 60 rpm

It can also be noted that while the radial velocity, F, peaks at approximately $z = 1$, it vanishes at the wall due to the no-slip condition. In the boundary layer region ($z < 4$), because F decreases rapidly at large z, the axial velocity, H, approaches to an asymptotic value at finite z (see Fig. 7.6).

7.6.2 Vertical Plane: Gel

Figures 7.8 (a) and (b) show the development of the velocity field for the gel in the (r-z) plane for speeds of Ω = 30 and 60 rpm, respectively. According to the von Kármán's solution, one would expect, the rotation of the disk draws fluid axially toward the surface, and as the fluid approaches it gains tangential velocity and exits radially. However, the gel at relatively low rotational speeds (Figs. 7.8 (a) and (b)) shows a more complex behavior than does the water. This departure from the Newtonian case is attributed to the yield surface which confines the flow within a region of high shear. At low rotational speeds, the shear stress created by the disk is not strong enough to overcome the yield stress of the gel except near the disk,

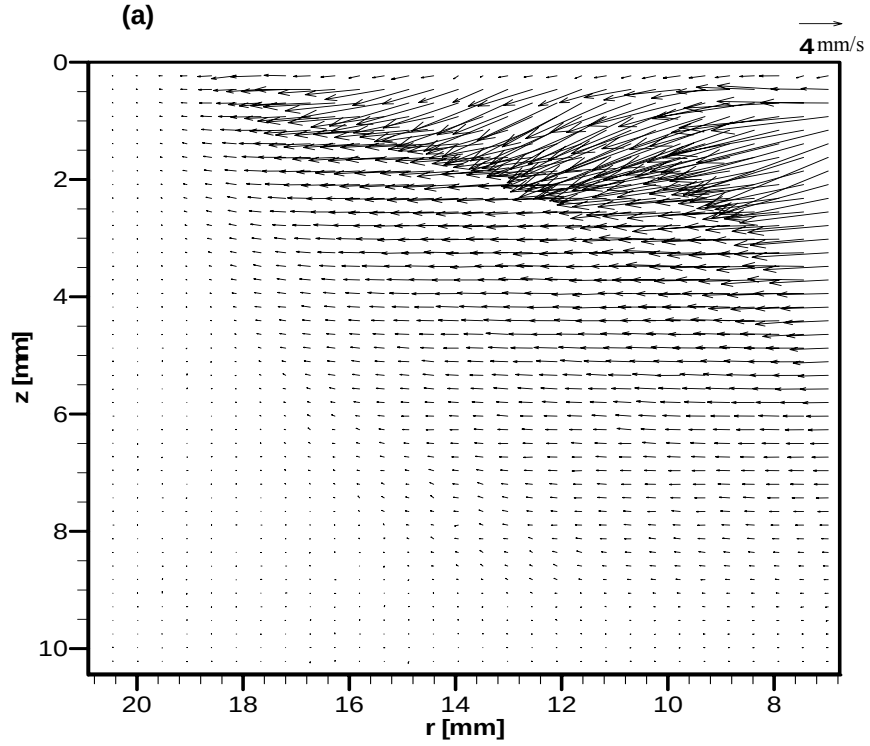

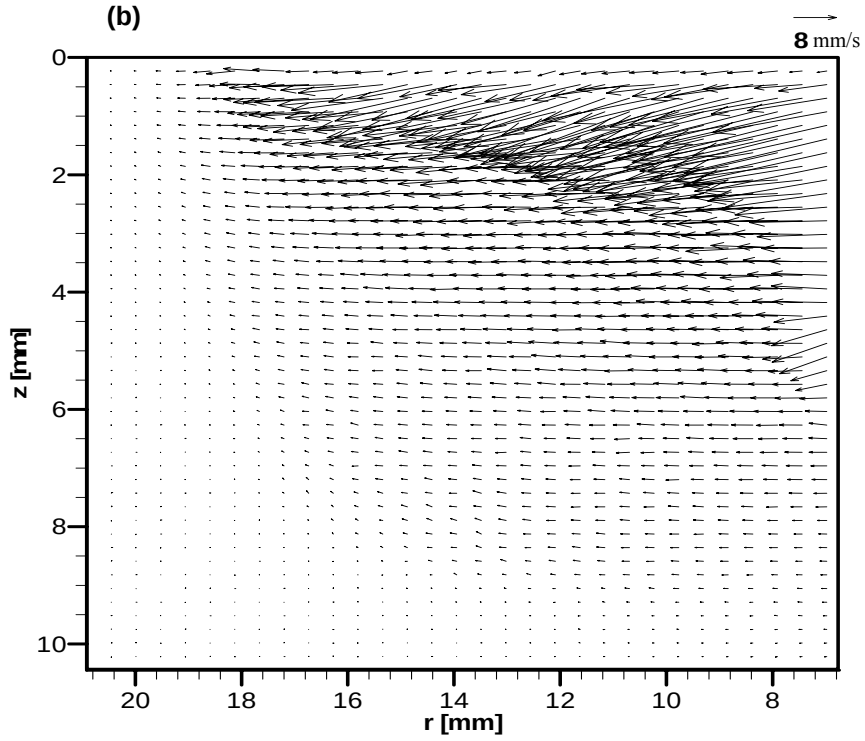

Figure 7.8: PIV velocity measurements of gel (field of view II) in the (*r*-*z*) plane: (a) Ω = 30 rpm; (b) Ω = 60 rpm

and the rotational flow consists of a re-circulating cavern flow, similar to that observed in Chapter 6. This cavern shape identifies the yield surface which separates the plug region from the shear region. Figure 7.9 shows the PIV velocity profile superimposed on top of a visualized cavern at the same rotational speed (Ω = 60 rpm). The shape and the boundary of the yield surface can be clearly seen in this figure.

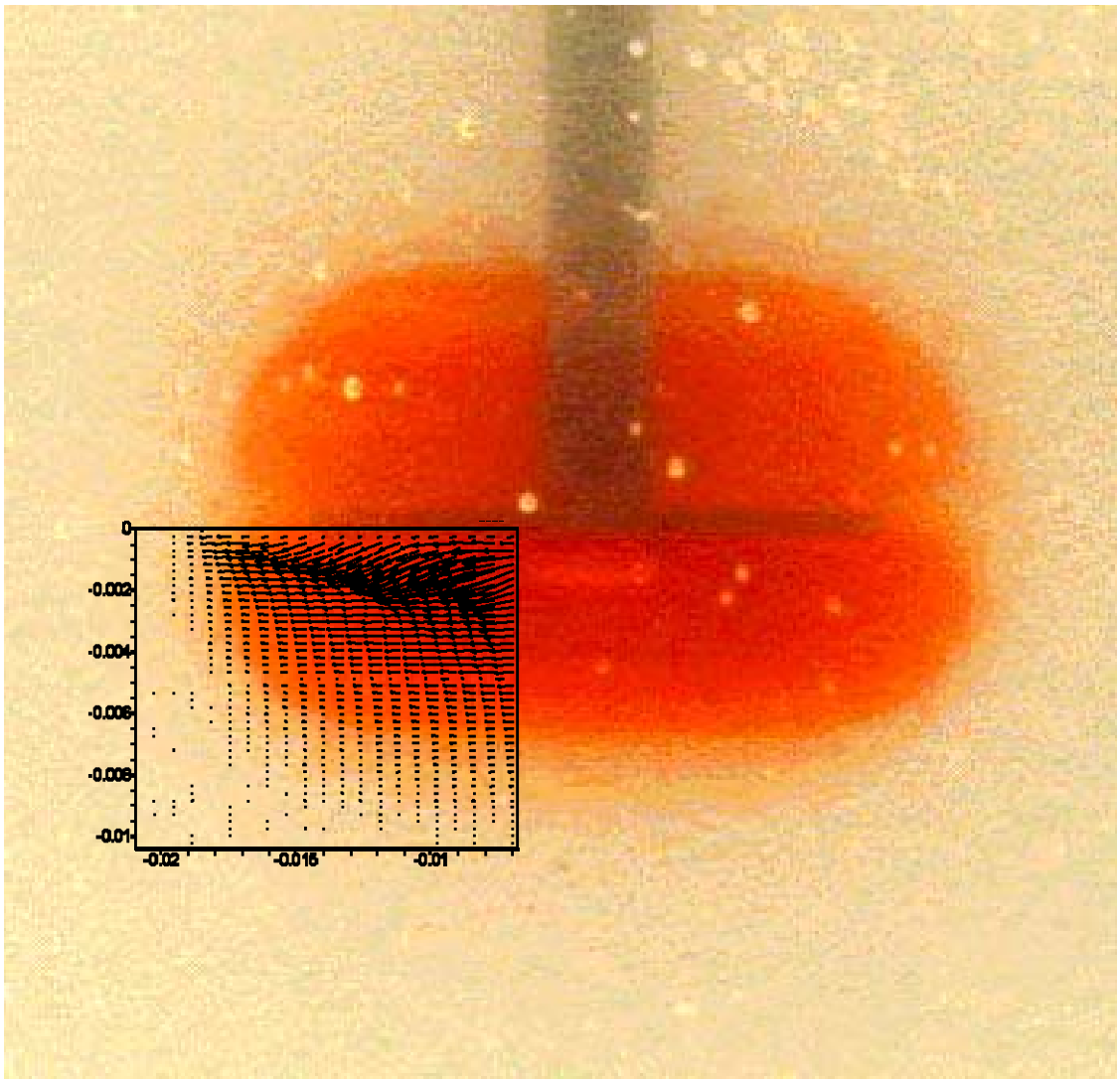

Figure 7.9: PIV vector maps of velocity data superimposed on top of a visualized cavern (Ω = 30 rpm)

In Fig. 7.10, a small negative axial velocity component is observed near the disk, while Fig. 7.11 indicates a strong radial variation in the profile of the radial velocity component. This departure from the Newtonian case is likely due to the finite domain of the flow caused by the yield surface.

This surprising result can be explained by examining the *r*-wise momentum equation following the approach taken by Prasad and Adrian (1993) who implemented stereoscopic PIV to perform three-dimensional measurements below a disk rotating in a tank of glycerine, a Newtonian fluid. The *r*-wise momentum equation was given in Chapter 3, Eq. (3.4), and it is given below to lead the following discussion.

$$\rho\left(v_r\frac{\partial v_r}{\partial r}+v_z\frac{\partial v_r}{\partial z}-\frac{{v_\phi}^2}{r}\right)=-\frac{\partial p}{\partial r}+\frac{\partial \tau_{rr}}{\partial r}+\frac{\partial \tau_{rz}}{\partial z}+\frac{\tau_{rr}-\tau_{\phi\phi}}{r} \tag{7.2}$$

The numerical solution (infinite disk) has $p = p(z)$ and therefore the pressure gradient term in Eq. (7.2) is zero. However, in the case of the Bingham fluid which is bounded by the yield surface, $p = p(r, z)$. The outward flow (radial velocity, v_r) experiences an adverse pressure gradient, i.e., $\partial p/\partial r > 0$. As a consequence, the outward flow is reduced relative to the infinite disk case. (At a large enough distance from the axis, the adverse pressure gradient forces the flow downwards, as shown in Fig. 7.10).

The yield surface has a strong effect on the axial flow as well, since the axial flow predicted by the numerical model is now severely restricted by the cavern. While the axial velocity, v_z, is large and positive along the axis of rotation (not measured, but it can be predicated by analogy to Prasad and Adrian's measurement), it decreases away from it, and eventually becomes negative. Therefore, the radial velocity along the radius is substantially smaller for the Newtonian case as is seen when comparing Figs. 7.11 and 7.7.

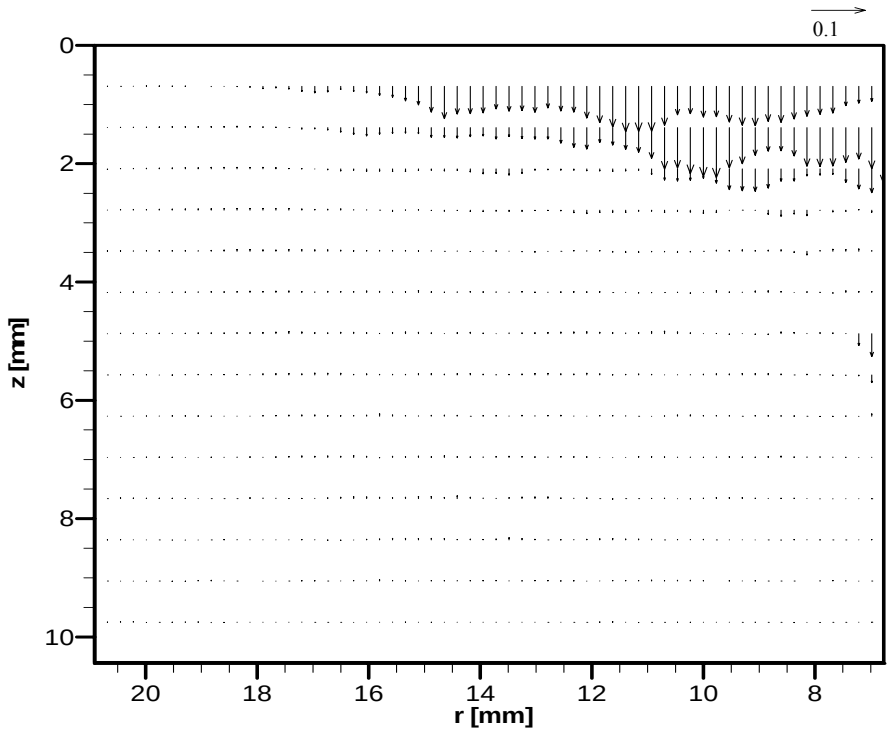

Figure 7.10: PIV vector profile of the dimensionless axial velocity of the gel at rotational speed of $\Omega = 60$

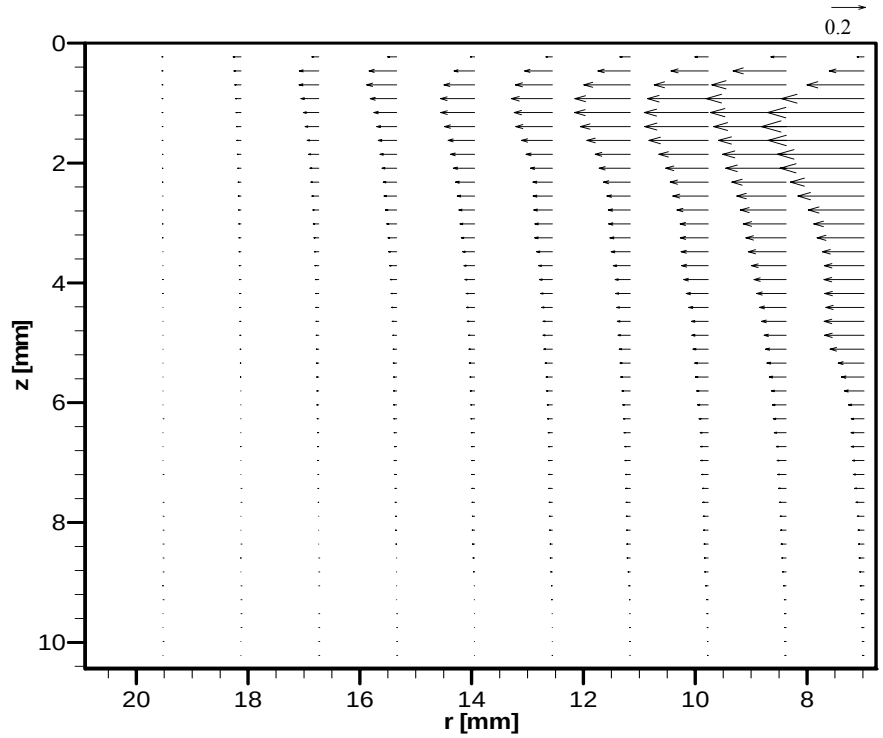

Figure 7.11: PIV vector profile of the dimensionless radial velocity of the gel at rotational speed of $\Omega = 60$

When the rotational speed is increased to 1200 rpm, Fig. 7.12, the disk induces a shear stress which overcomes the yield stress. More specifically, the local viscous stresses become larger than the yield stress of the gel for a large region of the flow. As a result, the flow field tends toward a pattern which is similar to the Newtonian case. A recirculation zone was also observed to be present in the far field. This was caused by the yield surface that formed in response to the viscous stresses. However, due to the limited field of view in the experiments, no clear conclusion on the formation of this

recirculation zone can be drawn. In order to study this behavior, a systematic study with a wider range of speeds should be carried out.

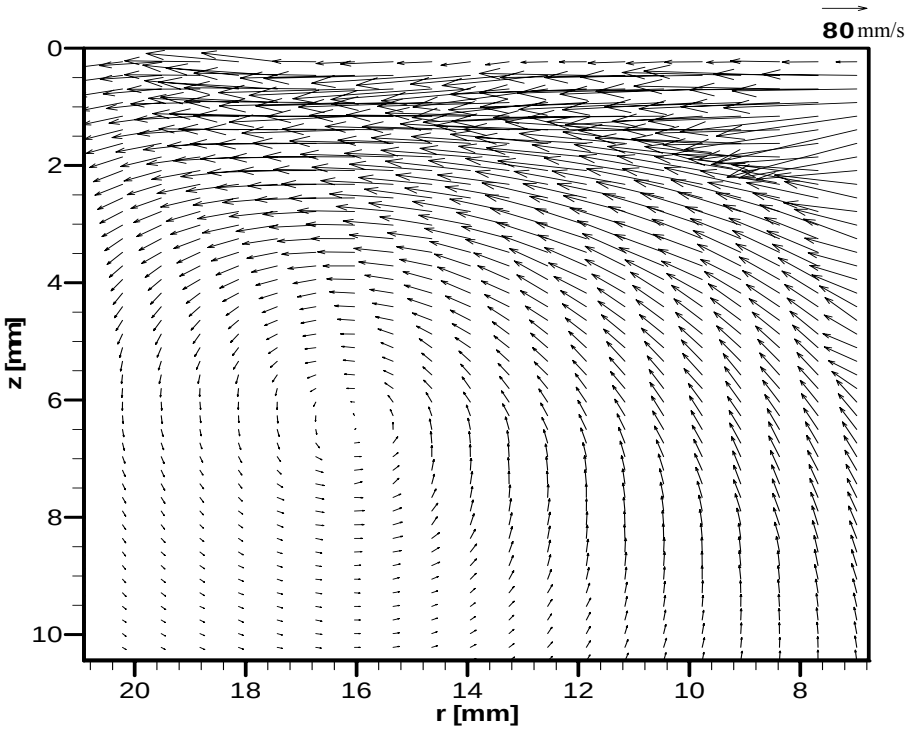

Figure 7.12: PIV velocity measurements of gel (field of view II) in the (*r*-*z*) plane: Ω = 1200 rpm

The development of the dimensionless radial and axial velocity profiles, for Ω = 1200, along the radial axis is shown in Figs. 7.13 and 7.14, respectively. The negative axial component in the vectors adjacent to the disk could be due to the perspective effect caused by the large out-of-plane displacement adjacent to the disk (Prasad and Adrian,

1993). It is also noted that even at this relatively high rotation rate the velocity profiles still exhibit a radial variation. This behavior contradicts an important assumption of the similarity problem as formulated by von Kármán.

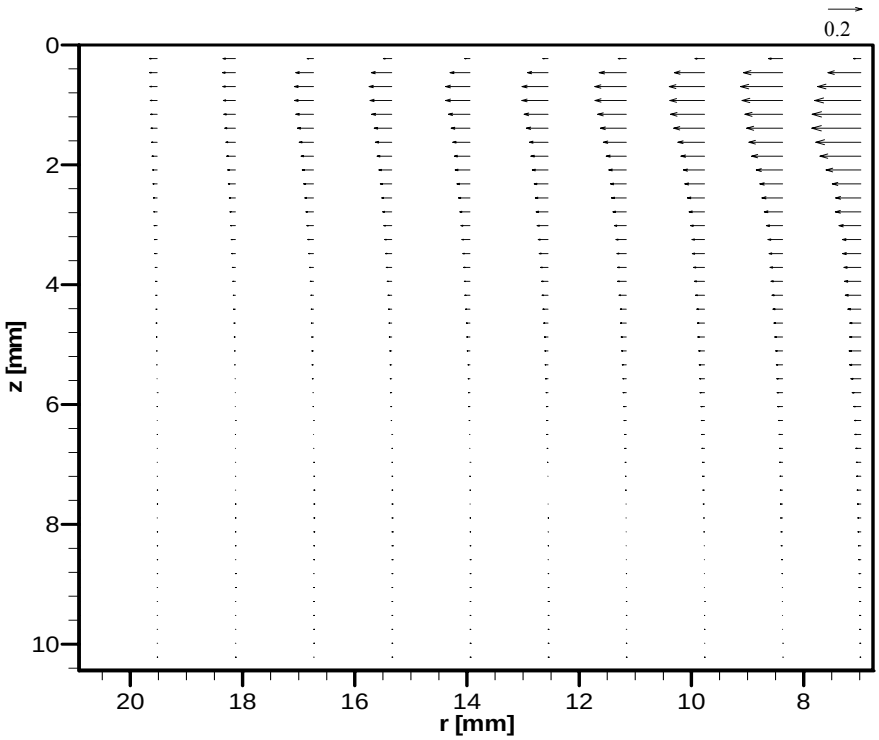

Figure 7.13: PIV vector profile of the dimensionless radial velocity of the gel at rotational speed of Ω = 1200 rpm.

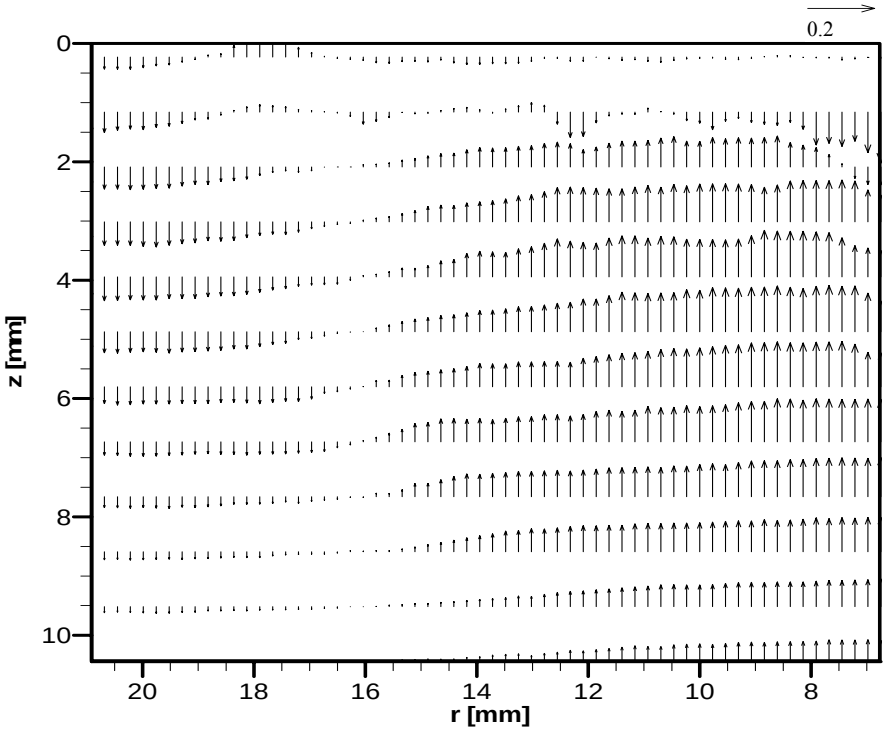

Figure 7.14: PIV vector profile of the dimensionless axial velocity of the gel at rotational speed of Ω = 1200 rpm

7.6.3 Horizontal Plane

Figure 7.15 (a) and (b) shows the velocity vector maps acquired at a location just below the disk surface (approximately at z = 0.5 mm) in the horizontal plane (r-ϕ), for both water and the gel at rotational speed of Ω = 30 rpm, respectively. Figure 7.15 (a) shows that the water was sheared in the entire neighborhood of the disk. On the other hand, for the gel, Fig. 7.15 (b) indicates a low-velocity zone beyond the perimeter of the disk. Note that the circle on the figures indicates the edge of the disk. Similar velocity vector maps at higher rotational speeds are given in Appendix D.

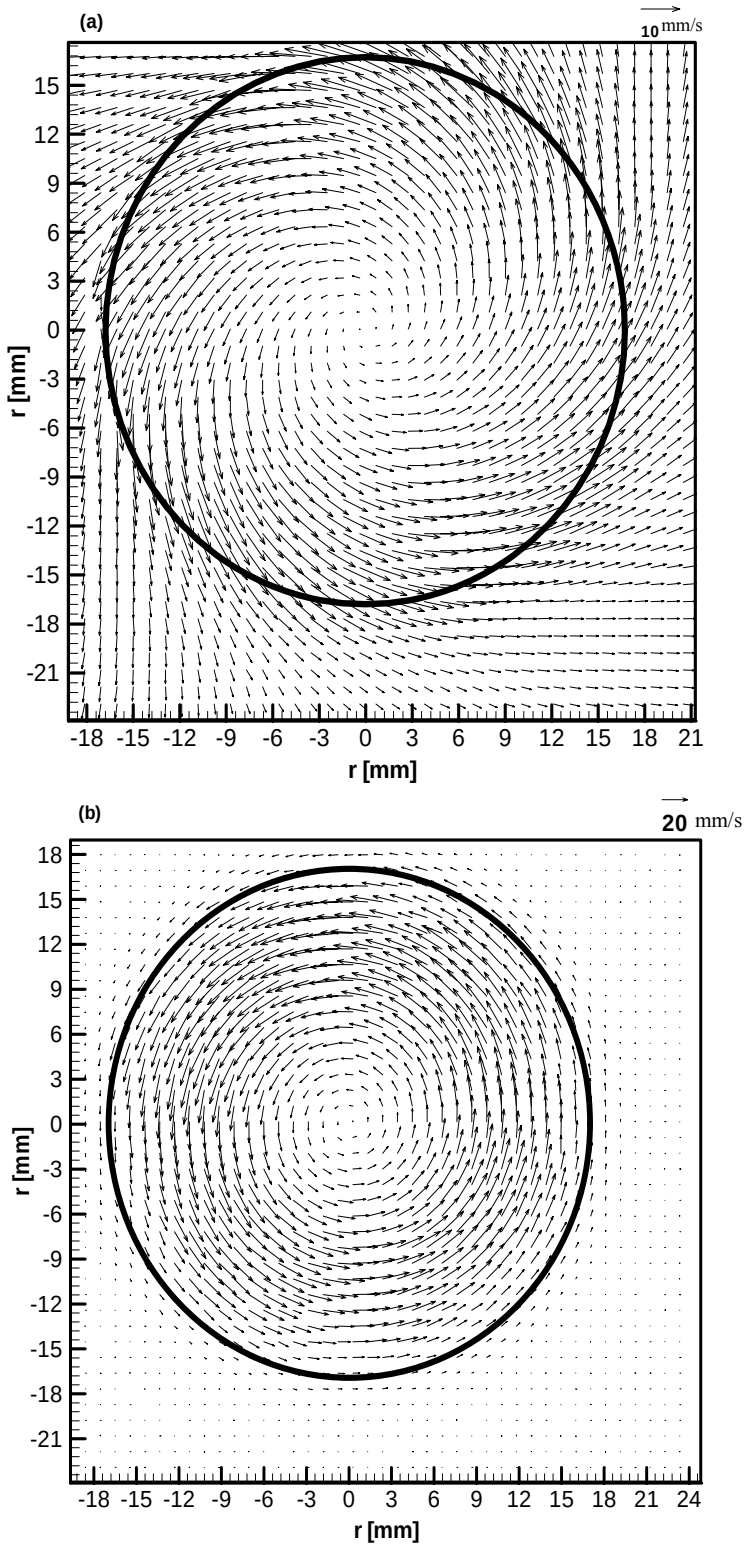

Figure 7.15: PIV velocity vectors at the surface of the disk in the (r-ϕ) plane at Ω = 30 rpm: (a) water; (b) gel

The yield stress has an important effect on the shape of the tangential velocity profile as shown in Fig. 7.16. It shows that the velocity profiles reach their peak values at $r = R/2$, and reduce to zero at the axis of symmetry and outer edge of the disk, $r = R$. A different trend was noticed at the higher speed, Ω = 1200 rpm as shown in Fig. 7.17, where the location of the maximum velocity shifts closer to the edge of the disk. This

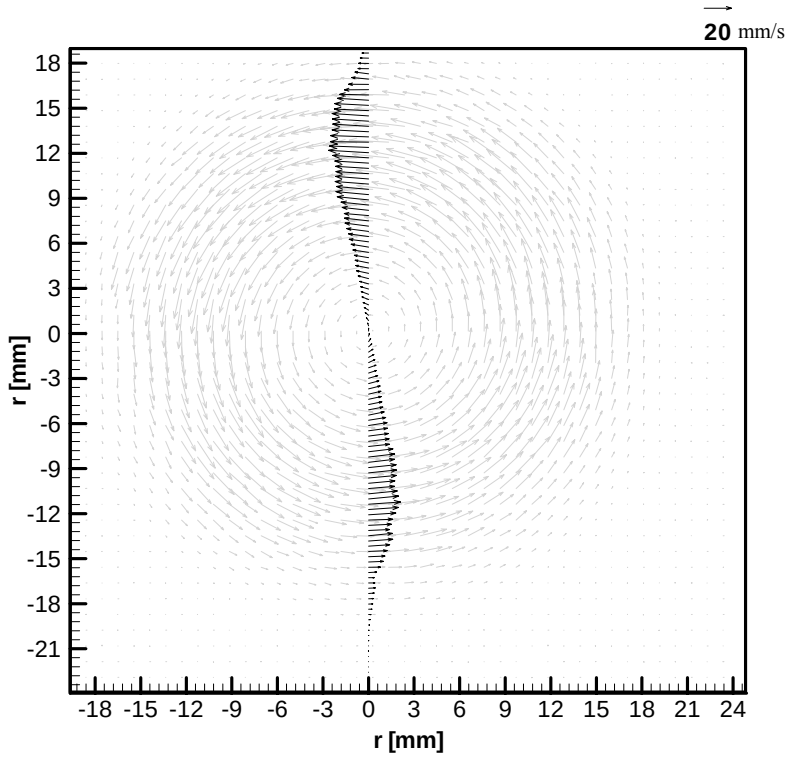

Figure 7.16: PIV vector profile of the tangential velocity of the gel along the radial axis at rotational speeds of Ω = 30 rpm

behavior indicates that the gel begins to behave more like the Newtonian case as shown in Fig. 7.18 for water. This behavior of the gel at high speed is attributed to the reduction of the Bingham number with the rotation rate.

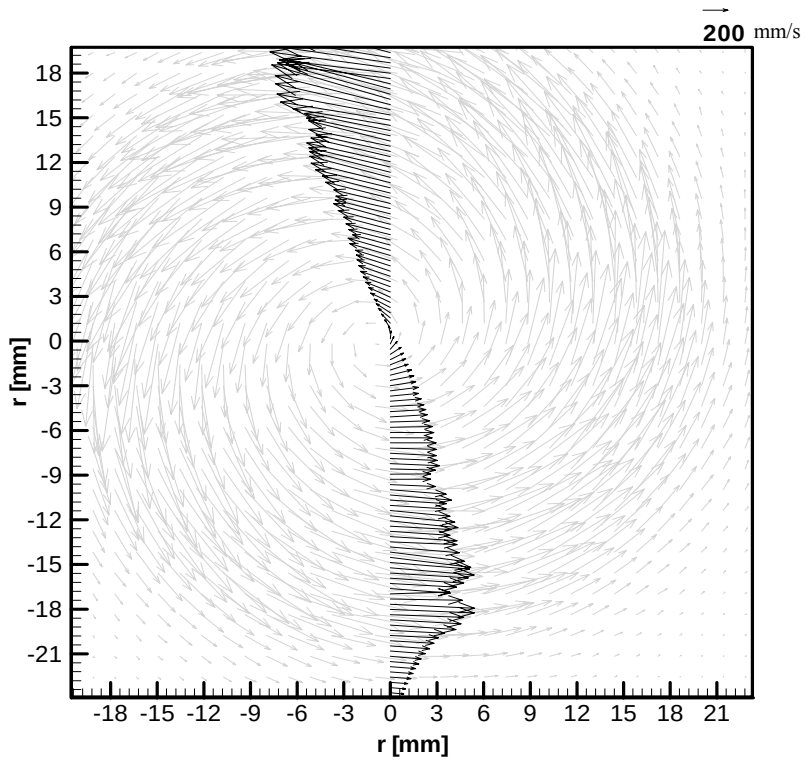

Figure 7.17: PIV vector profile of the tangential velocity of the gel along the radial axis at rotational speeds of Ω = 1200 rpm.

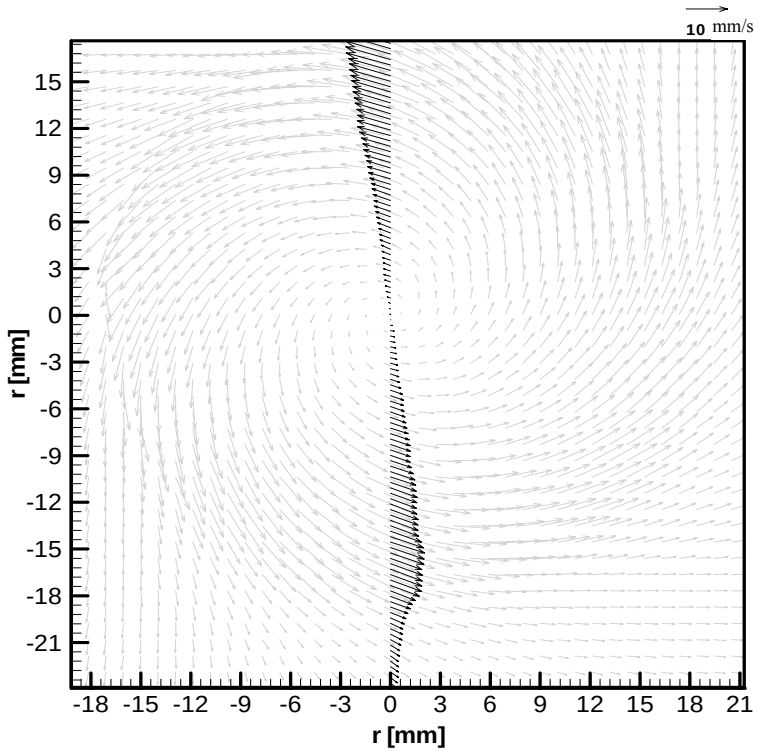

Figure 7.18: PIV vector profile of the tangential velocity of water along the radial axis at rotational speeds of Ω = 30 rpm

7.6.2 Comparison with the Model Predictions

The measurements for the gel are confined to a reduced region of the tank. The extent of the cavern can be compared to the value of $\zeta(\infty)$ for the model, which is given by:

$$\zeta(\infty) = z(\infty)\left(\frac{\Omega}{\kappa}\right)^{\frac{1}{2}} \tag{7.2}$$

For the gel, the kinematic plastic viscosity, κ, is relatively large, which causes small values of the far field, $\zeta(\infty)$, for low rotational speeds, Ω. Therefore, the field of view did not extend to infinity. Also, the confinement of the flow by the cavern for the gel did not permit the flow field itself to reach infinity, and in fact made the notion of infinity ambiguous. However, as the speed is increased the Bingham number decreased, and the cavern size increases to an extent that allows the effective far field or infinity to be reached. For water, the dimensionless location of the far field is much larger due to the small kinematic viscosity. A summary of the test parameters that determine the far field is given in Table 7.2.

Table 7.2: Summary of test parameters

Water			Gel		
Ω (rpm)	$\zeta(\infty)$	κ (m^2/sec)	Ω (rpm)	$\zeta(\infty)$	κ (m^2/sec)
30	30	0.896×10^{-6}	30	0.73	0.71×10^{-3}
60	42	0.896×10^{-6}	60	1.0	0.71×10^{-3}
1200	190	0.896×10^{-6}	1200	4.6	0.71×10^{-3}

One of the crucial assumptions adopted by von Kármán and applied in development of our numerical model is that the dimensionless velocity profiles are independent of r. The validity of this assumption was approximately confirmed for the Newtonian case (Fig. 7.7) and the case of gel at high rotational speed (Fig.7.13). Therefore, the dimensionless radial and axial velocity components acquired at only one radial location, r = 10 mm, were used for a quantitive comparison between the experimental and computational results. However, due to the confinement by the cavern, the velocity profiles for the gel at low rotational speeds were not independent of r (Figs. 7.10 and 7.11). They were also acquired at r = 10 mm to explore their deviations from the corresponding high rotational speed one.

The present boundary layer solution for a Newtonian fluid is compared to the results obtained with water in Fig. 7.19 for a rotational speed of 30 rpm. The distribution of the dimensionless radial, F, and axial, H, velocity components are plotted. Due to the limitation of the PIV system available for measurements, the tangential velocity component was not captured. When $\zeta < 1$, the PIV measurements show a higher measured radial velocity and lower axial velocity than predicted by the boundary layer solution.

The dimensionless radial and axial velocity components for the 50 wt% gel solution at 30, 60 and 1200 rpm are shown in Figs. 7.20 and 7.21, respectively; the results for water at 30 rpm and numerical curves for different values of Bingham number, i.e., B_y

= 0 and 1, are also included. An important difference is that the measured radial velocities for the gel solution peak at higher values than both the water and the numerical results near the surface of the disk, and then diminish to zero at a location closer to the disk. A second difference is that the axial velocity components were shown to reach their "infinite values" much more rapidly than they did for water and numerical results. These differences were caused by the confinement due to the presence of the yield surface which was not considered by our numerical model. Due to the confinement introduced by

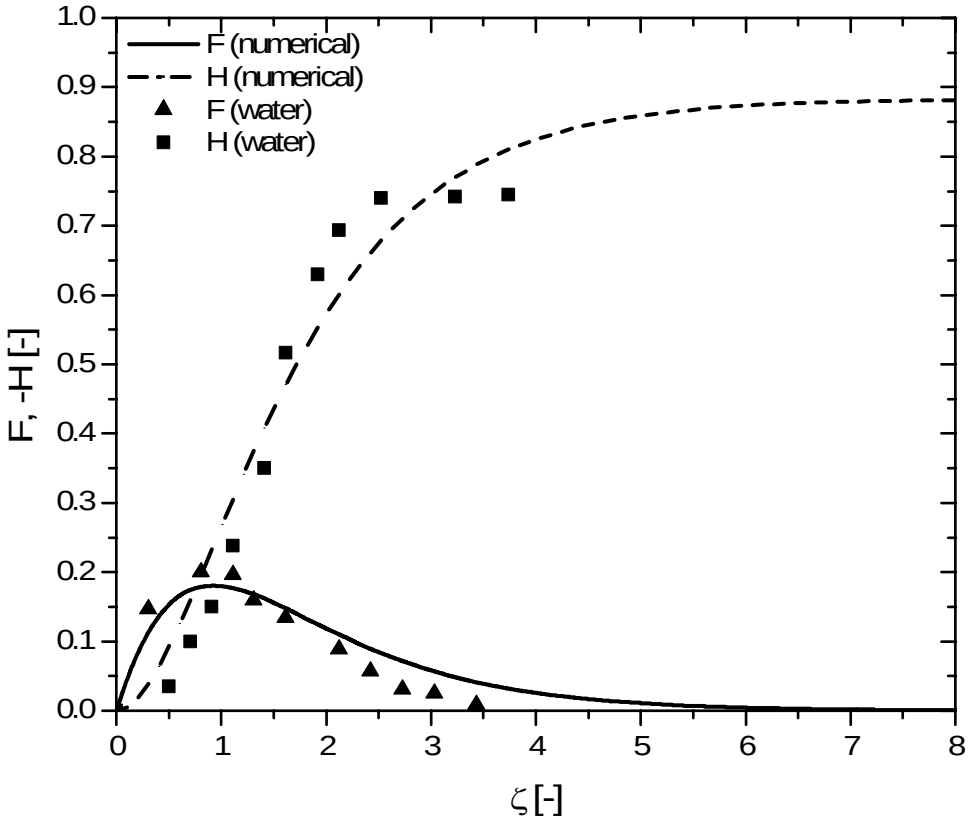

Figure 7.19: Comparison of *F* and *H* from the PIV measurements of water with numerical results of the Newtonian case

the yield surface, and possibly a pressure gradient, the velocity profiles were functions of both *r* and *z*. Therefore, significant quantitative differences were seen for the magnitude of the radial and axial velocities at all speeds compared to that of both water and the results of the numerical model.

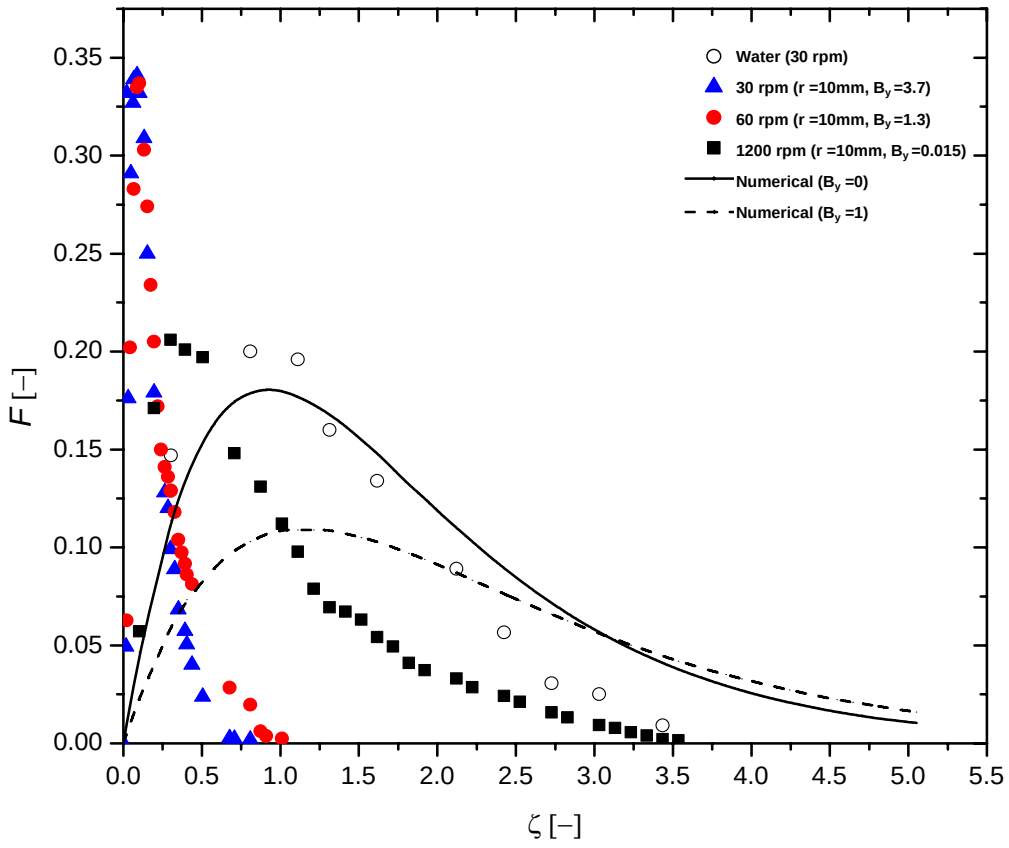

Figure 7.20: Comparison of the dimensionless radial velocity from the PIV measurements of water and the gel with numerical results for different values of Bingham number, B_y

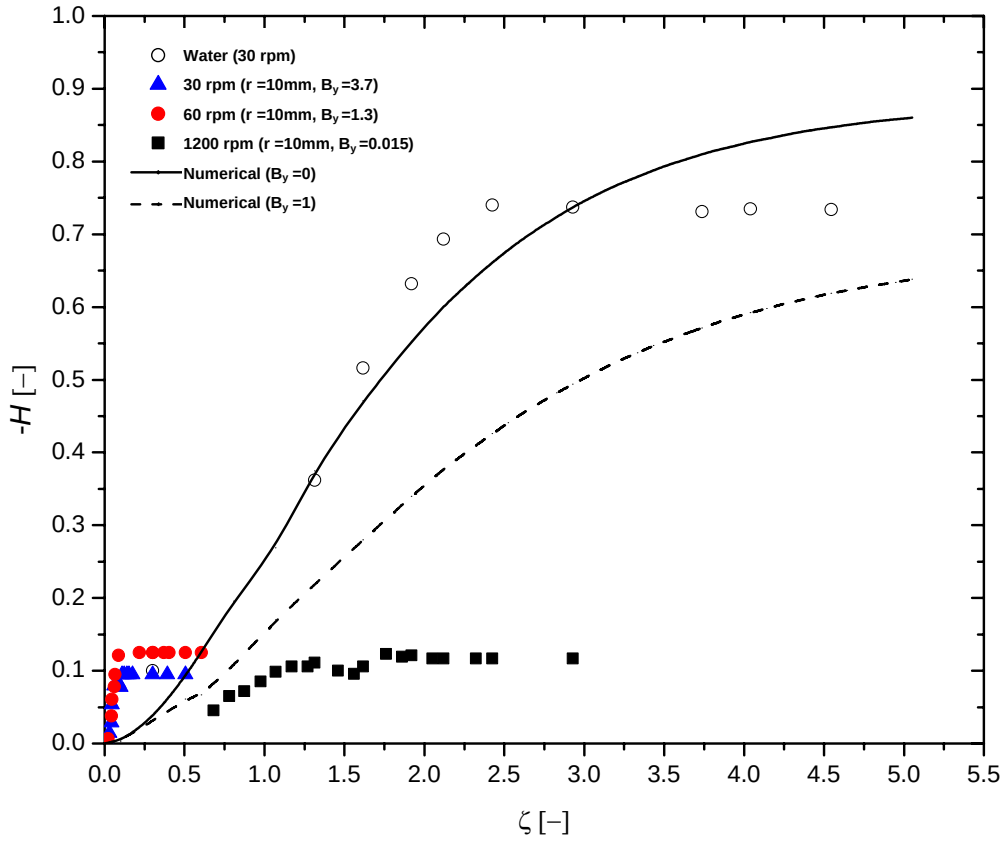

Figure 7.21: Comparison of the dimensionless axial velocity from the PIV measurements of water and the gel with numerical results for different values of Bingham number, B_y

7.7 Summary

PIV measurements were carried out for both distilled water and the 50 wt% gel in the same rotating disk apparatus that was used for the flow visualization experiments. Both the axial and radial velocity components in the (r-z) plane were measured at rotational speeds ranging from Ω = 10 to 1200 rpm. Due to experimental limitations, the

tangential velocity component was only measured close to the surface of the disk. Profiles of the dimensionless axial and radial velocity components were extracted from the measurements. The results for the water and the gel were compared at rotational speeds of 30, 60 and 1200 rpm.

When analyzing the water data for various speeds, a clear rotational speed effect can be observed. The dimensionless radial velocity profiles were observed to be approximately constant for both water and the gel at high rotational speeds, along the radial direction which validated a critical assumption of the present numerical model. For the gel at low rotational speeds this assumption was not valid. In conclusion, at relatively small Bingham numbers similar results as for water were obtained, both of which were quantitatively consistent with the results of the numerical model.

CHAPTER 8

Conclusions, Contributions and Recommendations

8.1 Introduction

Several aspects of the behavior of a Bingham plastic fluid under rotational shear which were systematically investigated in this study, are believed to be original research. Specifically, the effects of the yield stress on the velocity field, boundary layer thickness, shear deformation rate and the torque exerted on the disk were investigated for the first time.

First, a numerical simulation for laminar flow of a Bingham fluid over a rotating disk was obtained. Then, in a related physical experiment, the flow field was visualized using dye, and the velocity field was measured using PIV. The conclusions following from these numerical and laboratory investigations are presented in the following section. Thereafter, the contributions are summarized, and some recommendations for future work are presented.

8.2 Conclusions from Numerical Investigation

Numerical simulation of the flow of a Bingham fluid over a rotating disk was considered in this study. The flow field was modelled by assuming that the fluid is sheared throughout the domain. The use of this critical assumption limits the results to the sheared region, and neglects the effect of any unsheared region which might exist outside the boundary layer region. The problem was solved by using boundary-layer approximation, and applying a similarity transformation of the variables. The coupled nonlinear boundary layer equations were transformed, and the resulting system of ordinary differential equations were numerically solved using a multiple shooting method. This method was adopted to account for the extreme sensitivity to the initial condition that was encountered in solving this problem. Also, approximate dimensionless expressions for the moment coefficient on a finite disk, wall shear rate, boundary layer thickness and volumetric flow rate were obtained in terms of the Bingham number (which accounts for the yield stress effect).

From the present investigation, we conclude that the effect of the Bingham model terms in the constitutive equation for the fluid, in comparison with the Newtonian case, are:

1. To increase the thickness of the boundary-layer formed near the disk.

2. To decrease the magnitude of the radial and axial velocity components, and increase the magnitude of the tangential velocity component at any point in the fluid within the boundary-layer region.
3. To increase the dimensionless moment coefficient.
4. To increase the wall shear rate.
5. To decrease the volumetric flow rate.

8.3 Conclusions from Laboratory Investigation

The original purpose of the measurements was to obtain a set of data against which the results of the numerical investigations, described in Chapter 4, could be tested. However, it turned out that the visualization and PIV results were also useful apart from their ability to validate the numerical model. These methods provide a general picture of the flow of a Bingham fluid over a rotating disk in a tank of finite extent. In this part of the thesis, the results of rheological measurements of simulated transparent Bingham fluids, visualization of the flow of a Bingham fluid over a rotating disk, and measurement of the local velocity field were presented. The major conclusions of the laboratory investigations are summarized in the subsections below.

8.3.1 Rheological Experiments

An experimental plan to simulate waxy crude oils has been developed and implemented. Transparent oil-wax mixtures were created for a wide range of wax concentrations having properties that could be measured by a viscometer. The Bingham plastic behavior was observed at wax concentrations higher than 3 wt%. At 3 wt%, the

yield stress was found to be negligible. The oil-wax mixture that best simulated Amna waxy crude oil occurred at wax concentration of 7 wt%. At this concentration, the plastic viscosity and yield stress, including their dependence on temperature and shear rate were documented. This mixture was used for the flow visualization experiments, where only moderate transparency of the fluid was required.

To fulfill the demand of the PIV system for a higher degree of visibility, a second Bingham fluid was created and rheologically investigated. A 50 wt% diluted hair gel was found to be sufficiently transparent for the PIV measurements. It exhibited a relatively high yield stress.

8.3.2 Flow Visualization

Visualization of the flow of the simulated oil generated by a rotating disk revealed that there are two zones: an active zone or cavern around the disk of elliptic shape and a stagnant outer zone. The size of this active zone or well-sheared cavern depends on a balance between the yield stress of the fluid and the force exerted on the cavern boundary by the rotation rate of the disk. Approximate expressions for predicting cavern size have been developed in terms of the global Bingham number, B_n. As B_n decreased, the size of the cavern increased. Based on these visual observations and correlations, the size of the caverns in opaque waxy crude oils of similar rheology to the model fluid can be estimated.

8.3.3 PIV Measurements

Two-dimensional PIV measurements were performed for laminar flows of water, as well as a 50 wt% gel-water solution, over a rotating disk. For the gel, the velocity fields provide useful information about the effect of the yield stress on the flow, although only part of the area near the disk was observed. These measurements demonstrate that Bingham flows can be investigated using a typical PIV technique by careful use of a thin laser sheet and correct choice of laser pulse separation. For a boundary layer exhibiting large velocity gradients, the outlier rejected data was calculated to be small for both the Newtonian and Bingham fluid.

Unlike the PIV measurements of water, the use of diluted gel was very challenging in terms of optical access, especially at low rotational speeds. At low rotational speeds, the gel produced different trends for the velocity components than those observed with water. This may be related to the yield stress. On the other hand, the gel at relatively high rotational speeds, and the water at both low and high speeds, exhibited similar flow behavior.

Comparison between the model predictions and experimental observations, with regard to axial and radial velocity profiles was satisfactory for water. For the gel, large differences were observed, e.g., the radial component F exhibits a higher peak value than that of the water near the surface of the disk, and the axial component H reaches its infinite value much closer to the disk than does the water. These discrepancies appear to be caused by the confinement that was introduced to the flow due to presence of the yield

surface which was not considered by the numerical model. In retrospect, from a practical standpoint it would be difficult to create the conditions in a tank which would create the flow pattern considered by the numerical simulation. The presence of a tank confines the flow within a finite domain which causes a flow disturbance.

8.4 Major Contributions

The present study provides new insight into the laminar boundary layer flow of a Bingham fluid generated by a rotating disk. The major contributions of this study are summarized as follows:

1. The first numerical investigation to apply the Bingham constitutive equation to von Kármán's classical problem. This numerical model provides insight into the role of the yield stress on the performance of equipment with characterstics which are physically similar to the rotating disk system.
2. The first rheological measurements of a fluid, which successfully mimics the rheological behavior of a waxy crude oil and yet remains transparent.
3. To the author's knowledge, this is the first study to apply the PIV technique to a Bingham fluid in the specific case of the flow generated by a rotating disk. This experiment provides a good basis for future work using the PIV technique to observe the flow behavior of a Bingham fluid in fluid handling equipment, such as a centrifugal pump.

8.5 Recommendations for Future Work

On the basis of the present study and our current understanding of the flow of a Bingham fluid over a rotating disk, the following recommendations are made with respect to future work:

1. According to the general Bingham model, the shear stress in the region near the yield surface is below the yield stress. As a result, the fluid in this region cannot flow. For such a material, a radially outward motion is physically impossible. This contradiction can be accounted for by the introduction of the bi-viscosity model, which assumes that the material behaves as a Newtonian fluid with very large viscosity until the critical yield stress is exceeded. Above the yield stress, the apparent viscosity of the material decreases. In this regard, modeling of the flow of a Bingham fluid over a rotating disk would have benefited from an investigation which employed the bi-viscosity model. However, this may require a different numerical approach.
2. The PIV results presented in this thesis should be considered as preliminary measurements. A more thorough experimental investigation would need to address the limitations associated with the current velocity measurements. For example, in order to get a complete picture of the flow patterns of a Bingham fluid, particularly at low rotational speeds, it would be desirable to perform measurements of the velocity field throughout the region below the disk. Further investigation of the effects of the wall on the PIV measurements would also be

useful in verifying the infinite medium assumption. It is recommended that a much larger tank be used with the current disk size.

3. Future experimental and/or numerical investigations into the effect of turbulence on a Bingham fluid flowing over a rotating disk will also aid in understanding the behavior of such material under high shear.

REFERENCES

Acrivos, A., Shah, J. and Petersen, E. 1960 On the Flow of a Non-Newtonian Liquid on a Rotating Disk. *J. of Applied Physics*. **31(6)**, 963-968.

Andersson, H., De Korte, E. and Meland, R. 2001 Flow of a Power-Law Fluid over a Rotating Disk Revisited. *Fluid Dynamics Research*. **28**, 75-88.

Al-Fariss, T., Jang, K., Ozbelge, H. and Ghasem, N. 1993 A New Correlation for the Viscosity of Waxy Oils. *J. Pet. Sci. Eng.* **9**, 139-144.

Balaram M. and Luthra B. 1973 A Numerical Study of Rotationally Symmetric Flow of Second-Order Fluid. 685-687.

Barry, E. G. 1971 Pumping Non-Newtonian Waxy Crude Oils. *J. Inst. Pet.*, **57(554)** 74-85.

Batchelor, G. K. 1951 Note on a Class of Solutions of the Navier-Stokes Equations Representing Steady Rotationally - Symmetric Flow. *Quart. J. Mech. Appl. Math*. **4**, 29-41.

Bercovier, M. and Engelman M. 1980 A Finite Element Method for the Incompressible Non-Newtonian Flows. *J. Comp. Phys*. **36**, 313-326.

Berman, N. S. and Pasch, M. A. 1986 Laser Doppler Velocity Measurements for Dilute Polymer Solutions in the Laminar Boundary Layer of a Rotating Disk. *J. of Rheology*, **30(3)**, 441-458.

Bingham, E. C. and Green, H. 1919 Plastic Material and not a Viscous Liquid; The Measurement of its Mobility and yield value. *Proc. Amer. Soc. Test Mater*. **20(2)**, 640-675.

Bird, R. B., Stewart, W. E. and Lightfoot, E. N. 2002 Transport Phenomena, **2nd** Edition, John Wiley & Sons, Inc., New York.

Bird, R. B. Dai, G. C. and Yarusso, B. Y. 1982 The Rheology and Flow of Viscoplastic Materials, *Rev. Chem. Eng.* **1**, 1.

Bodewadt, U. T. 1940 Die Drehstromunguber Festem Grund. *Z. Angew. Math. Mech*. **20**, 241–253.

Brian G. H. 1986 Film Flow on a Rotating Disk. *Phys. of Fluids.* **29(11)**, 3522-3529.

Burgess, S. L. and Wilson, SDR 1996 Spin-Coating of a Viscoplastic Material. *Phys. Fluids*. **8**, 2291–2297.

Burson, J. H., Keng, E. Y. H. and Orr, G. 1967 Particle Dynamics in Centrifugal Fields, *Powder Technology*. **1**,305-315.

Cheng Chang, Boger, D. V., and Nguyen, D., 1998 The Yielding of Waxy Crude Oils. *Ind. Eng. Chem. Res*., **37**, 1551-1559.

Cochran, W. G. 1934 The Flow Due to a Rotating Disk. *Cambridge Philos. Soc. Proc.* **30**, 365-375.

Conover, R. A. 1968 Laminar Flow Between a Rotating Disk and a Parallel Stationary Wall With and Without Radial Inflow. *Transactions of the ASME, J. Basic Engng*.

Daily, J. W. and Nece, R. E. 1960 Chamber Dimension Effects on Induced Flow and Frictional Resistance of Enclosed Rotating Disks. *J. Basic Engng*. **82**, 217-232.

Davenport, T. C. and Somper, R. S. H., 1971 The Yield Value and Breakdown of Crude Oil Gels. *J. Inst. Pet*., **55(554)**, 86-105.

Denier, J. P. and Hewitt, R. E. 2004 Asymptotic matching constraints for a boundary-layer flow of a power-law fluid. *J. Fluid Mech*. **518**, 261–279.

Drain, L. E. 1972 The Laser Doppler Technique, John Wiley & Sons, Inc., New York.

El-Eman N., Bayoumi A., El-Gamal I. And Abu-zied A. 1993 A Study on the Suitable Techniques for Improving the Flow Properties of the Egyptian Waxy Crude Oils. *Revue de L'insitut fancais du petrole*. **48(4)**, 371-382.

Durst, F., Melling N. and Whitelaw, J. H. 1981 Principle and Practice of Laser- Doppler Anemometry, (2^{nd} ed.) Academic Press.

Elson T. P., Cheesman D. J. and Nienow A. W 1986 X-Ray Studies of Cavern Sizes and Mixing Performance with Fluids Possessing a Yield Stress. *Chemical Engineering Science*. **41(10)**, 2555-2562.

Emslie A. G., Bonner F. T. and Peck L. G. 1958 Flow of a Viscous Liquid on a Rotating Disk. *J. of Applied Physics*. **29**, 858-862.

Goldstein, S., 1935 On the Resistance to the Rotation of a Disc Immersed in a Fluid. *Proc. Cambridge Philos. Soc*. **31**, 232–241.

Gregory, N., Stuart, J. T. and Walker, W. S. 1955 On the Stability of Three-Dimensional Boundary Layers with Application to the Flow Due to a Rotating Disk. *Math. Phys. Sci.* **248**, 155-199.

Greif, R. and Paterson, J. 1973 Mass Transfer to a Rotating Disk in a Non-Newtonian Fluid. *Phys. Fluids*. **16**, 1816-1817.

Hansford, G. and Litt, M. 1968 Mass Transport from a Rotating Disk into Power-Law Liquids. *Chem. Eng. Sci.* **23**, 849-864.

Hart D. P. 2000 PIV Error Correction, *Exp. in Fluids,* **29**, 13-22.

HM 40, 2004 Guidelines for the Crude Oil Washing of Ships, Tanks and the Heating of Crude Oil Being Transported by Sea. Energy Institute, Colchester, UK.

Hydraulic Institute Standards, 1975 **13 ed**., 100-105.

Irani, C., and Zajac, J. 1982 Handling of High Pour Point West African Crude Oils. *J. Pet. Technol.* **34**, 289-298.

Jenekhe S. A. and Schuldt S. B. 1985 Flow and Film Thickness of Bingham Plastic Liquids on a Rotating Disk. *Chem. Eng. Commun*. **33**, 135-147**.**

Kármán, Th.v. 1921 Über laminare und turbolente Reibng. *Zeitschrift für Angew. Math. Mech.* **1**, 233-252.

Kawase Y., and Ulbrecht J. 1983 Heat and Mass Transfer in Non-Newtonian Fluid Flow with Power Function Velocity Profiles. *Can. J. Chem. Eng*. **61**, 791-798.

Khan H., Diluwar S., Nautiyal P.and Srivastava P. 1993 New Methods Determine Pour Point more Accurately than ASTM D-97 *Oil and Gas J.*, **1**, 74-76.

Keane R.D., Adrian R. J., and Zhang Y. 1995 Super-Resolution Particle Image Velocimetry. *Meas. Sci. Technol.* **2**,1202-1215.

Kang, H. S., Choi, H. and Yoo, J. Y. 1998 On the Modification of the Near-Wall Coherent Structure in a Three-Dimensional Turbulent Boundary Layer on a Free Rotating Disk. *Phys. of Fluids.* **10(9)**, 2315-2322.

Kirsanov, E. A. and Remizov, S. V. 1999 Application of the Casson Model to Thixotropic Waxy Crude Oil. *Rheologica Acta.* **38(2)**, 172 – 176.

Lance, G. N. and Rogers, M. H. 1961 The axially Symmetric Flow of a Viscous Fluid Between Two Infinite Rotating disks. *Proc. Roy. Soc. Lond*. **A 266**, 109-121.

Li, W. –G., 2000 Effects of Viscosity of Fluids on Centrifugal Pump Performance and Flow Pattern in the Impeller. *Int. J. Heat and Fluid Flow*. **21**. 207-212.

Lorenzo Fusi, 2003 On the Stationary Flow of a Waxy Crude Oil with Deposition Mechanisms. *Nonlinear Analysis*, **53**, 507-526.

Lovell P. F. and Seitzer W. H. 1981 Some Flow Characteristics of Utah Shale Oils. *Proc., 12th Oil Shale Symposium*. Colorado School of Mines Press, Golden. 213-220.

Lutz, M., Denk, V., Wichterle, V., Sobolik, 1996 Electrodiffusional Flow Diagnostics in a Centrifugal Pump. *Fourth European Symposium on Electrochemical Engineering, Prague*, 28-30.

Marsden S., Kiyoshi Ishimoto and Lidian Chen, 1988 Slurries and Emulsions of Waxy and Heavy Crude Oils for Pipeline Transportation of Crude Oil. *Colloids and Surfaces*. **29**, 133-146.

Matsumoto S. and Takashima Y. 1982 Film Thickness of a Bingham Liquid on a Rotating Disk. *Ind. Eng. Chem. Fundam*. **21**, 198-202.

Mellor, G. L., Chapple, P. J. and Stokes, V. K. 1968 On the Flow Between a Rotating and a Stationary Disk. *J. Fluid Mech*. **31**, 95-112.

Millsaps K and Pohlhausen K. 1952 Heat Transfer by Laminar Flow from a Rotating Plate, *J. Aeronautical Science*. **19**,120-126.

Mishra P. and Prakash Singh. 1978 Mass Transfer from Rotating Disk to Non-Newtonian Fluids. *Chemical Engineering Science*. **33**, 1463-1470.

Mitschka, P. and Ulbricht, J. 1965 *Collect. Czech. Chem. Commun*. **30**, 2511.

Mueller, T.J., and Batill, S.M. 1982 Experimental Studies of Separation on a Two-Dimensional Airfoil at Low Reynolds Numbers. *AIAA J.*. **20(4),** 456-463.

Neil, S. and Mark, A., 1986 Laser Doppler Velocity Measurements for Dilute Polymer Solutions in the Laminar Boundary Layer of a Rotating Disk. *J. of Rheology*. **30(3)**, 441-458.

Nguyen, Q. D. and Boger D. V. 1992 Measuring the Flow Properties of Yield Stress Fluids. *Annu. Rev. Fluid Mech*. **24**, 47–88.

O'Donovan, E. J. and Tanner R. I. 1984 Numerical study of the Bingham squeeze film problem. *J. Non-Newtonian Fluid Mech.* **15**, 75-83.

Owen, J. M. and Rogers, R. H. 1989 Flow and Heat Transfer in Rotating Disc Systems: Vol. 1, Rotor-stator systems. *Research Studies Press*, John Wiley & Sons, Inc., New York.

Ostrach and Thornton, 1958 Compressible Laminar Flow and Heat Transfer about a Rotating Disk, *NACA Technical Note 3420*.

Papanastasiou, T.C. 1987 Flow of Materials with Yield. *J. Rheol.* **31**, 385-404.

Pedersen, N., Larsen, P. S. and Jacobsen, C. B. 2003 Flow in a Centrifugal Pump Impeller at Design and Off-design Conditions-Part I: Particle Image Velocimetry (PIV) and Laser Doppler Velocimetry (LDV) Measurements. *J. of Fluids Engineering*, **125**, 61-72.

Prasad, A. and Adrian, R. 1993 Stereoscopic Particle Image Velocimetry Applied to Liquid Flows *Exp. Fluids* **15** 49–60.

Rashaida A. A., Bergstrom D. J. and Sumner R.J. 2005 Mass Transfer from a Rotating Disk to a Bingham Fluid. *Accepted for publication in the J. of Applied Mechanics.*

Reynolds, O. 1883 An Experimental Investigation of the Circumstances which Determine whether the Motion of Water shall be Direct or Sinuous, and of the Law of Resistance in Parallel Channels. *Royal Society, Phil. Trans*. **174**, 935-982.

Riahi, A. and Hill, P.G. 1994 Turbulent Swirling Flow in short Cylinder Chambers. *ASME Trans., J. Fluids Engng.* **115**, 444-451.

Rojas, G., 1977 Rheological Behavior of Extra-Heavy Crude Oils from the Orinoco Oil Belt, Venezuela. Inc. *The Oil Sands Of Canada-Venezuela*, 284-302.

Ronningsen, H. P. 1992 Rheological Behavior of Gelled, Waxy North Sea Crude Oils. *J. Pet. Sci. Eng*., **7**, 177-213.

Schlichting H. 1979 Boundary Layer Theory. **7th ed**. New York: McGraw-Hill.

Skelland, A. H. P. 1967 Non-Newtonian Flow and Heat Transfer. John Wiley & Sons, Inc., New York.

Shinneeb A-M, Balachandar, R. and Bugg, J.D. 2004 PIV Measurements in Shallow Water Jets, *Canadian Society of Civil Engineering Conference*, Saskatoon, June 2-5.

Sirivat, A., Rajagopal, K. and Szeri, A. 1988 An Experimental Investigation of the Flow of non-Newtonian Fluids Between Rotating Disks. *J. Fluid Mech*. **186**, 243-256.

Soo, S. L. 1958 Laminar Flow over an Enclosed Rotating Disk. *Trans. ASME*. **80**, 287-296.

Solomon J., Elson T. P., Nienow A. W. and Pace G. W. 1981 Cavern Sizes in Agitated Fluids With a Yield Stress. *Chem. Eng. Commun.* **11**, 143-164.

Sparrow, E. M., Gregg, J. L. 1959 A Theory of Rotating Condensation. *J. Heat Transfer.* **81**.113-120.

Sparrow, E. M., Gregg, J. L. 1960 Mass Transfer, Flow, and Heat Transfer about a Rotating Disk," *J Heat Trans., Trans. ASME*. **82**, 294-302.

Stern, F., Muste, M., Beninati, M.L., and Eichinger W.E. 1999 Summary of Experimental Uncertainty Assessment Methodology with Example. *IHR Technical Report No.* **406**, University of Iowa, Iowa City, IA.

Stewartson, K. 1953 On the Flow Between Two Rotating Coaxial Disks. *Proc. Camb. Phil. Soc.* **49**, 333-341.

Van Wazer, J. R., Lyons, J. W., Kim, K. Y. and Colwell, R. E. 1963 Viscosity and Flow Measurement. John Wiley & Sons, Inc., New York.

Wagner C. 1948 Heat Transfer from a Rotating Disk to Ambient Air. *J. Applied Physics,* **19**, 837-839.

Walker, C. I. and Goulas, A. 1984 Performance Characteristics of Centrifugal Pumps When Handling Non-Newtonian Homogeneous Slurries. *Proc. Inst. Mech. Engrs.*, **198 A (1)**, 41-49.

Wardaugh, L. T. and Boger, D. V. 1987 Measurement of the Unique Flow Properties of Waxy Crude Oils. *Chem. Eng. Res. Des*. **65**, 74-83.

Wardaugh, L. T. and Boger, D. V. 1991 The Flow Characteristics of Waxy Crude Oils-Application to Pipeline Design. *AIChE J.*, **37(6)**, 871-885.

Werle, H.1973 Hydrodynamic Flow and Visualization. *Annual Rev. Fluid Mech*. **5**. 361–382.

Westerweel. J. 1997 Fundamentals of Digital Particle Image Velocimetry," *Meas. Sci. Technol.* **8**, 1379-1392.

Wichterle K. and Wein O. 1981 Threshold of Mixing of Non-Newtonian Liquids. *International Chemical Engineering*. **21(1)**, 116-120.

Wichterle, K., Sobolik, V., Lutz, M. and Denk, V., 1996 *Chem. Engng Sci.* **51(23)**, 5227-5228.

Wichterle K. and Mitschka, P. 1998 Relative Shear Deformation of Non-Newtonian Liquids in Impeller Induced Flow. *Collect. Czech. Chem. Commun*., **63**, 2092-2102.

Wu, X. and Squires, K.D. 2000 Prediction and Investigation of the Turbulent Flow over a Rotating Disk, *J. Fluid Mech*. **418**, 231-264.

Xu J., Tipman R., Gillies R. and Shook C. 2002 Centrifugal Pump Performance with Newtonian and Non-Newtonian Slurries, *Proc. Hydrotransport 15, BHR Group, Cranfield, U.K.,* 693-710.

Yamane, T., Clarke, H., Asztalos, B., Nishida, M., and Kobayashi, T. 1999 Flow Visualization Measurement for Shear Velocity Distribution in the Impeller-Casing Gap of a Centrifugal Blood Pump. *JSME International j.*, *Series C*, **42(3)**, 621-627.

Zhou, M., Garner, C. P. and Reeves, M. 1996 Numerical Modeling and Particle Image Velocimetry Measurement of the Laminar Flow Field Induced by an Enclosed Rotating Disc. *Int. j. for Numerical Methods in Fluids*, **22**, 283-296.

APPENDIX A

Reduction of the Transport Equations of Mass and Momentum to a Set of ODEs

In this Appendix, a step by step algebraic manipulation for casting the final form of the ordinary differential equations, ODEs, is presented. It is helpful to understand the development of the model.

Substitutions of the equations (3.12 a, b, c, d) for velocity, equations (3.26) and (3.27) for the shear stress components, and equation (3.28) for the ratio B_y, into equations (3.7) to (3.9) are as follows:

Continuity Equation

$$\frac{\partial (r\Omega F)}{\partial r} + \frac{r\Omega F}{r} + \frac{\partial (\sqrt{\kappa\Omega}\ H)}{\partial z} = 0 \tag{A.1}$$

$$\Omega F + \Omega F + \frac{\partial (\sqrt{\kappa\Omega}\ H)}{\partial \zeta}\frac{\partial \zeta}{\partial z} = 0 \tag{A.2}$$

$$2\Omega F + \sqrt{\kappa\Omega}\frac{\partial H}{\partial \zeta}\sqrt{\frac{\Omega}{\kappa}} = 0 \tag{A.3}$$

$$2F + \frac{\partial H}{\partial \zeta} = 0 \tag{A.4}$$

$$2F + H' = 0 \tag{A.5}$$

Momentum Equations

r-wise

$$r\Omega F\frac{\partial (r\Omega F)}{\partial r} + (\sqrt{\Omega\kappa}\,H)\frac{\partial (r\Omega F)}{\partial z} - \frac{(r\Omega F)^2}{r} = \frac{1}{\rho}\frac{\partial}{\partial z}\left[\mu_p + \frac{\tau_y}{\left[\left(\frac{\partial v_r}{\partial z}\right)^2 + \left(\frac{\partial v_\phi}{\partial z}\right)^2\right]^{\frac{1}{2}}}\right]\left(\frac{\partial v_r}{\partial z}\right) \tag{A.6}$$

$$r\Omega^2 F^2 - r\Omega^2 G^2 + (\sqrt{\Omega\kappa}\,H)\frac{\partial (r\Omega F)}{\partial \zeta}\frac{\partial \zeta}{\partial z} = \frac{1}{\rho}\frac{\partial}{\partial z}\left[\mu_p + \frac{\tau_y}{\left[\frac{\partial^2}{\partial z}(r\Omega F)^2 + \frac{\partial}{\partial z}(r\Omega G)^2\right]^{\frac{1}{2}}}\right]\frac{\partial}{\partial z}(r\Omega F) \tag{A.7}$$

$$r\Omega^2\left(F^2-G^2\right)+(\sqrt{\Omega\kappa})r\Omega H\sqrt{\frac{\Omega}{\kappa}}\frac{\partial F}{\partial\zeta}=$$

$$\frac{1}{\rho}\frac{\partial}{\partial z}\left\{\left[\mu_p+\frac{2B_y\left(\mu\rho\Omega^3r^2\right)^{\frac{1}{2}}}{\left[\left(\frac{\partial}{\partial\zeta}(r\Omega F)\frac{\partial\zeta}{\partial z}\right)^2+\left(\frac{\partial}{\partial\zeta}(r\Omega G)\frac{\partial\zeta}{\partial z}\right)^2\right]}\right]\frac{\partial}{\partial\zeta}(r\Omega F)\frac{\partial\zeta}{\partial z}\right\} \tag{A.8}$$

$$r\Omega^2\left(F^2-G^2\right)+(\sqrt{\Omega\kappa})r\Omega^2H\sqrt{\frac{\Omega}{\kappa}}\frac{\partial F}{\partial\zeta}=$$

$$\frac{1}{\rho}\frac{\partial}{\partial z}\left\{\left[\mu_p+\frac{2B_y\rho\Omega r(\kappa\Omega)^{\frac{1}{2}}}{\left[\left(\frac{\Omega rF'}{\left(\frac{\kappa}{\Omega}\right)^{\frac{1}{2}}}\right)^2+\left(\frac{\Omega rG'}{\left(\frac{\kappa}{\Omega}\right)^{\frac{1}{2}}}\right)^2\right]^{\frac{1}{2}}}\right]\frac{\Omega rF'}{\left(\frac{\kappa}{\Omega}\right)^{\frac{1}{2}}}\right\} \tag{A.9}$$

$$r\Omega^2\left(F^2-G^2\right)+(\sqrt{\Omega\kappa})r\Omega^2H\sqrt{\frac{\Omega}{\kappa}}\frac{\partial F}{\partial\zeta}=$$

$$\frac{1}{\rho}\frac{\partial}{\partial z}\left\{\left[\mu_p+\frac{2B_y\rho\Omega r(\kappa\Omega)^{\frac{1}{2}}}{\sqrt{\Omega^2r^2}\left(\frac{\Omega}{\kappa}\right)^{\frac{1}{2}}\left[F'^2+G'^2\right]^{\frac{1}{2}}}\right]\frac{\Omega rF'}{\left(\frac{\kappa}{\Omega}\right)^{\frac{1}{2}}}\right\} \tag{A.10}$$

$$r\Omega^2\left(F^2-G^2\right)+(\sqrt{\Omega\kappa})r\Omega^2 H\sqrt{\frac{\Omega}{\kappa}}\frac{\partial F}{\partial\zeta}=$$

$$\frac{1}{\rho}\frac{\partial}{\partial z}\left\{\left[1+\frac{2B_y\rho\kappa}{\left[F'^2+G'^2\right]^{\frac{1}{2}}}\right]\frac{\mu\Omega rF'}{\left(\frac{\kappa}{\Omega}\right)^{\frac{1}{2}}}\right\} \tag{A.11}$$

$$r\Omega^2\left(F^2-G^2\right)+(\sqrt{\Omega\kappa})r\Omega^2 H\sqrt{\frac{\Omega}{\kappa}}\frac{\partial F}{\partial\zeta}=$$

$$\frac{\partial}{\partial\zeta}\left\{\left[1+\frac{2B_y}{\left[F'^2+G'^2\right]^{\frac{1}{2}}}\right]\frac{\mu\Omega rF'}{\frac{\mu}{\kappa}\left(\frac{\kappa}{\Omega}\right)^{\frac{1}{2}}}\right\}\frac{\partial\zeta}{\partial z} \tag{A.12}$$

$$r\Omega^2\left(F^2-G^2\right)+(\sqrt{\Omega\kappa})r\Omega^2 H\sqrt{\frac{\Omega}{\kappa}}\frac{\partial F}{\partial\zeta}=$$

$$\left\{\left[1+\frac{2B_y}{\left[F'^2+G'^2\right]^{\frac{1}{2}}}\right]\frac{\Omega rF''}{\frac{1}{\kappa}}\left(\frac{\Omega}{\kappa}\right)^{\frac{1}{2}}\right\}\left(\frac{\Omega}{\kappa}\right)^{\frac{1}{2}} \tag{A.13}$$

$$r\Omega^2\left(F^2-G^2\right)+(\sqrt{\Omega\kappa})r\Omega^2 H\sqrt{\frac{\Omega}{\kappa}}\frac{\partial F}{\partial\zeta}=$$

$$\left\{\left[1+\frac{2B_y}{\left[F'^2+G'^2\right]^{\frac{1}{2}}}\right]\Omega rF''\frac{\Omega}{\kappa}\kappa\right\} \tag{A.14}$$

$$r\Omega^2\left(F^2-G^2\right)+r\Omega^2 HF'=r\Omega^2 F''\left[1+\frac{2B_y}{\left[F'^2+G'^2\right]^{\frac{1}{2}}}\right] \tag{A.15}$$

$$F^2-G^2+HF'-F''-\frac{2B_y\left(F''-\dfrac{F'\left(G'G''+F'F''\right)}{F'^2+G'^2}\right)}{\left(F'^2+G'^2\right)^{\frac{1}{2}}}=0 \tag{A.16}$$

$$\begin{aligned}F''=&\left[F^2\left(F'^2+G'^2\right)^{\frac{1}{2}}F'^2+F^2\left(F'^2+G'^2\right)^{\frac{1}{2}}G'^2-G^2\left(F'^2+G'^2\right)^{\frac{1}{2}}F'^2+2B_yG'F'G''\right.\\&\left.-G^2\left(F'^2+G'^2\right)^{\frac{1}{2}}G'^2+F'^3H\left(F'^2+G'^2\right)^{\frac{1}{2}}+F'H\left(F'^2+G'^2\right)^{\frac{1}{2}}G'^2\right]\\&\left(F^2\left(F'^2+G'^2\right)^{\frac{1}{2}}F'^2+F^2\left(F'^2+G'^2\right)^{\frac{1}{2}}G'^2+2B_yG'^2\right)^{-1}\end{aligned} \tag{A.17}$$

<u>*ϕ-wise* (Eq. 3.9, p.36)</u>

$$\begin{aligned}r\Omega F\frac{\partial(r\Omega G)}{\partial r}+(\sqrt{\Omega\kappa}\,H)\frac{\partial(r\Omega G)}{\partial z}-\frac{(r^2\Omega^2FG)}{r}=&\\\frac{1}{\rho}\frac{\partial}{\partial z}\left[\mu_p+\frac{\tau_y}{\left[\left(\dfrac{\partial v_r}{\partial z}\right)^2+\left(\dfrac{\partial v_\phi}{\partial z}\right)^2\right]^{\frac{1}{2}}}\right]&\left(\frac{\partial v_\phi}{\partial z}\right)\end{aligned} \tag{A.18}$$

$$r\Omega^2 FG + r\Omega^2 FG + (\sqrt{\Omega\kappa}\,H)\frac{\partial(r\Omega G)}{\partial\zeta}\frac{\partial\zeta}{\partial z} = \frac{1}{\rho}\frac{\partial}{\partial z}\left[\mu_p + \frac{\tau_y}{\left[\frac{\partial^2}{\partial z}(r\Omega F)^2 + \frac{\partial}{\partial z}(r\Omega G)^2\right]^{\frac{1}{2}}}\right]\frac{\partial}{\partial z}(r\Omega G) \tag{A.19}$$

$$2r\Omega^2 FG + (\sqrt{\Omega\kappa})r\Omega H\sqrt{\frac{\Omega}{\kappa}}\frac{\partial G}{\partial\zeta} = \frac{1}{\rho}\frac{\partial}{\partial z}\left\{\left[\mu_p + \frac{2B_y\left(\mu\rho\Omega^3 r^2\right)^{\frac{1}{2}}}{\left[\left(\frac{\partial}{\partial\zeta}(r\Omega F)\frac{\partial\zeta}{\partial z}\right)^2 + \left(\frac{\partial}{\partial\zeta}(r\Omega G)\frac{\partial\zeta}{\partial z}\right)^2\right]}\right]\frac{\partial}{\partial\zeta}(r\Omega G)\frac{\partial\zeta}{\partial z}\right\} \tag{A.19}$$

$$2r\Omega^2 FG + r\Omega^2 H\frac{\partial G}{\partial\zeta} = \frac{1}{\rho}\frac{\partial}{\partial z}\left\{\left[\mu_p + \frac{2B_y\rho\Omega r(\kappa\Omega)^{\frac{1}{2}}}{\left[\left(\frac{\Omega rF'}{\left(\frac{\kappa}{\Omega}\right)^{\frac{1}{2}}}\right)^2 + \left(\frac{\Omega rG'}{\left(\frac{\kappa}{\Omega}\right)^{\frac{1}{2}}}\right)^2\right]^{\frac{1}{2}}}\right]\frac{\Omega rG'}{\left(\frac{\kappa}{\Omega}\right)^{\frac{1}{2}}}\right\} \tag{A.20}$$

$$2r\Omega^2 FG + r\Omega^2 H\frac{\partial G}{\partial \zeta} =$$

$$\frac{1}{\rho}\frac{\partial}{\partial z}\left\{\left[\mu_p + \frac{2B_y\rho\Omega r(\kappa\Omega)^{\frac{1}{2}}}{\sqrt{\Omega^2 r^2}\left(\frac{\Omega}{\kappa}\right)^{\frac{1}{2}}\left[F'^2 + G'^2\right]^{\frac{1}{2}}}\right]\frac{\Omega r G'}{\left(\frac{\kappa}{\Omega}\right)^{\frac{1}{2}}}\right\} \tag{A.21}$$

$$2r\Omega^2 FG + r\Omega^2 H\frac{\partial G}{\partial \zeta} =$$

$$\frac{\partial}{\partial z}\left\{\left[1 + \frac{2B_y}{\left[F'^2 + G'^2\right]^{\frac{1}{2}}}\right]\frac{\mu\Omega r G'}{\frac{\mu}{\kappa}\left(\frac{\kappa}{\Omega}\right)^{\frac{1}{2}}}\right\}\frac{\partial\zeta}{\partial z} \tag{A.22}$$

$$2r\Omega^2 FG + r\Omega^2 H\frac{\partial G}{\partial \zeta} =$$

$$\left\{\left[1 + \frac{2B_y}{\left[F'^2 + G'^2\right]^{\frac{1}{2}}}\right]\frac{\Omega r G''}{\frac{1}{\kappa}}\left(\frac{\Omega}{\kappa}\right)^{\frac{1}{2}}\right\}\left(\frac{\Omega}{\kappa}\right)^{\frac{1}{2}} \tag{A.23}$$

$$2r\Omega^2 FG + r\Omega^2 H\frac{\partial G}{\partial \zeta} =$$

$$\left\{\left[1 + \frac{2B_y}{\left[F'^2 + G'^2\right]^{\frac{1}{2}}}\right]\Omega^2 r G''\right\} \tag{A.24}$$

$$2r\Omega^2 FG + r\Omega^2 HG' = r\Omega^2 G''\left[1 + \frac{2B_y}{\left[F'^2 + G'^2\right]^{\frac{1}{2}}}\right] \tag{A.25}$$

$$2FG + HG' = G''\left[1 + \frac{2B_y}{\left[F'^2 + G'^2\right]^{\frac{1}{2}}}\right] \tag{A.26}$$

$$2FG + HG' - G'' - \frac{2B_y\left(G'' - \frac{G'\left(G'G'' + F'F''\right)}{F'^2 + G'^2}\right)}{\left(F'^2 + G'^2\right)^{\frac{1}{2}}} = 0 \tag{A.27}$$

$$G'' = \left[2FG\left(F'^2 + G'^2\right)^{\frac{1}{2}} F'^2 + 2FG\left(F'^2 + G'^2\right)^{\frac{1}{2}} G'^2 + G'H\left(F'^2 + G'^2\right)^{\frac{1}{2}} F'^2 + G'^3 H\left(F'^2 + G'^2\right)^{\frac{1}{2}} + 2B_y F'G'F''\right]$$

$$\left(F^2\left(F'^2 + G'^2\right)^{\frac{1}{2}} F'^2 + \left(F'^2 + G'^2\right)^{\frac{1}{2}} G'^2 + 2B_y F'^2\right)^{-1} \tag{A.28}$$

Now we have to eliminate the second derivatives in the right hand side of equations (A.17) and (A.28), since we derive a single second order variable for each equation. This can be done by substituting the value of F'' and G'' back into equations (A.27) and (A.16), respectively. Thus,

$$F'' = \Big[2F^2 B_y F'^2 - G'^2 G^2 \left(F'^2 + G'^2\right)^{\frac{1}{2}} + G'^2 F' H \left(F'^2 + G'^2\right)^{\frac{1}{2}} - G^2 F'^2 \left(F'^2 + G'^2\right)^{\frac{1}{2}} + 2B_y G'^2 F' H + F^2 G'^2 \left(F'^2 + G'^2\right)^{\frac{1}{2}} + 4B_y F F' G G' + F'^3 H \left(F'^2 + G'^2\right)^{\frac{1}{2}} + F^2 F'^2 \left(F'^2 + G'^2\right)^{\frac{1}{2}} + 2B_y F'^3 H - 2B_y F'^2 G^2 \Big] \left(2B_y G'^2 + \left(F'^2 + G'^2\right)^{\frac{1}{2}} F'^2 + \left(F'^2 + G'^2\right)^{\frac{1}{2}} G'^2 + 2B_y F'^2 \right)^{-1} \tag{A.29}$$

$$G'' = \Big[2B_y G'^3 H + G'^3 H \left(F'^2 + G'^2\right)^{\frac{1}{2}} + 2B_y G' F' F^2 + 4B_y G'^2 F G + 2FGG'^2 \left(F'^2 + G'^2\right)^{\frac{1}{2}} - 2B_y G^2 G' F' + 2B_y G' F'^2 H + F'^2 G' H \left(F'^2 + G'^2\right)^{\frac{1}{2}} + 2FGF'^2 \left(F'^2 + G'^2\right)^{\frac{1}{2}} \Big] \left(2B_y G'^2 + \left(F'^2 + G'^2\right)^{\frac{1}{2}} G'^2 + \left(F'^2 + G'^2\right)^{\frac{1}{2}} F'^2 + 2B_y F'^2 \right)^{-1} \tag{A.30}$$

APPENDIX B

Flow of a Power Law Fluid over a Rotating Disk

The relation between the stress components τ_{ij} and the rate of deformation tensor e_{ij} (for steady, laminar, incompressible flow) using a power law model is given by

$$\tau_{ij} = -K\mathbf{e}_{ij} \tag{B.1}$$

where K is the apparent viscosity of the fluid. With the standard boundary-layer approximations noted in Chapter 3 (Section 3.1.3) and assuming rotational symmetry, the apparent viscosity of a power-law fluid takes the following form

$$K = m\left[\left(\frac{\partial v_r}{\partial z}\right)^2 + \left(\frac{\partial v_\phi}{\partial z}\right)^2\right]^{\frac{n-1}{2}} \tag{B.2}$$

where m is the fluid consistency constant and n is the power law index, with $n > 1$, $n < 1$ corresponding to shear-thickening and shear-thinning fluids, respectively. The classical Newtonian viscosity law is obtained by setting $n = 1$.

The flow is again governed by the transport equations of momentum and continuity (3.7) to (3.10) given in Chapter 3. In order to solve these equations, it is convenient to introduce a dimensionless distance, ζ, from the disk, following (Mitschka and Ulbrich, 1965):

$$\zeta = z\left(\frac{r^{1-n}\,\Omega^{2-n}}{K/\rho}\right)^{\frac{1}{1+n}} \tag{B.3}$$

Furthermore, the following assumptions are made for the velocity components:

$$F(\zeta) = \frac{v_r}{\Omega r} \tag{B.4 a}$$

$$G(\zeta) = \frac{v_\phi}{\Omega r} \tag{B.4 b}$$

$$H(\zeta) = \frac{v_z}{\left(r^{n-1}\Omega^{2n-1}\quad K/\rho\right)^{\frac{1}{1+n}}} \tag{B.4 c}$$

Inserting these expressions into equations (3.7) to (3.9), we obtain a system of ordinary differential equations for the functions *F*, *G* and *H*, as follows:

$$H' = -2F - \frac{(1-n)F'\zeta}{n+1} \tag{B.5}$$

$$\begin{aligned} F'' = &\left(F^2 - G^2 + \left(H + \frac{(1-n)F\zeta}{n+1}\right)F'\right)\left(1 + \frac{(n-1)G'^2}{F'^2 + G'^2}\right) - (n-1)F'G' \\ &\left(2FG + \left(H + \frac{(1-n)F\zeta}{n+1}\right)G'\right)\left(F'^2 + G'^2\right)^{-1}\left(n\left(F'^2 + G'^2\right)^{\left(\frac{1}{2}n - \frac{1}{2}\right)}\right)^{-1} \end{aligned} \tag{B.6}$$

$$G'' = \left(2FG + \left(H + \frac{(1-n)F\zeta}{n+1}\right)G'\right)\left(1 + \frac{(n-1)F'^2}{F'^2 + G'^2}\right) - (n-1)F'G' \\ \left(F^2 - G^2 + \left(H + \frac{(1-n)F\zeta}{n+1}\right)F'\right)\left(F'^2 + G'^2\right)^{-1}\left(n\left(F'^2 + G'^2\right)^{\left(\frac{1}{2}n - \frac{1}{2}\right)}\right)^{-1} \tag{B.7}$$

The set of the ODE's given by equations (B.5) to (B.7) for a power law fluid represents a "two-point boundary value problems" (TPBVP) which must be solved numerically. Solution of these equations was obtained by the same method described in Chapter 3. The ODEs (B.5) to (B.7) can be cast into first order ODEs in a similar way to the Bingham fluid case. By putting

$y_1 = F, \quad y_2 = F', \quad y_3 = G, \quad y_4 = G', \quad y_5 = H,$

we are left with five nonlinear ODEs for the variables F', F'', G', G'' and H' as functions of the independent variable ζ .

The boundary conditions are given by

$y_1(0) = 0,\ y_2(0) = a,\ y_3(0) = G(0),\ y_4(0) = b,\ y_5(0) = 0,$

where *a* and *b* are unknown.

A multiple shooting method was used for obtaining the numerical solution of this nonlinear boundary value problem. The details of these numerical calculations were given in Chapter 3.

Appendix D

PIV Results

Examples of one velocity vector map and ensemble average of 50 velocity vector maps, corresponding to the vertical plane for water at 10 rpm are shown in Figs. D.1 (a) and (b), respectively. It should be noted that the figure indicates the image boundaries not the extent of the tank. Figure D.1 shows that there are almost no differences between the two velocity figures, (a) and (b).

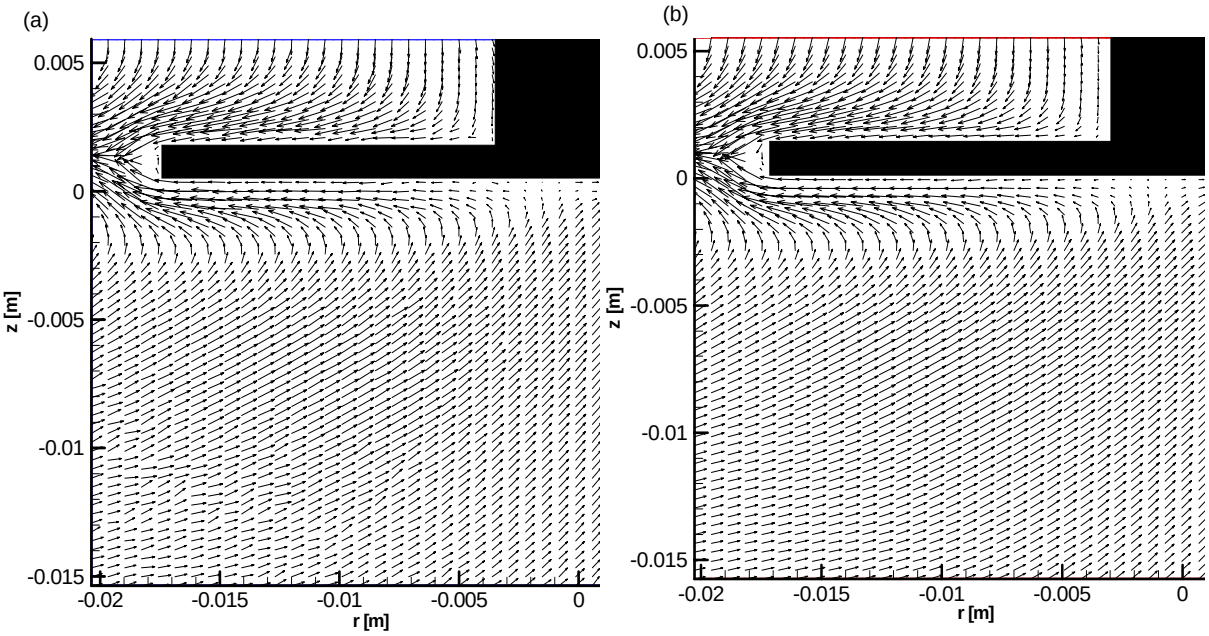

Figure D.1: PIV vector maps of velocity data in the (*r*-*z*) plane for water: (a) one velocity vector map , (b) ensemble average of 50 velocity vector maps. (Ω =10 rpm)

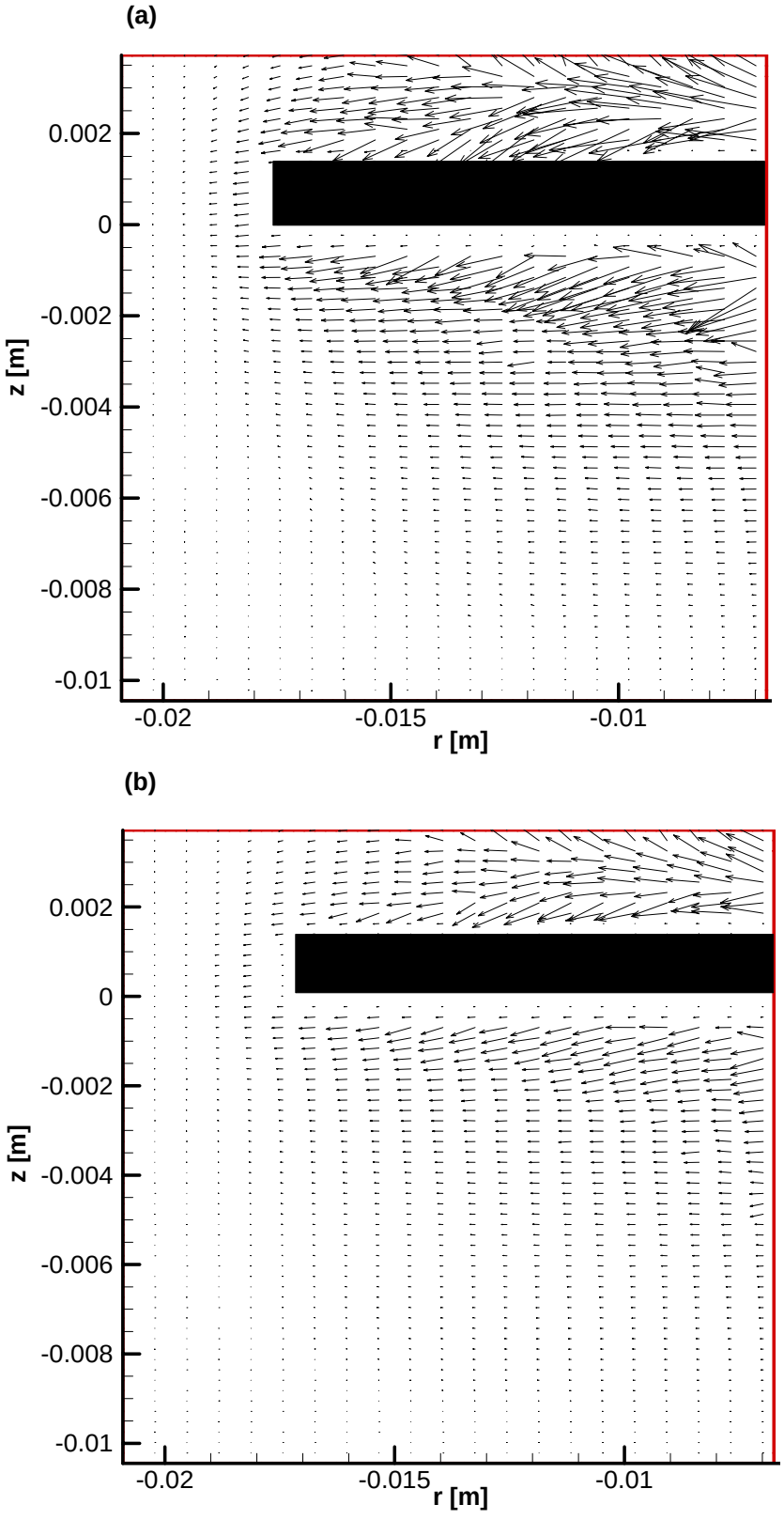
(a)
0.002
0
-0.002
-0.004
-0.006
-0.008
-0.01
z [m]
-0.02
-0.015
-0.01
r [m]
(b)
0.002
0
-0.002
-0.004
-0.006
-0.008
-0.01
z [m]
-0.02
-0.015
-0.01
r [m]

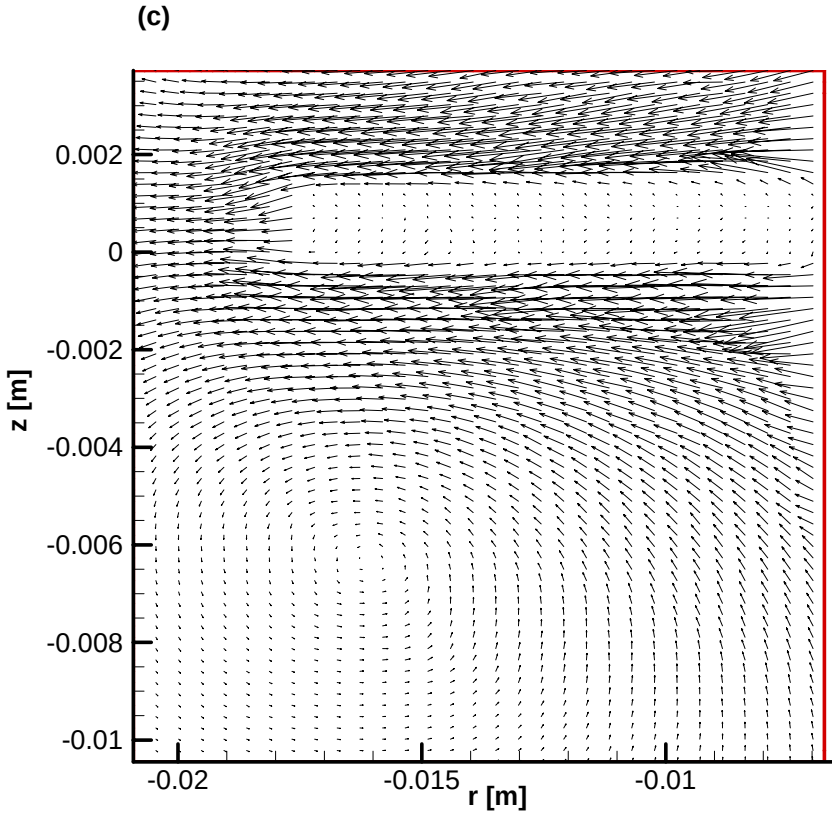

Figure D.2: PIV vector maps of velocity data in the (*r*-*z*) plane for the gel: (a) Ω =30 rpm; (b) Ω =60 rpm; (c) Ω =1200 rpm

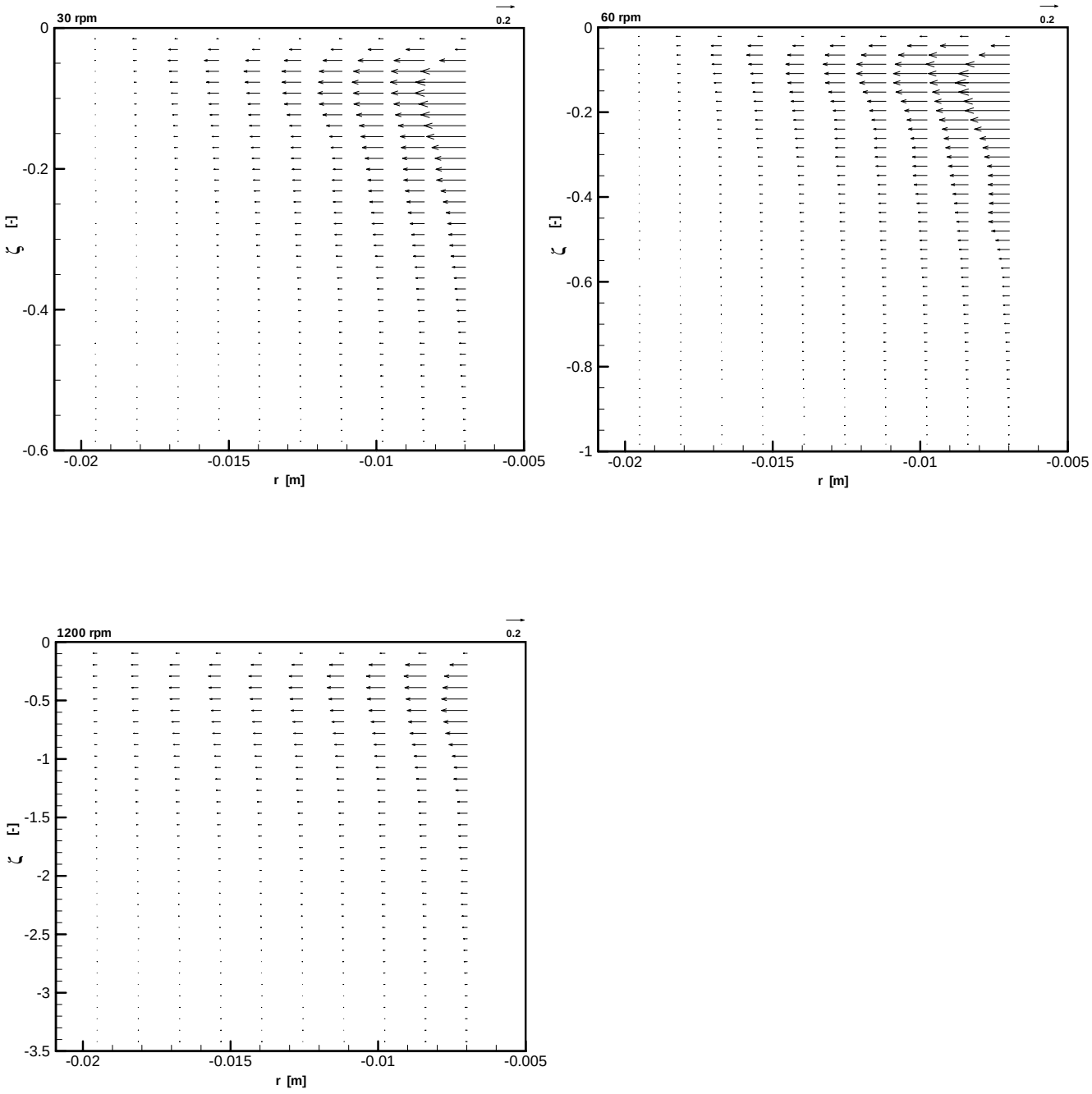

Figure D.3: PIV vector profile of the dimensionless radial velocity of the gel at rotational speeds of Ω = 30, 60 and 1200 rpm, respectively.

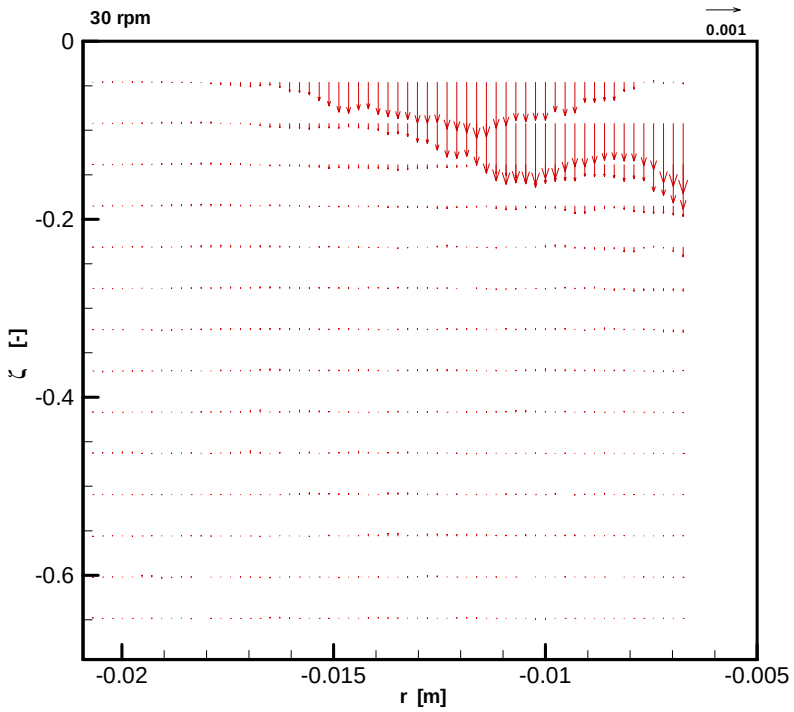

Figure D.4: PIV vector profile of the dimensionless axial velocity of the gel at rotational speed of $\Omega = 30$

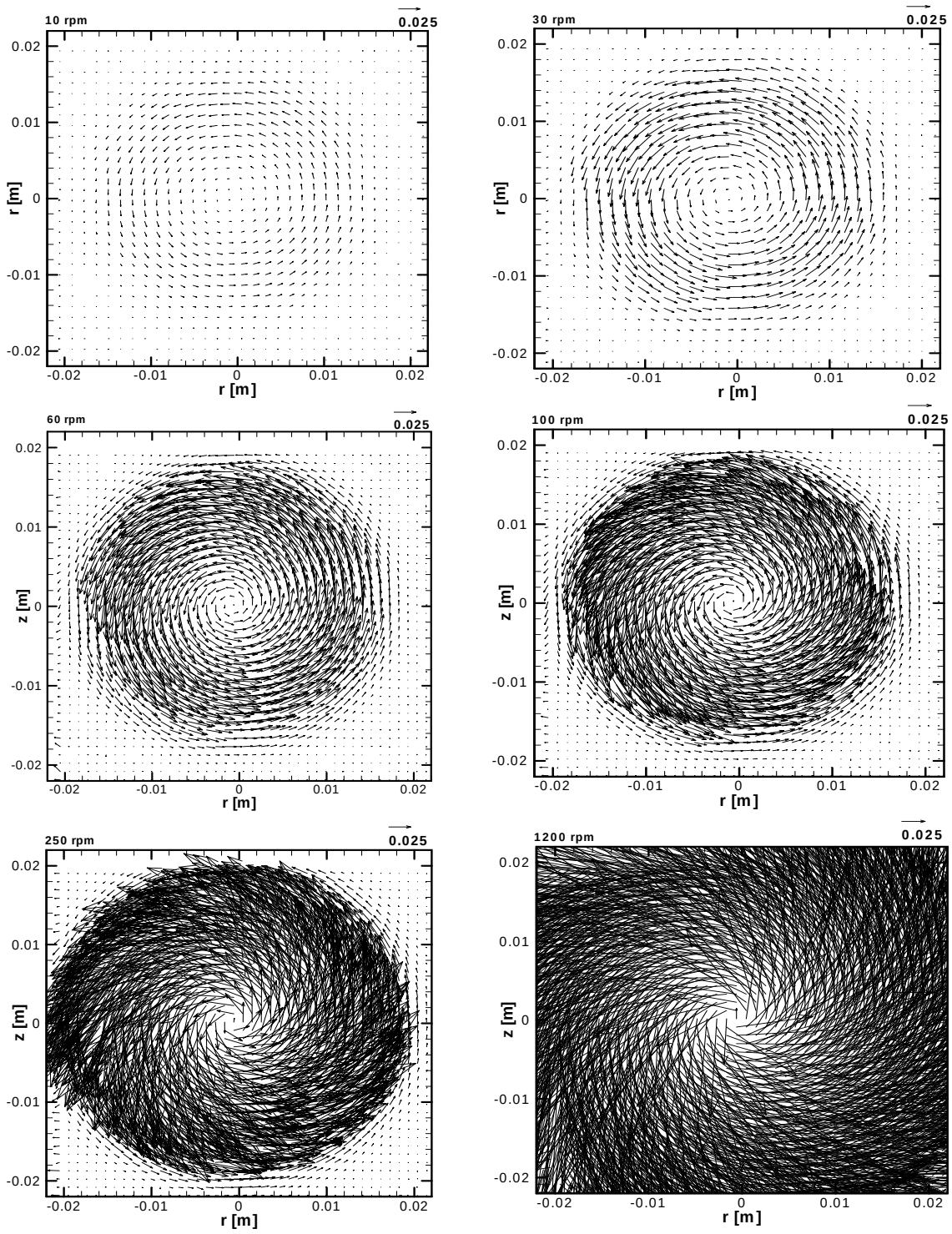

Figure D.5: PIV velocity vectors for gel at z = 0.005 m from the surface of the disk in the (r-ϕ) plane at: Ω = 10, 30, 60, 100, 250 and 1200 rpm, respectively.

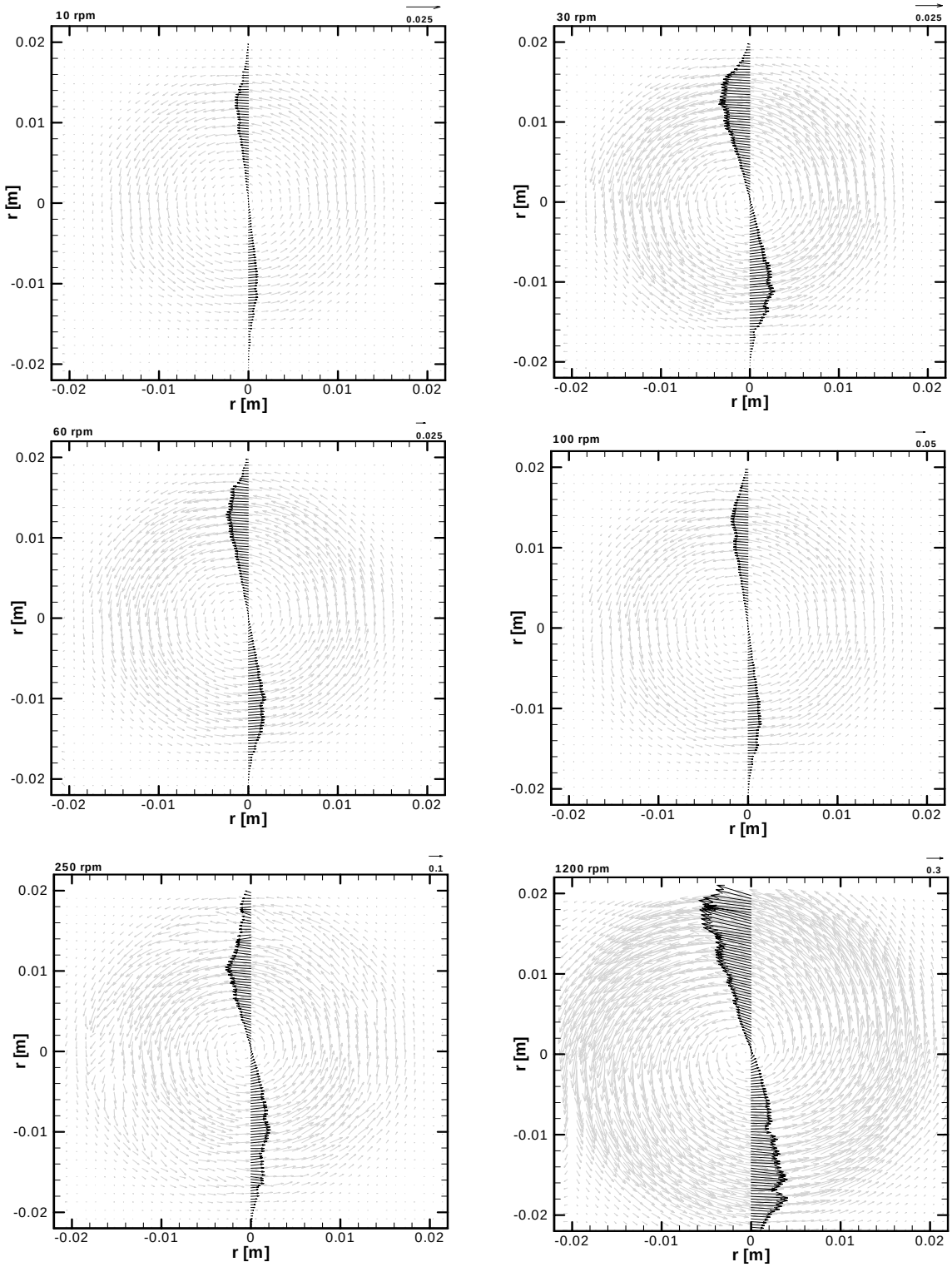

Figure D.6: PIV vector profile of the tangential velocity for the gel along the radial axis at rotational speeds of Ω = 10, 30, 60, 100, 250 and 1200 rpm, respectively.

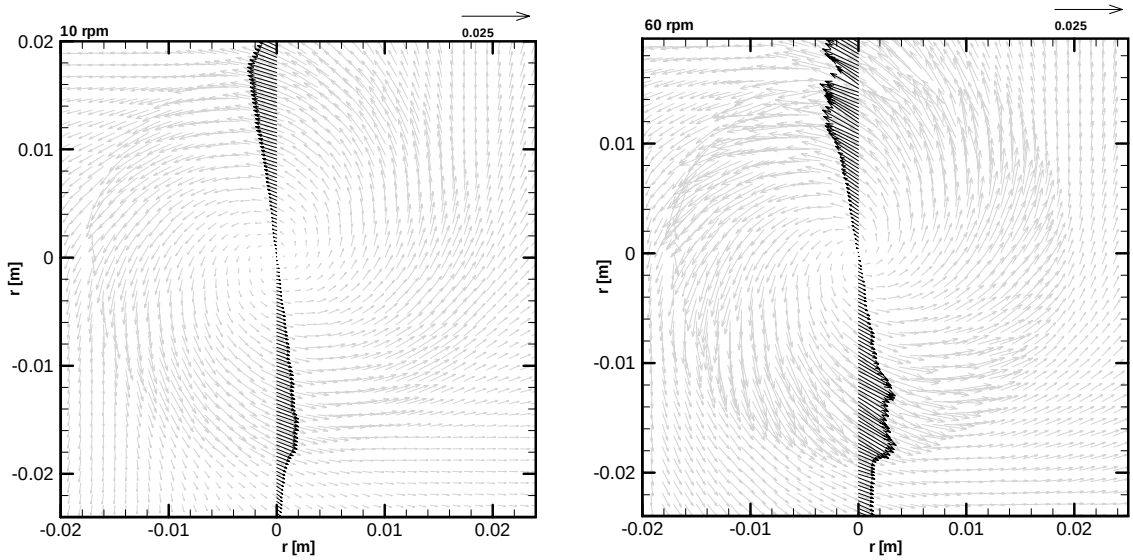

Figure D.7: PIV vector profile of the tangential velocity for water along the radial axis at rotational speeds of Ω = 10 and 60 rpm.

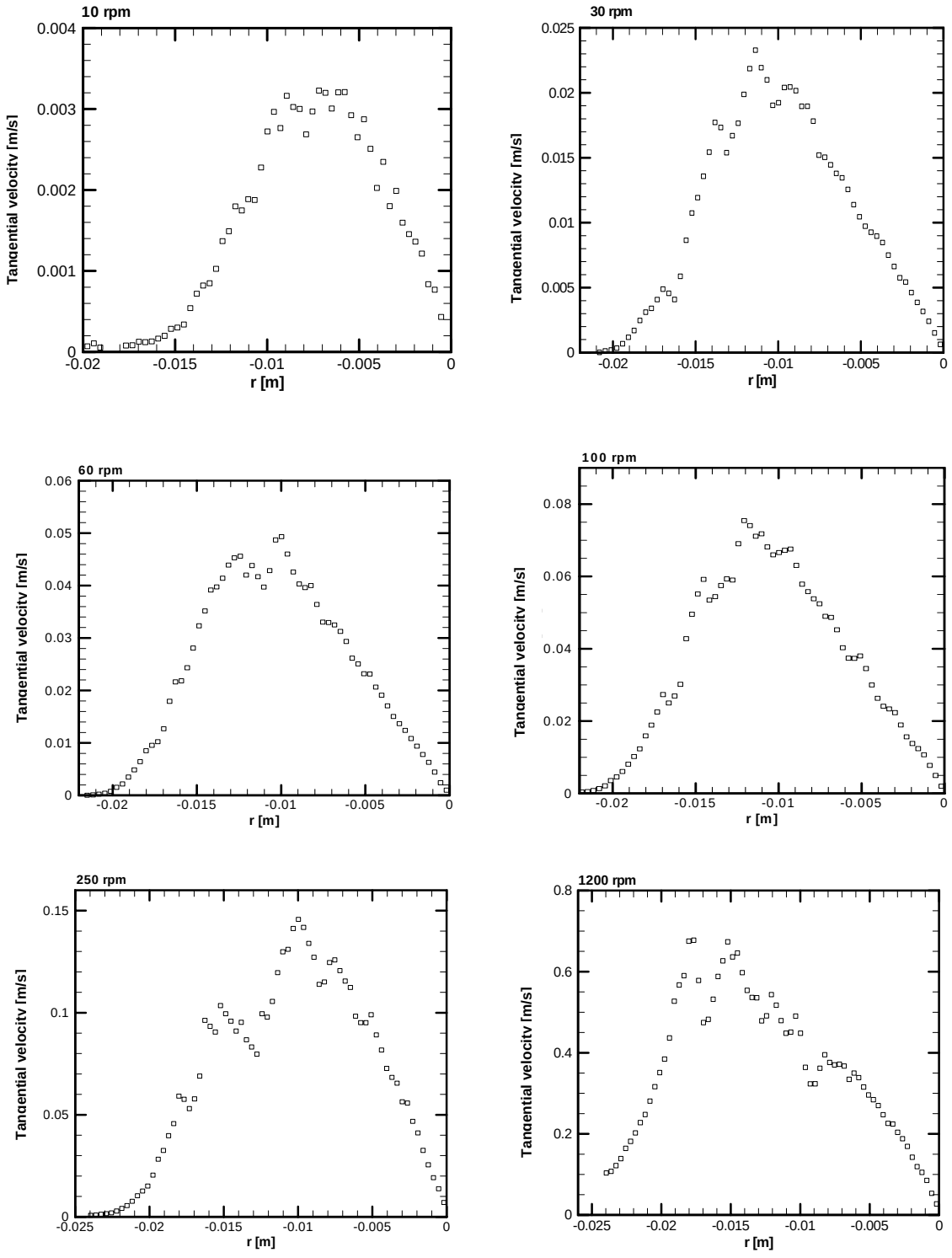

Figure D.8: Distribution of the tangential velocity component for the gel along the radial axis at rotational speeds of Ω = 10, 30, 60, 100, 250 and 1200 rpm, respectively.

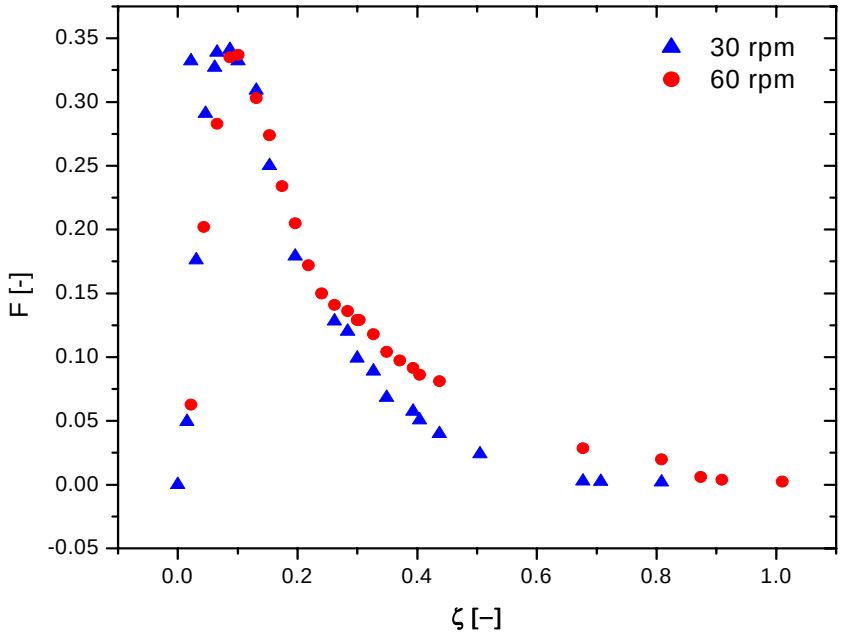

Figure D.9: Dimensionless radial velocity for 50 wt% gel solution at different rotational speeds.

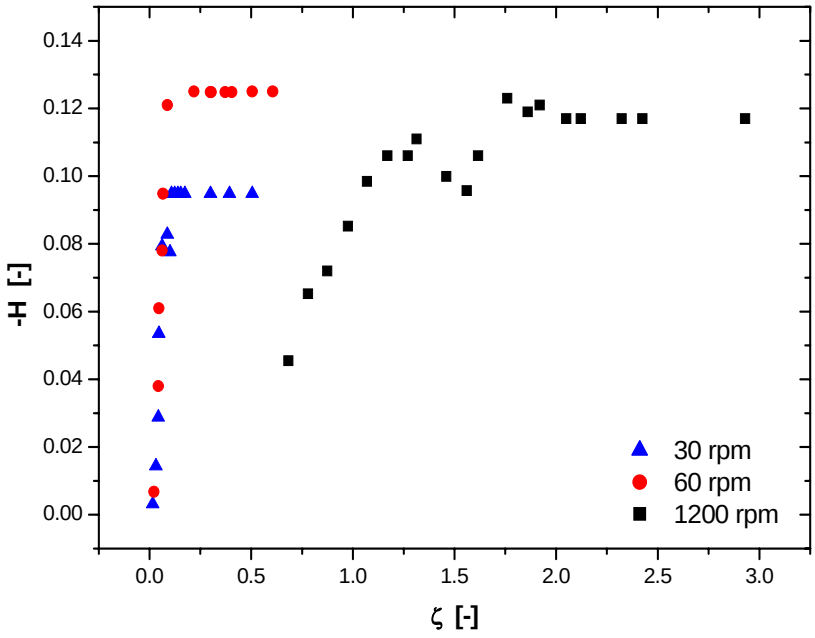

Figure D.10: Dimensionless axial velocity for 50 wt% gel solution at different rotational speeds.

APPENDIX E

Solution Method

A brief description of the multiple-shooting method for a two-point boundary value problem (TPBVP) is as follows (Roberts and Shapman, 1972):

Each of the set of *n* nonlinear ODEs can be written as

$$y_i' = f(x, y_i) \qquad \text{(E.1)}$$

The range [a,b] is split into *N* parts by the partition $x_0, x_1, ..., x_N$ such that

$$a = x_0 < x_1 < x_2 < ..... < x_N = b \qquad \text{(E.2)}$$

Initial conditions $y_i(x_i) = S_i$ are chosen, and the equations

$$y_i' = f(x, y_i) \qquad \text{(E.3)}$$

are integrated using the fourth-order Runge-Kutta method with variable step size over the subinterval $[x_i, x_{i+1}]$ to give

$y_i(x_{i+1})$ for $i = 0,1,...N-1$

To find the solution of (E.1) we must satisfy the non-linear equation set

$$T(S) = 0 \qquad \text{(E.4)}$$

where

$$S=\begin{bmatrix} S_0 \\ S_1 \\ . \\ . \\ . \\ S_{N-1} \end{bmatrix}, \qquad T(S)=\begin{bmatrix} y_0(x_1)-S_1 \\ y_1(x_2)-S_2 \\ . \\ . \\ S_{N-2}(x_{N-1})-S_{N-1} \\ g(S_0,\, y_{N-1}(x_N))-S \end{bmatrix} \tag{E.5}$$

The first *N-1* elements of *T* are continuity (matching) conditions while the last element represents the boundary condition. Equation (E.5) is solved by a modified Newton iteration as described by Roberts and Shapman (1972). The Jacobian $\partial T/\partial S$ can be calculated by differencing or can be supplied. In our case we supply them in a separate subroutine for the three cases, Newtonian, Bingham and power-law fluids. At each iteration in the Newton method a system of equations

$$J\Delta S^{(j)} = -T\left(S^{(j)}\right), \tag{E.6}$$

is solved for a correction $\Delta S^{(j)}$ to $S^{(j)}$, where J is the Jacobean (evaluated at $S^{(j)}$) with block form

$$J=\begin{bmatrix} G_0 & -\overline{G}_1 & & & \\ & G_1 & -\overline{G}_2 & & \\ & & & G_{N-1} & -\overline{G}_N \\ A & 0 & & 0 & B \end{bmatrix} \tag{E.7}$$

where A and B are Jacobeans arising from the boundary conditions and where the matrices G_i and $\overline{G}_i$ arise from the continuity (matching) conditions.

$$G_i = \frac{\partial y(x_{i+1}, S_i)}{\partial S_j}, \qquad i = 0,..., N-1, \qquad A = \frac{\partial T}{\partial y(a)}, \qquad B = \frac{\partial T}{\partial y(b)},$$

This procedure has been formulated in a subroutine called BVPMS from the International Mathematics and Statistics Libraries (IMSL). The pertained details of the subroutine are provided below.

BVPMS/DBVPMS (Single/Double precision)

Solve a (parameterized) system of differential equations with boundary conditions at two points, using a multiple-shooting method.

Usage

CALL BVPMS (FCNEQN, FCNJAC, FCNBC, NEQNS, TLEFT, TRIGHT, DTOL, BTOL, MAXIT, NINIT, TINIT, YINIT, LDYINI, NMAX, NFINAL, TFINAL, YFINAL, LDYFIN)

Arguments

FCNEQN — User-supplied SUBROUTINE to evaluate derivatives. The usage is

CALL FCNEQN (NEQNS, T, Y, P, DYDT), where

NEQNS – Number of equations. (Input)

T – Independent variable, *t*. (Input)

Y – Array of length NEQNS containing the dependent variable. (Input)

P – Continuation parameter used in solving highly nonlinear problems. (Input)

See Comment 4.

DYDT – Array of length NEQNS containing *y′* at T. (Output)

The name FCNEQN must be declared EXTERNAL in the calling program.

FCNJAC — User-supplied SUBROUTINE to evaluate the Jacobian. The usage is

CALL FCNJAC (NEQNS, T, Y, P, DYPDY), where

NEQNS – Number of equations. (Input)

T – Independent variable. (Input)

Y – Array of length NEQNS containing the dependent variable. (Input)

P – Continuation parameter used in solving highly nonlinear problems. (Input)

See Comment 4.

DYPDY – Array of size NEQNS by NEQNS containing the Jacobian. (Output)

The entry DYPDY(i, j) contains the partial derivative $\partial f_i / \partial y_j$ evaluated at (t, y).

The name FCNJAC must be declared EXTERNAL in the calling program.

FCNBC — User-supplied SUBROUTINE to evaluate the boundary conditions. The usage is CALL FCNBC (NEQNS, YLEFT, YRIGHT, P, H), where

NEQNS – Number of equations. (Input)

YLEFT – Array of length NEQNS containing the values of Y at TLEFT. (Input)

YRIGHT – Array of length NEQNS containing the values of Y at TRIGHT. (Input)

P – Continuation parameter used in solving highly nonlinear problems. (Input)

See Comment 4.

H – Array of length NEQNS containing the boundary function values. (Output)

The computed solution satisfies (within BTOL) the conditions $h_i = 0$, $i = 1, \ldots\ldots, NEQNS$.

The name FCNBC must be declared EXTERNAL in the calling program.

NEQNS — Number of differential equations. (Input)

TLEFT — The left endpoint. (Input)

TRIGHT — The right endpoint. (Input)

DTOL — Differential equation error tolerance. (Input)

An attempt is made to control the local error in such a way that the global error is proportional to DTOL.

BTOL — Boundary condition error tolerance. (Input) The computed solution satisfies the boundary conditions, within BTOL tolerance.

MAXIT — Maximum number of Newton iterations allowed. (Input) Iteration stops if convergence is achieved sooner. Suggested values are MAXIT = 2 for linear problems and MAXIT = 9 for nonlinear problems.

NINIT — Number of shooting points supplied by the user. (Input) It may be 0. A suggested value for the number of shooting points is 10.

TINIT — Vector of length NINIT containing the shooting points supplied by the user. (Input)

If NINIT = 0, then TINIT is not referenced and the routine chooses all of the shooting points. This automatic selection of shooting points may be expensive and should only be used for linear problems. If NINIT is nonzero, then the points must be an increasing sequence with TINIT(1) = TLEFT and TINIT(NINIT) = TRIGHT.

YINIT — Array of size NEQNS by NINIT containing an initial guess for the values of Y at the points in TINIT. (Input) YINIT is not referenced if NINIT = 0.

LDYINI — Leading dimension of YINIT exactly as specified in the dimension statement of the calling program. (Input)

NMAX — Maximum number of shooting points to be allowed. (Input) If NINIT is nonzero, then NMAX must equal NINIT. It must be at least 2.

NFINAL — Number of final shooting points, including the endpoints. (Output)

TFINAL — Vector of length NMAX containing the final shooting points. (Output) Only the first NFINAL points are significant.

YFINAL — Array of size NEQNS by NMAX containing the values of Y at the points in TFINAL. (Output)

LDYFIN — Leading dimension of YFINAL exactly as specified in the dimension statement of the calling program. (Input)

Comments

1. Automatic workspace usage is

BVPMS NEQNS * (NEQNS + 1)(NMAX + 12) + 2 * NEQNS + 30 DBVPMS 2 * NEQNS * (NEQNS + 1)(NMAX + 12) + 3 * NEQNS + 60 Workspace may be explicitly provided, if desired, by use of B2PMS/DB2PMS. The reference is

CALL B2PMS (FCNEQN, FCNJAC, FCNBC, NEQNS, TLEFT, TRIGHT, DTOL, BTOL, MAXIT, NINIT, TINIT, YINIT, LDYINI, NMAX, NFINAL, TFINAL, YFINAL, LDYFIN, WORK, IWK) The additional arguments are as follows:

WORK — Work array of length NEQNS * (NEQNS + 1)(NMAX + 12) + NEQNS + 30.

IWK — Work array of length NEQNS.

2. Informational errors

Type Code

1 5 Convergence has been achieved; but to get acceptably accurate approximations to $y(t)$, it is often necessary to start an initial-value solver, for example IVPRK, at the nearest TFINAL(i) point to t with $t \geq$TFINAL (i). The vectors YFINAL (j, i), j = 1,….., NEQNS are used as the initial values.

4 1 The initial-value integrator failed. Relax the tolerance DTOL or see Comment 3

4 2 More than NMAX shooting points are needed for stability.

4 3 Newton's iteration did not converge in MAXIT iterations. If the problem is linear, do an extra iteration. If this error still occurs, check that the routine FCNJAC is giving the correct derivatives. If this does not fix the problem, see Comment 3.

4 4 Linear-equation solver failed. The problem may not have a unique solution, or the problem may be highly nonlinear. In the latter case, see Comment 3.

3. Many linear problems will be successfully solved using program selected shooting points. Nonlinear problems may require user effort and input data. If the routine fails, then increase NMAX or parameterize the problem. With many shooting points the program essentially uses a finite-difference method, which has less trouble with nonlinearities than shooting methods. After a certain point, however, increasing the number of points will no longer help convergence. To parameterize the problem,

see Comment 4.

4. If the problem to be solved is highly nonlinear, then to obtain convergence it may be necessary to embed the problem into a one parameter family of boundary value problems, $y' = f(t, y, p)$, $h(y(t_a, t_b, p)) = 0$ such that for $p = 0$, the problem is simple, e.g., linear; and for $p = 1$, the stated problem is solved. The routine BVPMS/DBVPMS automatically moves the parameter from $p = 0$ toward $p = 1$.

5. This routine is not recommended for stiff systems of differential equations.

Algorithm

Define N = NEQNS, M = NFINAL, t_a, = TLEFT and t_b, = TRIGHT. The routine BVPMS uses a multiple-shooting technique to solve the differential equation system $y' = f(t, y)$ with boundary conditions of the form

$$h_k(y_1(t_a),.....,y_N(t_a),.....,y_N(t_b)) = 0 \qquad \text{for } k = 1, \ldots\ldots, N$$

A modified version of IVPRK is used to compute the initial-value problem at each "shot." If there are M shooting points (including the endpoints t_a and t_b), then a system of NM simultaneous nonlinear equations must be solved. Newton's method is used to solve this system, which has a Jacobian matrix with a "periodic band" structure. Evaluation of the NM functions and the NM x NM (almost banded) Jacobian for one iteration of Newton's method is accomplished in one pass from t_a to t_b of the modified IVPRK, operating on a system of $N(N+1)$ differential equations. For most problems, the total amount of work should not be highly dependent on M. Multiple shooting avoids many of the serious ill conditioning problems that plague simple shooting methods. For more details on the algorithm, see Sewell (1982). The boundary functions should be scaled so that all components h_k are of comparable magnitude since the absolute error in each is controlled.